



ENVIRO-CHEM SYSTEMS

GT 350 0025

Handwritten signature/initials

ENVIRO-CHEM SYSTEMS

A MONSANTO COMPANY

14522 SOUTH OUTER FORTY ROAD

CHESTERFIELD, MISSOURI 63017

P.O. Box 14547

ST. LOUIS, MISSOURI 63178

PHONE (314) 275-5700

FAX (314) 275-5701

enviroch@monsanto.com

www.enviro-chem.com

03 October 2000

U.S. Nuclear Regulatory Commission
Advisory Committee: Reactor Safety
Room T2 - E26
Washington, D.C. 20555-0001

RECEIVED
ACRS/ACNW

OCT 25 2000

PM
7:38:31 12/12/31/5/6

Dear Sirs,

Enclosed are several reprints and a copy of a draft paper (accepted for publication) which relate to the mechanical integrity of thermowells in severe or hazardous services. They specifically show that the current thermowell design standard is unsafe for hazardous applications.

Also enclosed are copies of papers relating to the Monju incident, regarding thermowell failures.

We have been in contact with Mr. Morishita, and have performed informal calculations on his thermowell designs using our model. They predict thermowell failure without having to invoke "symmetric vortex shedding."

We also have a monograph in preparation (80 pages or so) relating to the details that publication space does not usually allow.

Yours truly,

MONSANTO ENVIRO-CHEM SYSTEMS, INC.

Handwritten signature of David S. Bartran

David S. Bartran
Sr. Instrument Engineering Specialist

Tel: 314.275.5869

Fax: 314.275.5942

email: David.S.Bartran@monsanto.com

DBS/jd
Enclosure

**ACRS OFFICE COPY
DO NOT REMOVE FROM ACRS OFFICE**

Handwritten: GT-350

Reprinted from

ISA TRANSACTIONS[®]

ISA Transactions 38 (1999) 123–132

Flow induced vibration of thermowells

David S. Bartran^{a,*}, Jerry M. Kinsey^a, Robert Schappelle^b, Richard Yee^a

^a*Monsanto Enviro-Chem Systems, 14522 South Outer Forty Road, Chesterfield, MO 63017, USA*

^b*Marconi Integrated Systems, Inc., San Diego, CA, USA*



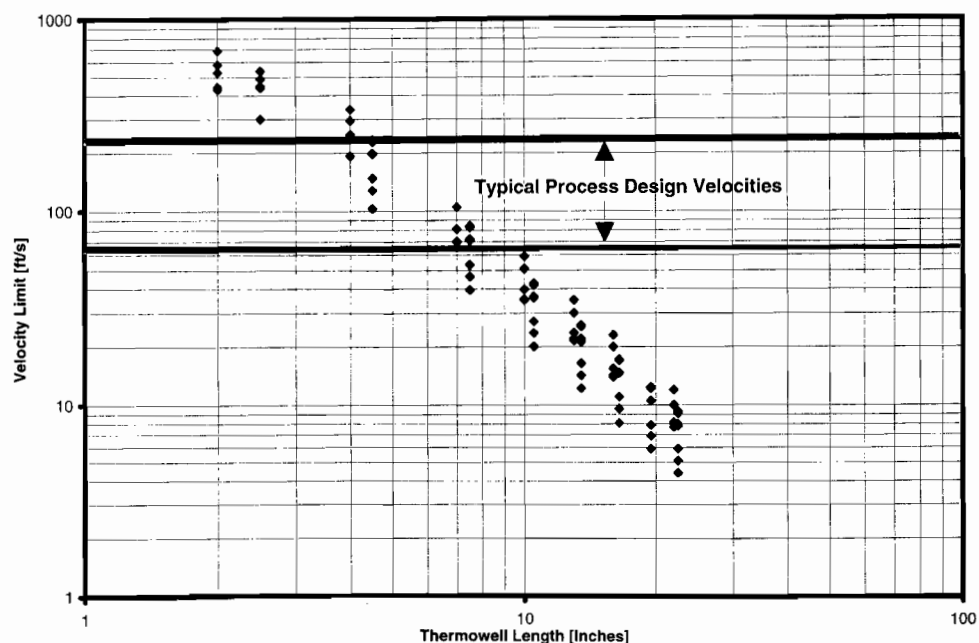


Fig. 1. Representative velocity limits for industrial thermowells. The range of process velocities commonly encountered are shown.

The ASME Power Test Code, PTC 19.3 [1,2] currently establishes the design criteria for thermowells in steam service and is widely used as the starting point for many thermowell designs. It is the basis of the published ratings shown in Fig. 1. The code model is based on a quasi-static analysis of a prismatic beam and includes contributions due to hydrostatic pressure, fluid drag, and vortex shedding. While this model is readily modified to include other fluids and even mechanical damping, it is formally restricted to sub-critical, i.e. sub-resonant, conditions. This is an essential restriction in high pressure steam service, but it leads to the application difficulties described for long thermowells.

To better understand the design issues involved in relaxing the requirement for sub-critical operation and improving the rating method for practical thermowells, the simplest possible thermowell model is considered. This model which permits an exact solution and demonstrates how resonance(s) evolve with flow. It also removes the mystery of thermowell stress, at least for the practicing instrument engineer, and serves as a benchmark for approximate methods.

2. Uniform cantilever in a flowing media

Consider a slender beam, attached to an infinite half-plane and extending into a fluid stream [3] as shown in Fig. 2. The fluid has uniform velocity acting to deflect the beam with a force consisting of static and time dependent components. The dynamic equation describing the forced excitation of a beam is given by:

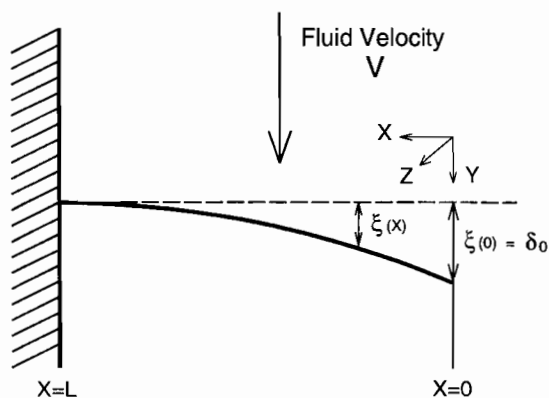


Fig. 2. Idealized thermowell extending into a moving fluid. The deflection response to simple drag is illustrated.

$$\frac{\partial^2}{\partial x^2} [EI \frac{\partial^2}{\partial x^2} \underline{\xi}(x, t)] = -\mu \frac{\partial^2}{\partial t^2} \underline{\xi}(x, t) + \underline{F} - \alpha \frac{\partial}{\partial t} \underline{\xi}(x, t) \quad (1)$$

with centerline deflection, $\underline{\xi}(x, t)$, modulus of elasticity, E , moment of inertia, I , mass per unit length, μ , viscous damping coefficient, α , acting to oppose the motion, and a generalized excitation force, \underline{F} . The equation is written in vector notation under the proviso, that only small amplitude displacements are considered.

Two deflections are considered: that due to drag and that due to vortex shedding. The drag response is a steady deflection parallel to the direction of flow while the vortex shedding response is a periodic deflection and perpendicular to the direction of flow. The two excitations as viewed from the tip end of the cantilever are shown in Fig. 3. The beam responses in these two directions are de-coupled to the extent that there is no interaction between adjacent fibers or torsional effects. As a result, the equation of motion for the two coordinates, are identical except for the form of excitation. A vector is used, fully recognizing that this represents two scalar beam equations.

The coordinate system is defined, such that the tip of the undisturbed cantilever is located at the origin. The solution must satisfy the standard set of boundary conditions for a beam clamped and the base and free at other end: $\{\underline{\xi}(L, t), \underline{\xi}'(L, t), \underline{\xi}''(0, t), \underline{\xi}'''(0, t)\} = \{0, 0\}$, with the auxiliary relationship governing the stress response, $\underline{\sigma}(x) = 1/2 DE \underline{\xi}''(x, \omega)$.

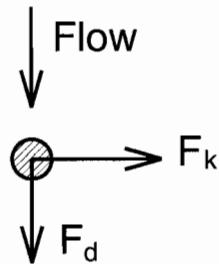


Fig. 3. The tip view, showing the drag and vortex shedding forces relative to the flow direction.

3. The response to drag

The drag response is a deflection in the direction of flow, and is a static for a steady flow condition. The solution is obtained by direct integration for the case of a uniformly distributed force. After the boundary conditions are imposed, the solution reduces to:

$$\xi(x) = \delta_o [1 - 4/3(x/L) + 1/3(x/L)^4], \quad (2)$$

with a tip deflection, δ_o , given by

$$\delta_o = |F_d| L^4 / 8EI. \quad (3)$$

The root stress, σ_o , defined in terms of the second derivative of the deflection at the attachment point, is

$$\sigma_o \equiv 1/2 DE |\xi''(L)| = |F_d| L^2 / 4I. \quad (4)$$

The distributed force acting on the cantilever is:

$$|F_d| = 1/2 \rho_f C_d D V^2. \quad (5)$$

Not surprisingly, Eqs. (3) and (4) are the traditional cantilever formulas and represent the response to a uniformly distributed load.

4. The response to vortex shedding

Vortex shedding is a common phenomenon, frequently visible in wind driven motion of power cables or telephone wires, or the rippling motion of flags, but it also occurs in heat exchanger tube banks and thermowell applications. It was first described by von Karman as a flow induced sound emitted from wires stretched across a duct. Later, Strouhal developed the relationship between the frequency of vortex formation and fluid velocity. Basically these vortices are characterized by flow rate dependent fluctuations in the pressure field surrounding the object. The pressure fluctuations are associated with the initiation and development of vortices that develop and roll-off in alternating fashion to form a series of vortices trailing behind the object.

At the risk of over-simplifying vortex shedding phenomena, they are resolved as two forces: one parallel with the flow direction and the other perpendicular. The force parallel to the flow direction is dominated by a constant term resulting from aerodynamic drag, which is modeled in the preceding section, and a small periodic component which is ignored. The force perpendicular to the direction of flow, is periodic, and comparable to the drag force; it is the dominant feature of vortex shedding. The vortex shedding force is taken to be as uniformly distributed and varies in time only. This is only an approximation and ignores coupling between instantaneous cantilever deflection and initiation of the vortices.

The transverse force resulting from vortex shedding is proportional to the aerodynamic pressure with a magnitude given by

$$|F_k| = 1/2 \rho_f C_k D V^2, \quad (6)$$

where the force coefficient, C_k associated with the strength of the von Karman vortices, is comparable to the conventional drag force coefficient, C_d . The excitation frequency is proportional to the fluid velocity:

$$\omega = 2\pi S V / D. \quad (7)$$

The Strouhal Number, $S \sim 0.22$, is assumed constant and empirically relates the cantilever diameter, D , and fluid velocity, V , to the vortex shedding frequency, ω . When the excitation approaches one of the natural frequencies of the cantilever, resonance can occur. Since the excitation frequency and fluid velocity (or flow rate) are linearly related, the terms *critical frequency*, *critical velocity*, or *critical flow* are used interchangeably to denote the resonance condition. For example, the first, second, and third criticals, etc., can be expressed either as a frequency, velocity, or flow criticals. They should not to be confused with sonic velocity.

5. Approximate resonant amplitudes

At resonance, the kinetic and potential energies of the vibrating cantilever are in balance so that

the rate of energy transfer to the system must equal the total dissipation. This results in a simple relationship between the aerodynamic forces acting on the cantilever and the amplitude of vibration. Taking the integral average of both sides of the dynamic equation results in a balance of the excitation with the net loss:

$$|F_k| = \alpha \omega \langle \xi_k \rangle. \quad (8)$$

The mean deflection, $\langle \xi_k \rangle$ is indicated since the net loss is dependent on the overall deflection of the cantilever not just the displacement at any one point. Continuing with this estimate, the mean deflection is bounded by the root-mean-square and the tip deflection of a simple bending mode response to a uniformly distributed force, somewhat similar to mode participation factor used in a more rigorous analysis. The result is:

$$\langle \xi_k \rangle = \left\{ \left[\int \xi^2 d(x/L) \right]^{1/2} \delta_{0k} \right\}^{1/2} = 0.7119 \delta_{0k} \quad (9)$$

Combining Eqs. (6), (8) and (9), and substituting the ideal resonant frequency for ω_1 , from Eq. (18), results in an expression for the tip deflection. Since the drag and vortex shedding forces are comparable, the deflection perpendicular to the flow can be expressed in terms of ratio of the two:

$$\delta_{0k} / \delta_o = 11.23 (EI \mu)^{1/2} / \alpha \gamma^2 L^2. \quad (10)$$

The magnification ratio increases with flexural rigidity and decreases with increasing length.

In analogy with a spring-mass system, the amplification at resonance is defined in terms of the relative damping:

$$\delta_{0k} / \delta_o = 1/2 \zeta^{-1} (\equiv 1/2Q). \quad (11)$$

The quality factor, Q , borrowed from electrical circuit theory, is an alternative measure of the resonance. The relative damping defined in terms of the critical damping for non-resonant response, i.e. $\zeta = \alpha / \alpha_c$, so that:

$$\alpha_c = 22.47 (EI \mu)^{1/2} / \gamma^2 L^2. \quad (12)$$

The root stress and tip deflection ratios for the approximate solution are numerically equal, i.e. $\delta_{0k}/\delta_o \sim \sigma_{0k}/\sigma_o$. With Q 's in the range of 10–100, the tip deflections and root stresses resulting from vortex shedding are easily one to two orders larger than those due to conventional drag forces. In the case of large amplitude vibrations, a magnification ratio based on the deflection amplitudes relative to the beam diameter [4,5].

The shape of the first order resonance can be invoked by appeals to similarity with spring-mass system response [6], or rigorously developed as a power-series solution of Eq. (1). It is characterized by a complex amplitude of the form:

$$\delta_k/\delta_o = 1/(1 - (\omega/\omega_i)^2 + 2j\zeta\omega/\omega_i) \quad (13)$$

where ω_i is the resonant frequency of the cantilever, ζ is the relative damping, and $j = \sqrt{-1}$. The response is not limited to tip deflection and root stresses. For example, the tip acceleration, estimated as $\omega^2\delta_o$, can be important in the case of acceleration sensitive sensors. This solution is useful for frequencies up to and including the first critical (more about this later), but quickly runs into difficulties as soon as higher order modes are considered.

6. Modal summation

The response at the higher order modes can be obtained systematically by a *modal analysis* of the cantilever. Briefly the solution to Eq. (1) is approximated as a linear combination of undamped normal modes [7,9,10]:

$$\xi(x, \omega) \sim \sum q_i(\omega)\varphi_i(x), \quad (14)$$

where the, φ_i , are the modal solutions. These are commonly tabulated, real-valued, orthogonal functions. The expansion coefficients, q_i , are known as the generalized coordinates of the system.

The modal solutions for the ideal beam are routinely tabulated for a variety of boundary conditions [10]. For the ideal cantilever they have the form:

$$\begin{aligned} \varphi_i(x) = & \cos h(\gamma_i x/L) - \cos(\gamma_i x/L) \\ & - \sigma_i[\sin h(\gamma_i x/L) - \sin(\gamma_i x/L)] \end{aligned} \quad (15)$$

where the $\sigma_i = \{0.7341, 1.0185, 0.9992, 1.000, \dots\}$ are integration constants and γ_i are the modal constants.

Substituting the modal expansion is substituted into Eq. (1), and using the orthogonality relations, it is decomposed into a system of linear equations. For the case of periodic excitation [9], the dynamic equation reduces to:

$$q_i(\omega) = 8\gamma_i^{-4}\delta_o\Gamma_i/(1 - (\omega/\omega_i)^2 + 2j\zeta_i\omega/\omega_i). \quad (16)$$

The mode participation factor, $\Gamma_i \equiv 2\sigma_i/\gamma_i$, defines the relative strength of excitation for the given mode, ζ_i is the relative modal damping, and δ_o is the equivalent tip deflection resulting from drag. Modal damping is included to illustrate how losses limit the response at resonance and is a function of frequency. It is related to the viscous damping by:

$$\zeta_i = 1/2(\alpha/\omega_i\mu). \quad (17)$$

For the case of a uniform cantilever, mode participation factor is series of numbers $\Gamma_i = \{0.7829, 0.4339, 0.2544, 0.1819, \dots\}$, while the critical frequencies, ω_i , are given by:

$$\omega_i = \gamma_i^2(EI/\mu)^{1/2}/L^2, \quad (18)$$

with $\{\gamma_i\} = \{1.875, 4.694, 7.855, 10.995, \dots\}$.

The total response is a summation over all of the modes so that the deflection amplitude at the tip ($x = 0$) is given by:

$$\delta_k/\delta_o = |\sum 8\gamma_i^{-4}\Gamma_i/(1 - (\omega/\omega_i)^2 + 2j\zeta_i\omega/\omega_i)|. \quad (19)$$

Similarly the combined stress amplitude, as a sum of the drag and vortex shedding components as in the Code model is given by a summation of the modal contributions as:

$$\sigma/\sigma_o = 1 + |\sum 4\gamma_i^{-2}\Gamma_i/(1 - (\omega/\omega_i)^2 + 2j\zeta_i\omega/\omega_i)|, \quad (20)$$

where σ_o is the drag stress. The code model contains an additive term for the hydrostatic stresses

and a correction to allow for non-uniform beams, ignored in the present analysis, but is in principle, identical with Eq. (20) in the limit of zero losses. For the case of viscous damping, the normalized tip deflection and root stress decrease as $\sim \gamma_i^2 \Gamma_i$ and $\sim \Gamma_i$ respectively.

7. The exact solution

Using complex exponential notation, the transverse component of the dynamic equation, Eq. (1), has a product solution of the form, $\xi(z, \omega, t) = A(\omega)e^{kz}e^{j\omega t}$ for the case of sinusoidal excitation, $F = F_0e^{j\omega t}$. The frequency dependent coefficient is a complex variable. Substitution in the homogeneous equation results in the characteristic equation for the spatial coordinate:

$$k^4 - \mu\omega^2(1 - j\alpha/\omega\mu)/EI = 0. \quad (21)$$

This equation has four complex roots symmetrically arranged about the origin. Using de Moivre's theorem:

$$\{k_i\} = \{k_0 e^{j(\phi/4 + i\pi/2)}\}, \{i\} = \{0, 1, 2, 3\}. \quad (22)$$

These are more conveniently expressed as:

$$\{k_i\} = \{j^i k_0(a + jb)\}, \{i\} = \{1, 2, 3, 4\} \quad (23)$$

with the following definitions

$$a \equiv \cos(\phi/4) \quad (24)$$

$$b \equiv \sin(\phi/4) \quad (25)$$

$$k_0^4 \equiv \mu\omega^2(1 + \tan^2 \phi)^{1/2}/EI. \quad (26)$$

The principle angle of the complex roots, ϕ , is defined as

$$\tan \phi \equiv -\alpha/\mu\omega. \quad (27)$$

The periodic, steady-state solution is a sum of exponentials associated with the roots of the characteristic equation and the particular integral, i.e.

$$\xi(x, \omega) = Ae^{(a+jb)z} + Be^{j(a+jb)z} + Ce^{-(a+jb)z} + De^{-j(a+jb)z} + F_0e^{-j\phi}/k_0^{-4}EI. \quad (28)$$

This solution is subjected to the same set of boundary conditions as in the static case and results in a system of linear equations in terms of the unknown coefficients (**A**, **B**, **C**, and **D**). These coefficients are complex numbers and generally frequency dependent. Eight real unknowns and eight real equations are involved in the solution. This solution applies to all beams that are piecewise uniform with a considerable increase in the unknown coefficients and can be readily extended to stepped-profile beams and various boundary conditions.

The exact solution must be evaluated numerically. This proceeds by picking the excitation frequency, i.e. specifying the fluid velocity for a given process condition, and solving for the coefficients using any of the common routines, such as Gauss–Jordan elimination. This process is repeated for a range of flows to chart the over-all magnitude response. Since losses are included, the 8×8 coefficient matrix, formed from Eq. (28) when the boundary conditions are applied, is non-singular for all frequencies, and the resonances show up as well behaved peaks in the response rather than discontinuities. The temporal solution can be reconstructed by taking the real part of $\xi(z, \omega)e^{j\omega t}$, if needed. The tip displacement $|\xi(0, \omega)|$, tip acceleration $\omega^2|\xi(0, \omega)|$, and root stress $\sigma = DE|\xi''(L, \omega)|/2$ are readily calculated by direct evaluation.

The closed-end tip of practical thermowells, reflects a departure from a truly uniform beam, and affects the resonant frequencies slightly. It can be included as a mass loading which modifies tip shear condition, i.e.

$$EI\xi''(0) = \mu_{\text{Tip}}\omega^2\xi(0) \quad (29)$$

or by means of the Dunkerley or Rayleigh approximations. The “added mass” of the fluid surrounding the cantilever [5] is also important for high density gases or liquids and can be included as a correction to the effective mass density of the cantilever. It shows up as a noticeable pressure dependent resonance in compressible fluids. Other

boundary conditions which are included, such as pipe wall flexure can also be considered.

Several sample calculations are considered. In Fig. 4 the exact response (vortex shedding only) is plotted against the frequency, with Q ranging from 1.25 to 10. The response upto and including the first critical is similar to generalized magnification factor charts for a simple spring-mass systems [3,6,7] with the exception of the higher order criticals. Note that the ratio of the normalized stress peaks is proportional to Γ_i as predicted from the modal analysis.

A comparison of the three solution methods is shown in Fig. 5 for $Q = 10$. The primary difference between the calculations is the pronounced anti-resonance or dip in the exact response, not present in the single mode power series solution or the modal analysis (four terms are used). Without attempting to quantify the numerical differences, all of these methods are completely suitable for

routine thermowell stress calculations up to the first critical. For the higher order modes, it is necessary to use either the modal analysis or the exact solution. The worst case stresses will be generally associated with a resonant peak.

The calculated drag and vortex shedding stresses for an actual thermowell application are plotted in Fig. 6. The cantilever dimensions and service conditions summarized in the legend are the same as used for the previous figures but with much smaller damping ($Q = 100$), so that the magnification ratio at the first critical ~ 50 . The drag stress increases with the square of velocity. The vortex shedding stresses on the other hand are characterized by a succession of resonances and anti-resonances. The resonant peaks are proportional to the product of the mode participation factor and the drag stress.

The maximum allowable stress for static and cyclical loads are also shown in Fig. 6 for

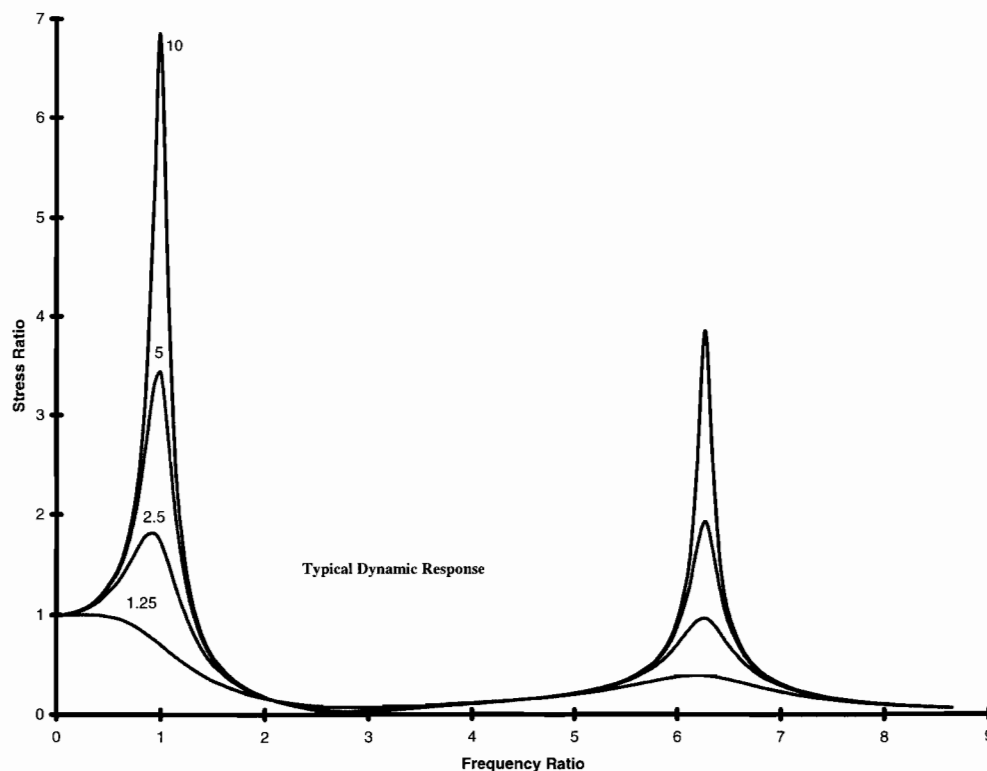


Fig. 4. Normalized stress (vortex shedding/conventional drag) versus normalized frequency. System Q is shown as a parameter.

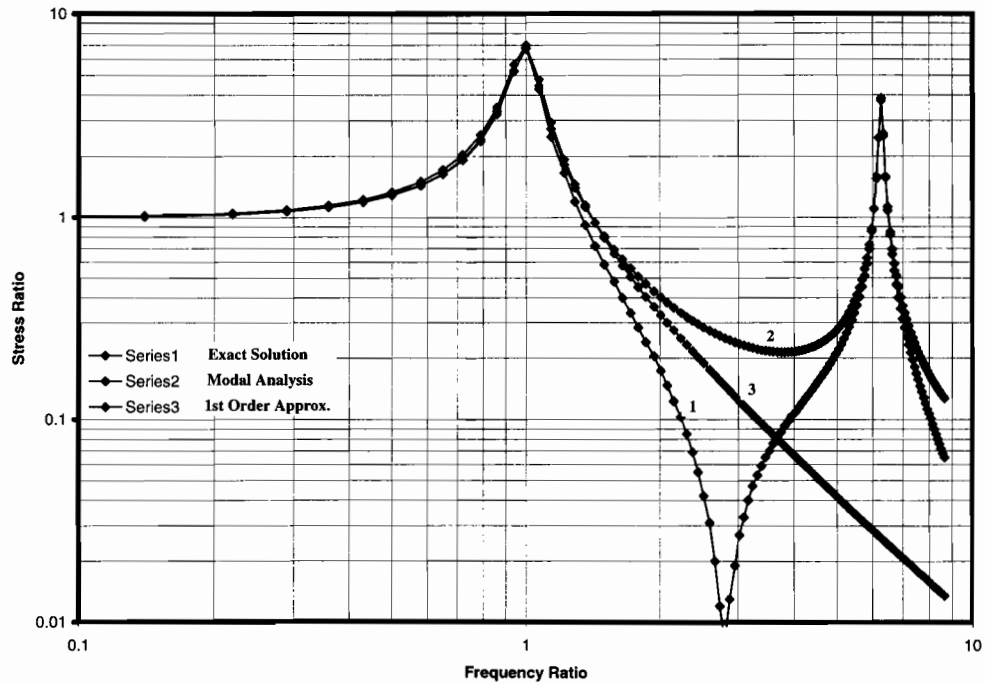


Fig. 5. Comparison of the exact calculation with the modal analysis for Q of 10.

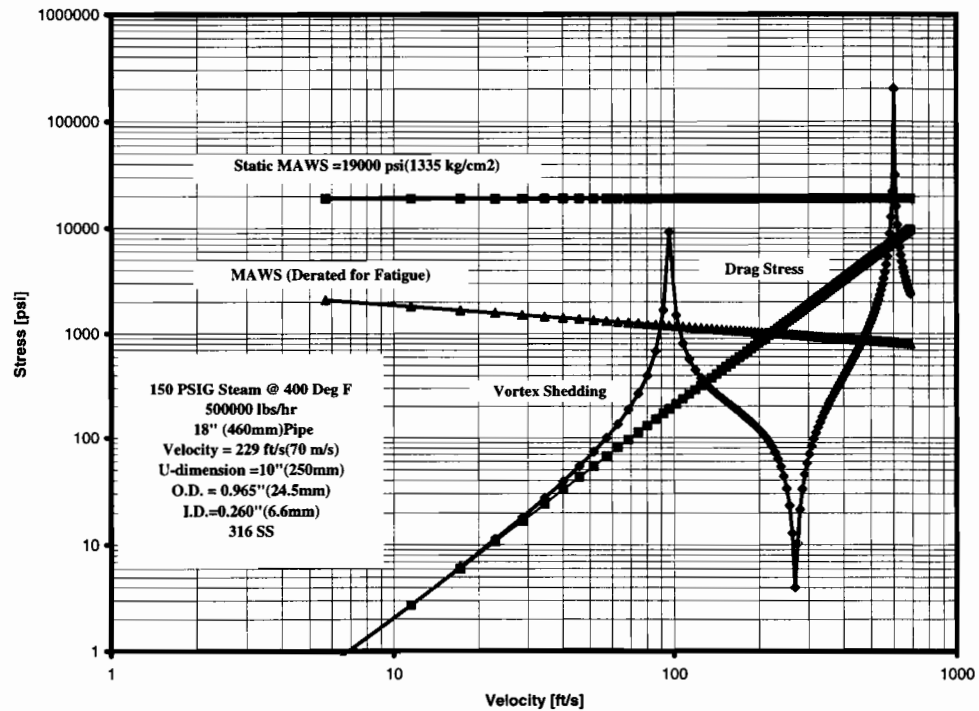


Fig. 6. Plot of dynamic stress as a function of steam velocity for a representative thermowell.

comparison. In this example, the second critical is well beyond the normal range of steam velocities commonly found in closed systems. Higher order modes are a more common issue only in long protection tube designs.

8. Maximum allowable stresses

The PTC is specific to severe service steam applications, but in practice it is used as the starting point for thermowell design and application for all services. It also requires that the sum of the hydrostatic, drag, and vortex shedding stresses do not exceed the maximum allowable working stress, and that the stream velocity be limited to 80% of the first critical. These are realistic criteria in extreme services where resonance must be avoided at all times as is the case in high velocity steam applications or where thermowells are located upstream of rotating equipment.

However, when these criteria are applied to less severe services, the velocity rating can be so restrictive as to impair measurement accuracy. Although the code acknowledges the importance of measurement accuracy, it does not address the consequences of extremely low critical velocities. When damping is included, even if only approximate, the criterion for thermowell velocity ratings is reduced to a stress condition and it is seen that low velocity resonances can be ignored in certain cases.

Additionally, the PTC takes the approach of using the maximum allowable working stress of the material based on its use in piping systems. This allowable is based on a 20 year service life with a daily stress cycle, i.e. 7000 stress cycles. Clearly this is not the case here, where the stress cycles occur at several hundred cycles per second. In spite of this, none of the published thermowell literature suggests that the allowable stresses need to be derated. Where corrosion fatigue is expected, particularly in non-steam applications, it is suggested that the allowable stresses be derated. This is especially true where hydrogen embrittlement or stress corrosion cracking is a concern.

Fatigue allowances are never exact, but a design allowance for them is essential. When fatigue data

are not available for a given design, the allowable stress can be derated by a factor which based on the number of stress cycles as is done in piping systems [8]. This is based on the observation that the cycles to failure is inversely related to the 5th power of the stress amplitude [8], so that the maximum allowable stress for static conditions must be reduced by the factor of

$$K \sim 6N^{-1/5} \quad (30)$$

to account for the cyclical nature of stress, where N is the number of cycles. For a nominal duration of 10^8 cycles, the maximum allowable cyclical stress is reduced to ~15% of the allowable working stress for static loads. Considering the uncertainties in the flow conditions for the average application and the rate at which stresses increase with velocity, this derating is not as severe as it seems.

9. Conclusions

Dynamic stress analysis can be routinely applied in the application phase of thermowell selection. The real benefits of such an analysis are process specific estimates of the static and dynamic stress levels. The key is including dynamic losses in the stress model.

The analysis can be developed from first principles or by an extension of the existing PTC model. The choice of model depends on the range of velocities being considered and the degree of completeness required. In the case of severe service thermowells a damped spring-mass resonance is completely adequate. In the case of less severe services where the potential of higher order excitations exists, it is necessary to use a more comprehensive solution found in a modal analysis or in the exact solution. When damping is included, the industry practice of selectively ignoring extremely low velocity ratings is partly explained since low velocity resonances are invariably low stress.

Essential to any of these model calculations, is a better understanding of vortex shedding especially at the higher order modes and improved estimates of the dynamic losses. For the present it is necessary

to treat these phenomenologically and adapt a strategy of avoiding high velocity resonances in conjunction with an allowance for corrosion fatigue.

Regardless of the stress model being used and inspite of the uncertainties in the damping parameter, etc., the detailed stress analysis improves the quality of thermowell selection and establishes a systematic basis for mechanical integrity. With the availability of desk top computing, these calculations are reduced to a routine evaluation.

Acknowledgements

Thanks to Paul D. Pate of Monsanto Enviro-Chem Systems, for his able assistance in preparing the figures, and to both J. Sainz and W. J. Meier, of PC&E, for helpful suggestions and comments. Particular thanks to the reviewers for calling attention to modal analysis methods.

References

- [1] J.W. Murdock, Power test code for thermometer wells. ASME Journal of Engineering for Power, Oct 1959: 403–416.
- [2] ASME Power Test Code, PTC 19.3, Part 3: Temperature measurement, 1974.
- [3] C.R. Wylie, Jr., Advanced engineering mathematics, second ed., McGraw-Hill, 1951.
- [4] R.D. Blevins, Flow-induced vibration, second ed., Malarbar FA: Krieger Publishing, 1994.
- [5] R.D. Blevins, B.W. Tilden, D.H. Martens, Vortex-induced vibration and damping of thermowells, ASME Transactions, PVP 328 (1996) 465–484.
- [6] A. Avallone, T. Baumeister, Marks standard handbook for mechanical engineers, ninth ed., McGraw-Hill, 1987.
- [7] W.T. Thompson, M.D. Dahleh, Theory of vibration, fifth ed., Prentice-Hall, 1998.
- [8] ASME Boiler and Pressure Vessel Code, Section III, Appendix N: flow-induced vibration of tubes and tube banks, 1992.
- [9] W. Weaver, Jr., S.P. Timoshenko, D.H. Young, Vibration problems in engineering, fifth ed., John Wiley & Sons, 1990.
- [10] R.D. Blevins, Formulas for natural frequency and mode shape, Malarbar FA. Krieger Publishing, 1984.

ISA TRANSACTIONS

Notes for Contributors

Submission

Authors should submit **five** copies of their contribution to the Editor-in-Chief, whose address can be found on the journal's inside front cover.

All papers will be reviewed and assessed by independent referees.

Manuscripts

Manuscripts should be typed in double spacing on one side of A4 paper with wide margins. All pages should be numbered consecutively.

Language

The language of the journal is English.

Style

The manuscript should be organized in the following order: *Title*; *authors and affiliations*; *abstract* (not exceeding 200 words in length); *keywords*; *main body of paper* (divided into numbered sections and subsections); *acknowledgement* (where applicable); *references*; *appendices* (where applicable). An abbreviated title of less than 40 characters (including spaces) should also be suggested.

Illustrations

Photographs, charts and diagrams are to be referred to as 'Figure(s)' and should be numbered consecutively in the order in which they are first mentioned. They should accompany the manuscript but should not be included in the manuscript pages.

Original line drawings or glossy prints (preferably not photocopies), suitable for immediate reproduction, should be submitted. All illustrations should be clear and suitable for reduction (to 50% original size). Lettering must be clear and open and must also be large enough to be reduced by the same proportion.

Figure legends should be typed on a separate sheet and placed at the end of the manuscript. The amount of lettering on a drawing should be reduced as far as possible by transferring it to the legend.

Mathematical expressions

Mathematical symbols and formulae should be typed. Particular care should be exercised in identifying all symbols and in avoiding ambiguities. Distinction should be made between the number one (1) and the letter l, and between the number zero (0) and the letter O.

Vectors and tensors should be marked clearly on the manuscript.

Equation numbers should appear in parentheses; equations must be numbered consecutively. All equation numbers must appear on the right-hand side of the equation and should be referred to within the text.

Use the following sequence of parentheses:)] }.

Tables

Particular care is needed to ensure that tables are clearly and legibly set out.

References

References to published literature should be quoted in the text by numbers in square brackets, [1].

References should be listed together at the end of the paper in numerical order. Double-spacing must be used throughout. Journal references should be arranged thus:

- [1] A. Paivio, B. Jansen, L.J. Becker, Comparisons through the mind's eye, *Cognition* 37 (2) (1975) 635-647.

Book references are given as follows:

- [2] W. Strunk Jr., E.B. White, *The Elements of Style*, 3rd ed., Macmillan, New York, 1979.

Units

All measurements and data should be given in SI units, or, where SI units do not exist, in an internationally accepted unit. Each paper should be self-consistent as to symbols and units which should all be properly defined.

Proofs

Page proofs will be sent to the author (or the first-mentioned author in papers of multiple authorship unless otherwise indicated) for checking. The corresponding author should supply a full postal address, and where possible, a fax number. *Corrections to the proofs must be restricted to printer's errors: any other changes to the text, in equations or grammar, may be charged to the author.* Authors will be asked to return proofs within 48 hours of receipt.

The original manuscript and diagrams will be discarded one month after publication unless the publisher is requested to return original material to the author.

Reprints

The corresponding author will receive 50 offprints of the paper free of charge. Extra reprints and copies of the journal may be ordered using the order form that accompanies the proofs.

Copyright and originality

All authors must sign the 'Transfer of Copyright' agreement before the article can be published. This transfer enables Elsevier Science Ltd to protect the copyrighted material for the authors, but does not relinquish the author's proprietary rights. The copyright transfer covers the exclusive rights to reproduce and distribute the article, including reprints, photographic reproductions, microform or other reproductions of similar nature and translations, and includes the right to adapt the article for use in conjunction with computer systems and programs, including reproduction or publication in machine-readable form and incorporation in retrieval systems. Authors are responsible for obtaining from the copyright holder permission to reproduce any figures for which copyright exists.

Submission of ACCEPTED articles on disk

Authors are requested, where possible, to submit electronic versions of *accepted* papers. Refer to the advert published in most issues for full details.

ELSEVIER SCIENCE

prefers the submission of electronic manuscripts

Electronic manuscripts have the advantage that there is no need for the rekeying of text, thereby avoiding the possibility of introducing errors and resulting in reliable and fast delivery of proofs.



The preferred storage medium is a 5.25 or 3.5 inch disk in MS-DOS format, although other systems are welcome, e.g. Macintosh.



After **final acceptance**, your disk plus one final, printed and exactly matching version (as a printout) should be submitted together to the accepting editor. **It is important that the file on disk and the printout are identical.** Both will then be forwarded by the editor to Elsevier.



Please follow the general instructions on style/arrangement and, in particular, the reference style of this journal as given in "Instructions to Authors."



Please label the disk with your name, the software & hardware used and the name of the file to be processed.



ISA TRANSACTIONS



Please send me a free sample copy



Please send me subscription information



Please send me Instructions to Authors

Name

Address



ELSEVIER
SCIENCE
B.V.

Send this coupon or a photocopy to:

ELSEVIER SCIENCE B.V.

Attn: Engineering and Technology Department
P.O. Box 1991, 100 BZ Amsterdam, The Netherlands

Static and dynamic stresses of practical thermowells

David S. Bartran^{a,*}, Donald R. Frikken^b, Jerry M. Kinsey^a,
Robert Schappelle^c, Richard Yee^a

^aMonsanto Enviro-Chem Systems, 14522 South Outer Forty Road, Chesterfield, MO 63017, USA

^bSolutia Inc., Chesterfield, MO, USA

^cBAE Systems, Inc., San Diego, CA, USA

Abstract

A flexible beam model is proposed for calculating the flow induced stresses and application limits of common thermowell designs. It is intended to replace traditional selection methods with one which emphasizes mechanical integrity and process containment. © 2000 Elsevier Science Ltd. All rights reserved.

1. Introduction

When dynamic analysis methods are used to evaluate thermowell application stresses, it is soon discovered that traditional application rules result in a surprising number of instances where thermowell failure is likely to occur. This is not restricted to high pressure steam services, but includes the full range of liquid and gas applications.

Historically, the Murdock thermowell stress model [1] and the accompanying ASME Performance Test Code, PTC 19.3 [2] deal with the relationship between thermowell design and dynamic ratings in high pressure steam applications. They address the issues of vortex shedding, flow induced resonance, and material strength in establishing the dynamic ratings of the thermowell and are the accepted basis for published velocity ratings in North America. While the PTC model is not without its failings, its predictions are frequently ignored

in an attempt to reduce the effects of conduction errors and the effects of process stratification.

For example, traditional thermowell selection methods are commonly based on a fixed ratio of thermowell length to pipe size. The result is a sizable number of thermowells being exposed to resonant conditions as the pipe size is increased. This was confirmed in a dynamic analysis of over eighty thermowells, selected by traditional means. Over a third of the applications were at risk of mechanical resonance and two of the highest stress applications were upstream of rotating equipment.

After demonstrating that the percentage of thermowells at risk was not significantly altered by changing the ratio of thermowell length to pipe size and the calculation method was demonstrated to be a conservative estimate, the traditional selection rules were abandoned altogether.

Obviously, a more comprehensive selection process is needed, one based on the actual service stresses rather than arbitrary rules or generic velocity rating tables. Unfortunately, the PTC model, so often used to establish the thermowell velocity ratings, cannot be used for this purpose,

* Corresponding author. Tel.: +1-314-275-5869; fax: +1-314-275-5942.

E-mail address: david.s.bartran@monsanto.com (D.S. Bartran).

because it is based on a stress model that pre-disposes thermowells to tensile failure.

2. Cantilever in a flowing media

2.1. Continuous beam model

Consider a slender beam, attached to an infinite half-plane and extending into a fluid stream as shown in Fig. 1. The fluid motion acts to deflect the beam with a force consisting of static and time dependent components. The bending mode response is described by the Euler–Bernoulli equation [4,5]:

$$\frac{\partial^2}{\partial x^2} [EI(x) \frac{\partial^2}{\partial x^2} \xi(x, t)] = -\mu(x) \frac{\partial^2}{\partial t^2} \xi(x, t) + \mathbf{F}(x, t) - \alpha \frac{\partial}{\partial t} \xi(x, t) \quad (1)$$

with centerline deflection, $\xi(x, t)$ having components parallel to and transverse to the direction of fluid flow. The beam is characterized by a modulus of elasticity, E , a moment of inertia, $I(x)$, a mass per unit length, $\mu(x)$, a viscous damping coefficient, α , acting to oppose motion, and a generalized excitation force, $\mathbf{F}(x, t)$. The dynamic equation is written in vector notation under the proviso, that only small amplitude displacements are considered.

The coordinate system is defined, such that the tip of the undisturbed cantilever is located at the

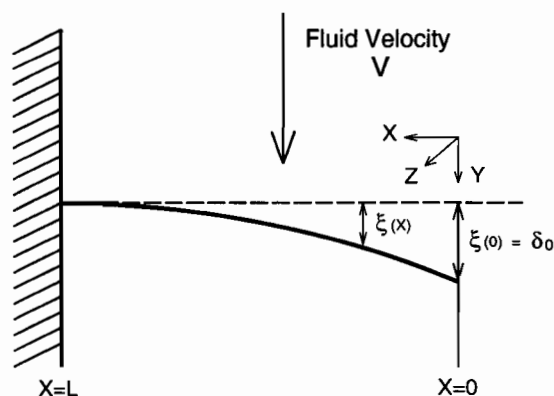


Fig. 1. Cantilever coordinates for the continuous beam model.

origin. The solution must satisfy the standard set of boundary conditions for a beam clamped at the base and free at the end. The stress response is related to the thermowell deflection by the auxiliary relation:

$$\sigma(x) = D(x) E \xi''(x, t) / 2, \quad (2)$$

where partial derivative operations are represented as $\xi' = \partial/\partial x(\xi)$.

2.2. Fluid drag and vortex shedding

The forces acting on the thermowell result from the change in momentum when the fluid path is disturbed. This results in a time averaged force acting to bend the thermowell in the flow direction (conventional drag) and periodic, approximately sinusoidal components acting parallel to the flow direction (oscillating drag) and transverse to the flow direction (oscillating lift) as shown in Fig. 2. The oscillating components are associated with the initiation and release of von Karman vortices from alternate sides of the thermowell.

The lineal force density [6] acting on the beam is given by:

$$\mathbf{F}(x, t) = (F_D + F_d \sin 2\omega t) \mathbf{y} + F_K \cos \omega t \mathbf{z}, \quad (3)$$

where the components of force have the form: $F_\beta = \rho_f D(x) C_\beta V^2 / 2$, where the subscript $\beta = \{D, d, K\}$, corresponds to drag, oscillating drag, and oscillating lift components, respectively. The vortex shedding frequency is roughly linear with

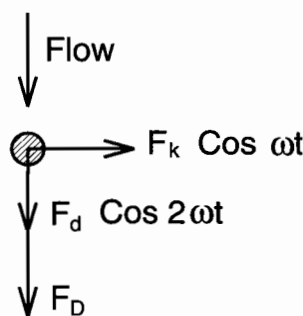


Fig. 2. Transverse forces acting on the thermowell.

the average fluid velocity: $\omega = 2\pi SV/D$, with a Strouhal number, $S \sim 0.22$.

2.3. Generalized response

The complete solution consists of a static component, $\delta(x)$, associated with fluid drag acting in the flow direction, \mathbf{y} , and a dynamic component, $\eta(x, \omega)$, associated with oscillating lift in the transverse direction, \mathbf{z} :

$$\xi(x, \omega) = [\delta(x) + \varepsilon(x, \omega)e^{j2\omega t}]\mathbf{y} + \eta(x, \omega)e^{j\omega t}\mathbf{z}. \quad (4)$$

The static solution, $\delta(x)$, is calculated by finite element methods for a uniform flow profile while the dynamic solutions for oscillating drag $\varepsilon(x, \omega)$, and oscillating lift, $\eta(x, \omega)$, are calculated as an expansion of normal modes, φ_i [4]. The static response and the normal modes are calculated using finite element methods.

The dynamic responses are expanded as summations of orthogonal functions [4] as follows:

$$\varepsilon(x, \omega) \sim \sum p_i(\omega)\varphi_i(x), i = 1, 2, 3 \dots \quad (5)$$

for the oscillating drag and

$$\eta(x, \omega) \sim \sum q_i(\omega)\varphi_i(x), i = 1, 2, 3 \dots \quad (6)$$

for the oscillating lift. The expansion coefficients $\{p_i, q_i\}$ are the modal amplitudes.

Orthogonality has the useful property that the product of any two functions in the set satisfy:

$$\int \varphi_i \varphi_j dx = 0 \text{ for } i \neq j \quad (7)$$

and

$$\int \varphi_i \varphi_j dx = L \text{ for } i = j. \quad (8)$$

Associated with the normal modes are the generalized stiffness and mass coefficients, κ_{ij}, μ_{ij} , are given by:

$$\begin{aligned} \kappa_{ij} = & \int EI(x)\varphi_i''\varphi_j'' dx + 2 \int EI'(x)\varphi_i''\varphi_j' dx \\ & + \int EI''(x)\varphi_i'\varphi_j' dx \end{aligned} \quad (9)$$

and

$$\mu_{ij} = \int \mu(x)\varphi_i\varphi_j dx. \quad (10)$$

The assumption of a coherent vortex shedding process results in a separable excitation model [7], so that a modal participation can be defined. With $F(x, \omega) = F_0 f(x)e^{j\omega t}$, where $F_0 \equiv \rho_f C_D V^2 A/2$ and $f(x) \equiv D(x)/A$, the modal participation factor is:

$$\Gamma_i = L^{-1} \int f(x)\varphi_i dx. \quad (11)$$

The effective mode constant, γ_i , is calculated in terms of the critical frequency, modal stiffness, and mass as:

$$\gamma_i^2 \equiv \omega_i L^2 (\kappa_{ii}/\mu_{ii})^{-0.5}. \quad (12)$$

These generalized coefficients allow a convenient representation of the dynamic equation in matrix form:

$$[(\gamma_i/L)^4 \kappa_{ii} - \mu_{ii} \omega^2 (1 - j\alpha/\omega \mu_{ii})] \{q_i(\omega)\} = \{\Gamma_i\} F_0. \quad (13)$$

The square brackets, $[]$, are used to indicate the square coefficient matrix and braces, $\{ \}$, column vectors. If the basis functions are actual solutions to the homogeneous equation, then the off-diagonal terms are identically zero. Since approximate modes are used, off-diagonal terms are expected in both the stiffness and mass matrices, which represent higher order interactions (non-linear terms). Ignoring these interactions, the modal amplitudes are obtained by simple division. A similar set of equations can be written for the oscillating drag response. The longitudinal stresses are obtained by applying the auxiliary relation, Eq. (2) to the respective deflection responses.

3. Critical frequencies

The critical frequencies of the thermowell serve as a focal point for the data essential to any stress

calculation capable of characterizing the flow induced stresses. These estimates should have a rigorous theoretical basis, allow for sensor mass, temperature effects, materials of construction, and added mass of the fluid [8].

Common manufacturing tolerances of thermowell length are on the order of $\sim 1\%$. This suggests that the minimum level of accuracy needed for evaluating industrial applications, as defined by $\Delta\omega/\omega_i \sim 2(\Delta L/L)$, is on the order of 2% . This is well within the capability of the finite element calculation or the analytical solutions. The criticals predicted by the finite element model are consistently within $\sim 0.25\%$ of those derived from analytical solutions for the uniform, piecewise uniform, and linearly tapered beams, with 512 elements in the model. Accuracy of the critical estimate is inversely related to the number of elements used in the calculation.

The critical frequency measurements published by Blevins et al. [9] offers a practical test of the finite element method. The test fixture used for these measurements is representative of a common class of thermowell installations involving a flanged pipe stub. Initially, the finite element method was found to consistently over-estimate the measured frequencies by an average of $\sim 4\%$ for the first and ~ 5 to $\sim 15\%$ for the higher order criticals with a 50 mm stub length.

This discrepancy was several times larger than expected, given close agreement between the finite element calculation and analytical solutions. However, when the test fixture, as a flanged pipe stub, was included in the critical frequency calculations, the discrepancies were reduced to less than $\sim 0.7\%$ for the first and less than $\sim 0.8\%$ for the second critical. The third critical could not be consistently predicted, because of the overlap between the fixture and thermowell modes.

Fixture parasitics are not just an academic issue. With flanged stubs as long as 250 mm in practical installations, the fixture itself may be excited to resonance by the flowing forces acting on the thermowell. Such installations should be carefully evaluated in any high velocity service, even if the thermowell is only partially exposed. Close-coupled mounting is recommended in all high velocity applications.

4. Design criteria for thermowells

4.1. Current design practice

Currently, the allowable design stresses of thermowells are not formally covered by any code or standard. Murdock recognized the benefits of having a commonly agreed basis for setting the allowable stress and suggested that the Boiler and Pressure Vessel Codes [10] be used for this purpose. This was later extended to include the Piping Codes [11], but without clarification.

In the current PTC, the thermowell is viewed as a small diameter pressure vessel with shear stress on the inner wall controlling the design. However, with all due respect, thermowell failures do not normally originate on the inside of the thermowell but rather on the outside, where the bending stresses and risk of corrosion are greatest.

Except for differences in how bending and static pressure stresses are combined in the flexible beam model, the piping codes practically describe the design requirements of the thermowell. Full advantage is taken of this fact in using the piping codes as the basis for allowable stress data for both static pressure and dynamic ratings. The most common piping codes are B31.1, for *Power Piping* and B31.3, for *Process Piping*.

4.2. Static pressure stresses

The primary stresses in the thermowell shank are axial, radial, and tangential. The axial stress is given by the hydrostatic load acting on the thermowell cross-section, while the radial and tangential (hoop) stresses are given by the Lamé formulas [12,13] for a thick walled tube. The greatest pressure stresses (hoop) occur on the inner wall, at a location where the wall thickness is smallest (usually near the tip):

$$S_l = P_o B^2 / (B^2 - d^2) \quad (14)$$

$$S_r = 0 \quad (15)$$

$$S_\theta = 2P_o B^2 / (B^2 - d^2). \quad (16)$$

The dimensions are in Fig. 3.

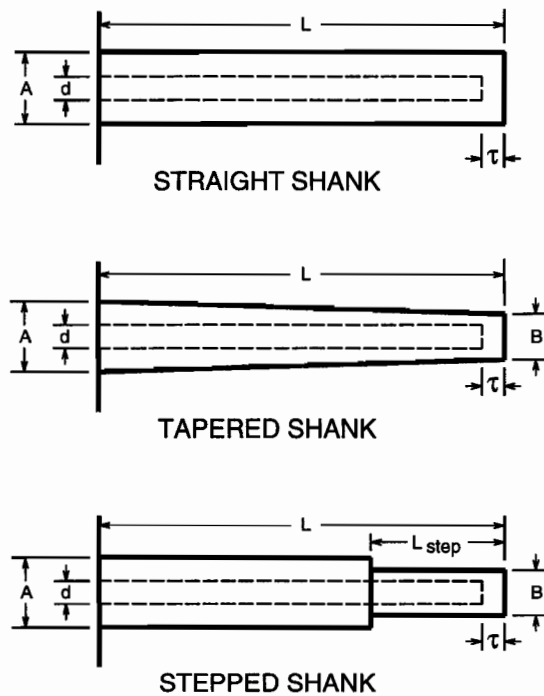


Fig. 3. Common thermowell designs: straight, tapered, and stepped.

The hoop stress on the inner wall of the thermowell controls and establishes the minimum wall thickness of the thermowell shank and the static pressure rating of the thermowell.

4.3. Tip stresses

The closed end tip of the thermowell deserves special attention. For design purposes it can be approximated as a thick circular plate *clamped* at its rim, with a diameter equal to the bore, d , and with thickness, τ . With uniformly distributed hydrostatic pressure, the peak radial stress in the plate [13] is given by:

$$S_r \sim 3P_o(d/\tau)^2/16. \quad (17)$$

Where the tip thickness is not uniform, use of the minimum thickness establishes the worst case stress. The PTC does not consider tip stresses explicitly, but requires that the tip thickness be set equal to the minimum wall thickness of the shank

[1]. However, this is not sufficient in the case of large bore or pipe type thermowells.

4.4. Combined longitudinal stresses

The longitudinal bending stresses of the thermowell increase with flow while the hoop stresses remain constant and at some point control design. For a representative thermowell, this transition occurs at ~ 15 m/s for compressible fluids including steam and at ~ 1.5 m/s for liquids; dynamic effects should be considered in most applications.

Above the transition velocity, the principle stress is dominated by the combined longitudinal stress. It includes the hydrostatic thrust, S_l , conventional drag, S_D , oscillating drag, S_d , and oscillating lift, S_K stresses:

$$S_l = P_o A^2 / (A^2 - d^2) \quad (18)$$

$$S_D = \sigma_D \quad (19)$$

$$S_d = \sigma_d \left| \Sigma 4\gamma_i^{-2} \Gamma_i [1 - (2\omega/\omega_i)^2 + 4j\zeta_i \omega/\omega_i]^{-1} + \Delta \right| \quad (20)$$

$$S_K = \sigma_D \left| \Sigma 4\gamma_i^{-2} \Gamma_i [1 - (\omega/\omega_i)^2 + 2j\zeta_i \omega/\omega_i]^{-1} + \Delta \right| \quad (21)$$

When the summation is performed only over a finite number of modes, all higher order modes are sub-resonant and results in a additive term, $\Delta \equiv 1 - \Sigma 4\gamma_i^{-2} \Gamma_i$. The drag stress and oscillating drag constants, σ_D and σ_d , are functions of the fluid velocity but parametric in the vortex shedding frequency, and are calculated at each velocity by finite element methods. The relative damping is related to the viscous damping parameter by $\zeta_i = \alpha\omega/2\mu_{ii}$. The drag stress for a uniform beam is $\sigma_D = \rho_f C_D A^2 L^2 V^2 / 8I$.

The peak stress is defined as the *sum of the absolute component values*. While a more definitive estimate is possible, it is hardly worth using, given the usually uncertainty in flow conditions. A definition based on the root-means-square of the stress components [3] under-estimates the peak stress and should not be used.

For design, the peak stress must be less than or equal to the maximum allowable (tensile) stress for the material i.e.

$$|S_I| + |S_D| + |S_d| + |S_K| \leq K S_m. \quad (22)$$

A fatigue de-rating factor, K , is included in the design criteria. In non-corrosive services, de-rating may be unnecessary [9] for common materials.

4.5. Sensor stresses

The acceleration stress experienced by a temperature sensor placed in the thermowell is given by the second order derivative in time of the deflection response. Unlike the peak stresses, the combined amplitude of the acceleration stress is given by the root-mean-square of the oscillating drag and oscillating lift components.

While there is very little data regarding allowable sensor stress under sustained vibration, it cannot be ignored. It is not uncommon for the predicted stresses to exceed 50–100 g near resonance. Some sensor designs appear to be resistant to vibration (> 50 g), but others are not (< 5 g). Even limiting acceleration stress to 5–10 g, is frequently more restrictive than the allowable design stresses of the thermowell.

5. Sample calculations

Several examples of the proposed stress model are considered. The first is taken from PTC 19.3 while the remaining examples represent thermowells which have actually failed in service. The same calculation procedure is used for all thermowells with the drag stresses, critical frequencies and other modal constants are calculated using the finite element method with 512 elements. The modal constants are estimated for the first four modes, all others assumed to be non-resonant, and the damping parameter is arbitrarily set so that the relative damping for the first critical is fixed at 1%. The modal analysis is performed for the range of fluid velocities that span the given application and the peak longitudinal stress is plotted. The drag and oscillating lift coefficients are both

set to unity, and the oscillating drag is set at a tenth of the oscillating lift. Customary US units have been used to simplify comparison with the original PTC example.

The predicted longitudinal stresses for the PTC [2] example are shown in Fig. 4. This is a thin walled, tapered thermowell, with dimensions and process conditions shown in the figure. Note that the longitudinal stress dominated by static pressure stresses at low velocities and by the flow induced stresses and resonance at high velocities. The two resonant peaks correspond to oscillating drag and oscillating lift excitation of the first order critical of the thermowell.

Oscillating drag results in a stress peak just below 300 ft/s (91 m/s), the given service velocity, with oscillating lift dominating the response at ~ 575 ft/s (175 m/s). Since this is a power station example, the piping and the thermowell are designed to the maximum allowable tensile stress permitted under B31.1 for Power Piping. The maximum allowable stress at the service temperature, shown on the graph, limits the design to ~ 275 ft/s (84 m/s).

A direct comparison with the PTC is difficult since it does not include oscillating drag and relies on an incorrect representation of resonance. However, after correcting the magnification ratio and using the actual, rather than the estimated, critical frequency of the thermowell, the maximum allowable stress condition limits the service velocity to ~ 392 ft/s (120 m/s). This is some 50% higher than the velocity allowed under the proposed model. In fact, if this thermowell is operated at the higher rating, it is likely to experience tensile failure!

Additional examples considered in Figs. 5–7, document applications where actual failures have been reported. The actual service temperature, pressures and fluid are indicated, but the calculation is performed using the nominal properties for 316 stainless steel with the allowable stresses taken from B31.3 for Process Piping. In each case, the proposed stress model correctly identifies the potential for failure.

The second example shown in Fig. 5, is a thermowell in which a resistance sensor failed where the extension wires were attached. The normal

- [6] R.D. Blevins, *Flow-Induced Vibration*, Krieger Publishing, Malarbar, FL, 1994.
- [7] D.S. Bartran, J.M. Kinsey, R. Schappelle, R. Yee, Flow induced vibration of thermowells, *ISA Transactions* 38 (1999) 123–132.
- [8] R.D. Blevins, *Formulas for Natural Frequency and Mode Shape*, Krieger Publishing, Malarbar, FL, 1984.
- [9] R.D. Blevins, B.W. Tilden, D.H. Martens, Vortex-induced vibration and damping of thermowells, *ASME Transactions*, PVP-Vol. 328, 1996, pp. 465–484.
- [10] ASME Boiler and Pressure Vessel Code.
- [11] ASME Code for Pressure Piping, B31.
- [12] J.C. Jaeger, N.G.W. Cook, *Fundamentals of Rock Mechanics*, 3rd Edition, Chapman and Hall (Methuen), 1979.
- [13] A. Avallone, T. Baumeister, *Marks Standard Handbook for Mechanical Engineers*, 9th Edition, McGraw-Hill, 1987.

flow condition approximately coincides with the resonance condition for oscillating drag and results in acceleration stresses exceeding ~ 5 g.

The third example, Fig. 6, is a documented failure [3] of a thermowell in a liquid sodium coolant loop where the process containment was lost. The normal flow condition coincides with the first critical of the thermowell (oscillating drag) and the potential for failure is evident even without derating for fatigue. Use of a tapered thermowell design, as recommended by the authors [3], increases the critical velocity by a factor of three and reduces the root stresses by an order of magnitude.

The fourth example, Fig. 7, documents a second hand report of a thermowell failure. Here the normal expected flow coincides with the resonance condition (oscillating lift) for a thermowell whose length was set at 40% of the pipe diameter. Again, the potential for thermowell failure is obvious. In this case the damaged thermowell was replaced by a longer one with good results, but a practice only recommended where a careful assessment of the thermowell stresses have been made.

6. Conclusions

Dynamic analysis of the thermowell as a flexible beam is the most effective method for predicting thermowell mis-application. However, it must be used in conjunction with a conservative estimate of the peak stresses and a realistic criteria of failure (allowable stresses). The Piping Codes offer the most reliable collection of material designations and allowable stress data suitable for thermowell manufacture. Their use insures designs which are compatible with the adjacent piping. This is demonstrated by an evaluation of several documented thermowell failures, which could have been avoided.

Though frequently cited as a basis for design, the PTC 19.3 is based on an in-complete stress model and results in thermowell designs predisposed to tensile failure. Traditional selection methods which focus exclusively on measurement accuracy or response time, offer little or no help, being equally prone to thermowell mis-application.

Both methods should be abandoned and replaced by either a thermowell selection based on a comprehensive stress analysis or a velocity rating method based on such an analysis. The dynamic analysis need not be overly complex, even a simplified estimate of the conventional drag stresses and the velocity corresponding to the onset of resonance can be used to define the operating envelope of the thermowell.

Where analysis is not possible, the fluid velocity is high, i.e. > 30 m/s for gas and steam and > 3 m/s for liquids, the thermowell length should be restricted to 50 and 100 mm, respectively. While these length requirements can be relaxed somewhat if the thermowells are installed in an elbow or inclined relative to the flow direction, or if tapered thermowell designs are considered, these design options can only be exercised to their fullest extent when a dynamic analysis is performed.

Acknowledgements

Thanks to Ron Haupt of Pressure Piping, Engineering Consultants, Inc. whose comments have been especially helpful in putting the thermowell design requirements in perspective, Paul D. Pate of Monsanto Enviro-Chem Systems, for preparing the figures, and special thanks to Julie Dunn for assistance with the physical layout of the manuscript.

References

- [1] J.W. Murdock, Power test code for thermometer wells, *ASME Journal of Engineering for Power*, October (1959) 403–416.
- [2] Performance Test Code, PTC 19. 3: Temperature Measurement, ASME, 1974.
- [3] K. Dozaki, M. Morishita, K. Iwata, Modification and design guide of thermowell for Fast Breeder Reactors, *ASME Transactions*, PVP-Vol. 363, 1998.
- [4] W.T. Thompson, M.D. Dahleh, *Theory of Vibration*, 5th Edition, Prentice Hall, 1998.
- [5] W. Weaver Jr., S.P. Timoshenko, D.H. Young, *Vibration Problems in Engineering*, 5th Edition, John Wiley & Sons, 1990.

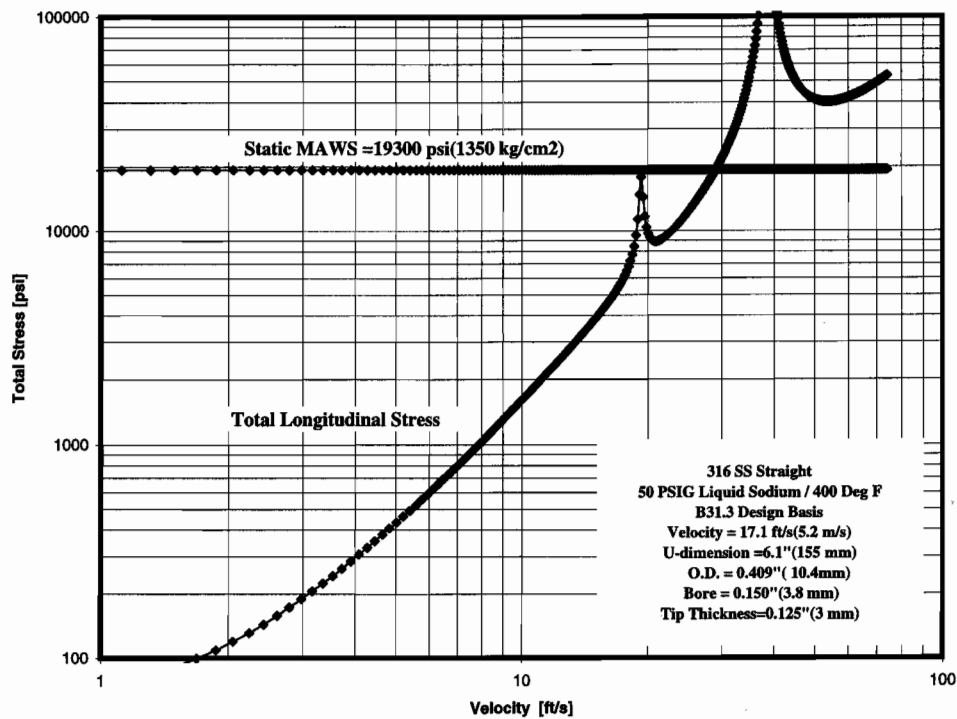


Fig. 6. An application in which stress cracking at the onset of resonance resulted in loss of process containment and fire.

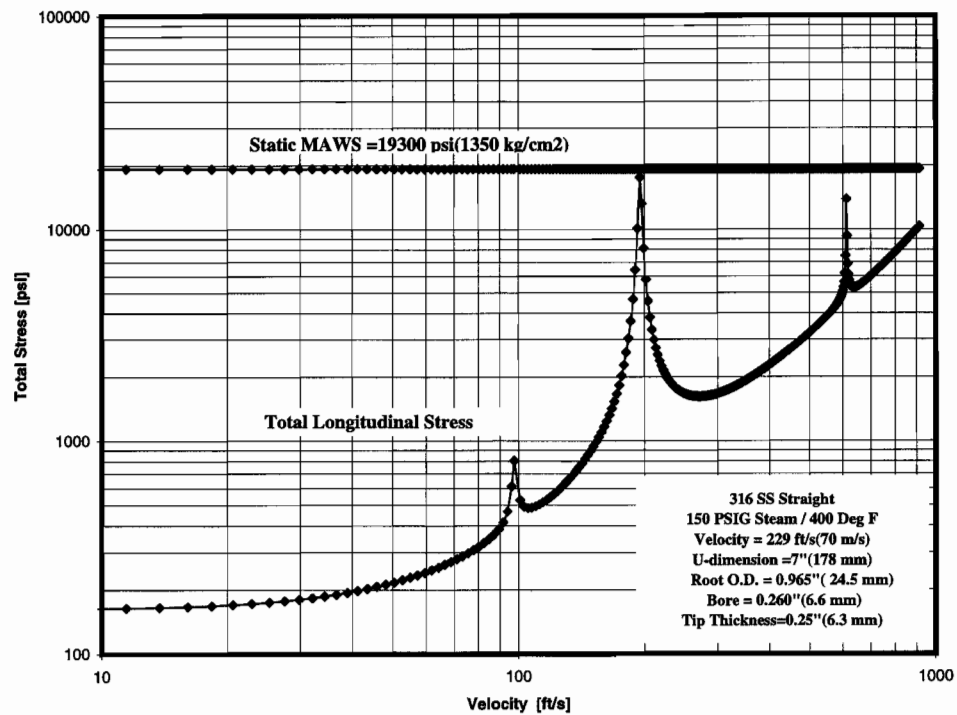


Fig. 7. A moderate pressure steam application exposed to high velocity resonance and reportedly bent in service.

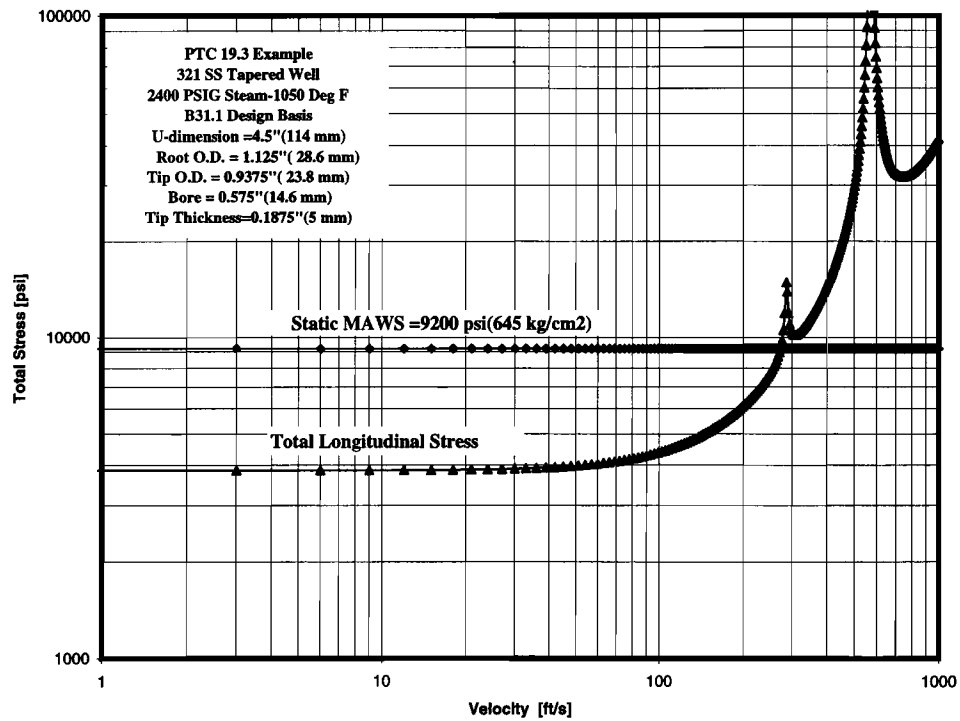


Fig. 4. Longitudinal stress for PTC design, pre-disposed to tensile failure.

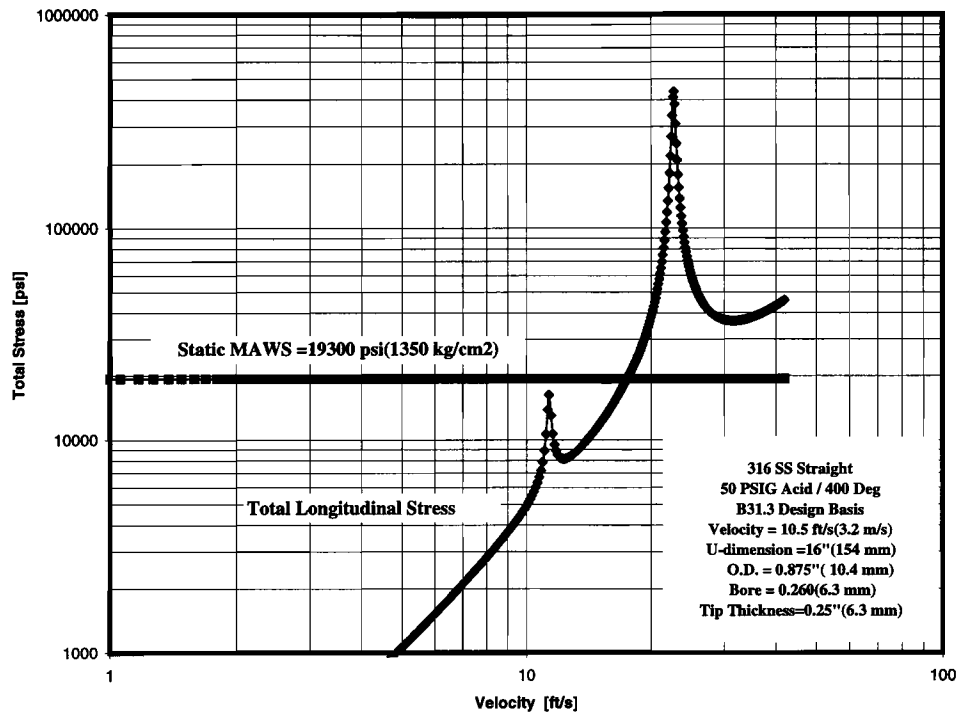


Fig. 5. An application where sensor failure occurred at onset of resonance.

Oct. 2, 2000
DRAFT - ACCEPTED FOR PUBL.
"HYDROCARBON PROCESSING" ZSF

Thermowell Design and Selection

David S. Bartran, Jerry M. Kinsey, Donald R. Frikken*

William J. Meier, Keith E. Patty, Tu T. Phan, Richard Yee

Monsanto Enviro-Chem Systems, Chesterfield Missouri 63017.

*Solutia Inc., Chesterfield Missouri 63017

Abstract

Dynamic analysis techniques are used to identify high risk thermowell applications.

Introduction

Specification of the pressure rating and use of corrosion resistant materials is usually sufficient to guarantee the mechanical integrity of thermowells. However, in high velocity fluids, a more comprehensive basis for selection is needed.

Current velocity rating tables are usually based on a nominal steam or condensate service to serve as a guide for thermowell selection. Murdock's stress model and its companion, the Performance Test Code, **PTC 19.3**, are the most commonly cited basis for these ratings; however they do not account for all of the service stresses!

To compound these difficulties, traditional thermowell selection methods, based on measurement accuracy, largely ignore velocity ratings. For example, to insure that conduction errors and process stratification are minimized, it is common practice to require that thermowells lengths range from 1/3 to 2/3 of the pipe diameter regardless of the fluid velocity. When dynamic analysis methods were used to evaluate such applications, a survey of some eighty thermowells,

found ~ 30% of the applications susceptible to fatigue failure and ~ 3% at risk of immediate stress failure.

The following calculation outlines a method which identifies high risk applications in the design stage and insures thermowell and sensor integrity.

Thermowell Stresses

Under static conditions, the thermowell design is controlled by the circumferential stresses in the shank caused by pressure. In the presence of flow, however, the longitudinal stresses, increased by the dynamic forces acting to bend the thermowell, Fig(1), dominate the stress model.

The forces acting on the thermowell have the form:

$$\underline{F}(x,t) = (F_D + F_d \sin 2\omega t) \underline{y} + F_k \cos \omega t \underline{z} , \quad (1)$$

where the force components have the form: $F_\beta = \rho_f D(x) C_\beta V^2/2$ where $\beta = \{D, d, k\}$, corresponds to drag, oscillating drag, and oscillating lift components. The oscillating lift coefficient is comparable to the conventional drag coefficient and $C_D \sim 1$, while oscillating drag is only $C_d \sim 0.1$. In spite of its reduced intensity, oscillating drag is capable of forcing the thermowell into resonance at lower velocities than is possible with oscillating lift simply because it occurs at twice the vortex shedding frequency. Resonance can easily increase the stress levels by one to two orders of magnitude above the drag stresses.

To simplify the calculation and to insure a conservative stress estimate, the vortex shedding process is assumed to be span-wise coherent regardless of the thermowell design. The vortex shedding frequency is roughly linear with the average fluid velocity and inversely related to thermowell diameter, D , i.e. $\omega = 2\pi S V/D$, with a Strouhal number, $S \sim 0.22$. Where the thermowell is non-uniform, the tip diameter is used to calculate the vortex shedding frequency. Note that oscillating drag occurs at twice the vortex shedding frequency.

The longitudinal stresses, i.e. due to bending and static pressure, reach a maximum at the base of the thermowell. The stress distribution is similar to that of an eccentrically loaded beam, and the peak stress has the form:

$$S = S_l \pm S_D + S_d \sin 2\omega t + S_k \cos \omega t . \quad (2)$$

The components of stress are: S_l , the static pressure stress, S_D , the drag stress, S_d , the oscillating drag stress, and S_k , oscillating lift stress.

$$S_l = P_o A^2 / (A^2 - d^2) \quad (3)$$

$$S_D = \sigma_D \quad (4)$$

$$S_d = \sigma_d \sum c_i [1 - (2\omega/\omega_i)^2 + 4j \zeta_i \omega/\omega_i]^{-1} , \quad (5)$$

$$S_k = \sigma_k \sum c_i [1 - (\omega/\omega_i)^2 + 2j \zeta_i \omega/\omega_i]^{-1} , \quad (6)$$

with modal amplitudes, c_i , critical frequency, ω_i , and relative damping, ζ_i . For example, the stress amplitudes for a straight shank thermowell have the form $\sigma_\beta = \rho_f C_\beta D^2 L^2 V^2 / 8I$ where $\beta = \{D, d, k\}$.

Design Criteria

The **PTC** only includes conventional drag and oscillating lift in the stress model and is concerned with shear stresses on the *interior surface* of the thermowell. This focus on the shear stresses stems from an earlier view of thermowells as a small bore pressure vessels rather than as flexible beams. It is adequate for low velocity applications where the pressure stresses dominate, but it is inconsistent with the failure characteristics of thermowells generally. In a more comprehensive analysis, the *longitudinal stresses* on the outer surface of the thermowell control the design at high velocities. Thermowells typically experience tensile failure long before the shear limit is reached. As a result the **PTC** model should not be used in its current form.

The design requirements for a principle stress model of the thermowell are essentially those of small diameter tubes subjected to external pressure and bending. These requirements are so close to those established in the piping codes that their use as a source of allowable stress data and material designations is justified. This also insures that the thermowell design is compatible with the adjacent piping. The benefits of this approach are found in several case study examples, which show that failures can be anticipated in the design stage of thermowell selection. The most commonly used ASME piping codes are **B31.1** for Power Piping and **B31.3** for Process Piping.

The static stress, as sum of the absolute values of the stresses caused by pressure and drag should not exceed the maximum allowable stress of the material, i.e.

$$|S_l| + |S_D| \leq \text{MAWS}. \quad (7)$$

Additionally, the high cycle dynamic components should not be allowed to exceed the fatigue allowable

$$|S_d| + |S_k| \leq K \text{ MAWS} \quad (8)$$

where K is the stress-reduction factor for the given application. This new criteria is more restrictive than the previously proposed in those cases where cyclical stresses dominate and corrosion is present.

The static allowable stresses for various materials are tabulated in the piping codes. Allowable stresses for fatigue loadings such as caused by thermowell vibration are frequently lower than the static allowable stress, depending on the number of cycles expected during operation. **B31.1** or **B31.3** rules may be used to determine fatigue allowable stresses. The maximum allowable static stress is used to determine the pressure rating of the shank portion of the thermowell and is in line with current industry practice.

Sample Calculations

Two stress calculations are presented which demonstrate the principle benefits of the proposed model. One of these calculations involve an actual failure and the second is taken from an example in the current **PTC 19.3**. Both cases demonstrate how the proposed model can be used to identify high risk applications and potential failures in the design stage.

The various stress components are calculated by a combination of finite element and modal analysis techniques. The dimensions, service conditions and temperature are indicated in the respective figures. The maximum allowable static stress is taken from **B31.3** for the first example while **B31.1** is used for the **PTC** calculation. The fatigue allowables are assumed to be one half the static allowable stresses. For clarity, only the cyclical stresses are shown in the figures.

The first example, Fig(2), is in liquid sodium cooling loop at Monju Japan, where thermowell cracking was reported with loss of process containment and subsequent fire. Thermowell failure coincides with the oscillating drag condition with stress levels approaching the allowable stress of the material. The tip acceleration is ~150 g's at oscillating drag resonance. This compares with a tip acceleration ~260 g's derived from the reported displacement amplitudes in actual flow tests.

When the maximum allowable stress is de-rated to allow for the potential of liquid metal embrittlement, it is obvious that this thermowell is predisposed to failure. The authors recommended use of a tapered thermowell to correct the design. This modification results in an increased resonant frequency, a reduction in coherence of the vortex shedding process, and a drastic reduction in the root stresses.

The second example, Fig(3), is for a high pressure steam application considered in **PTC 19.3**. Even without oscillating drag, this design is predisposed to failure if used at the **PTC** rating of ~392 ft/s (120 m/s). To insure mechanical integrity, the maximum velocity should be limited to ~275 ft/s (85 m/s); however, even at this velocity the tip acceleration exceeds ~100 g's so an alternative design is required. When both thermowell and sensor accelerations are taken into

account, the **PTC** application is better served by a thermowell with a length restricted to 2" (50 mm).

Conclusions

Dynamic analysis methods are the most reliable method for predicting the application limits of thermowells. This is accomplished by combining a flexible beam model of the thermowell with a principle stress criteria for design and use of the allowable stresses established in the ASME Piping Codes (**B31**). The examples presented support the claim that high risk applications and potential failures are easily identified in design. It is clear that sensor acceleration limits must be included to insure measurement integrity and that both oscillating drag and oscillating lift need to be considered in the thermowell selection process.

Sub-critical operation of the thermowell is recommended in all high velocity streams, especially those upstream of rotating equipment, corrosive, or otherwise hazardous processes. Where a dynamic analysis is not performed and fluid velocity is high, i.e. >100 ft/s (30 m/s) for gas and steam and > 10 ft/s (3 m/s) for liquids, the thermowell length should be restricted to 2" (50 mm) and 4"(100 mm) respectively.

Figure Captions:

Figure 1: Cantilever coordinates for the continuous beam model.

Figure 2: An application where thermowell cracking resulted in a loss of containment and fire.

Figure 3: A thermowell design based on **PTC 19.3** which is predisposed to failure.

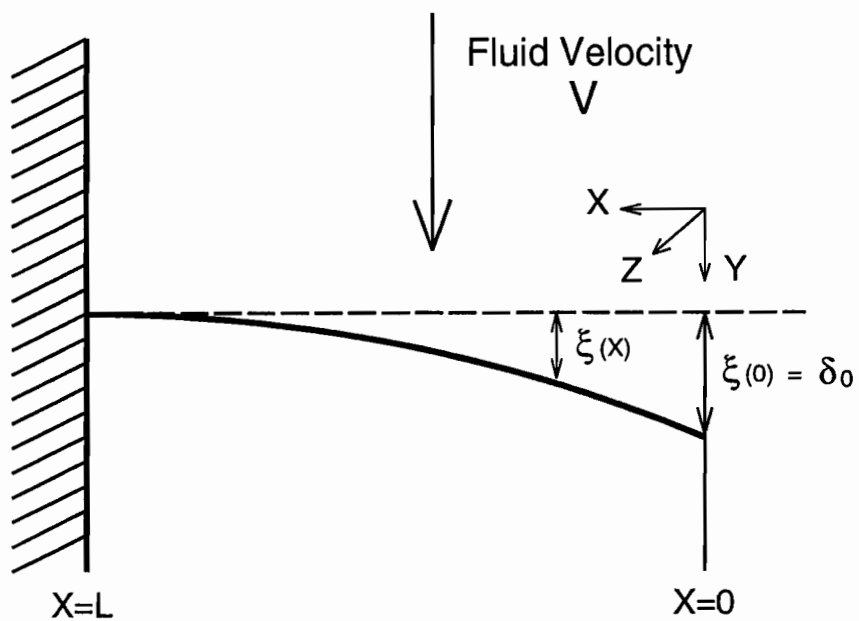


Figure 1

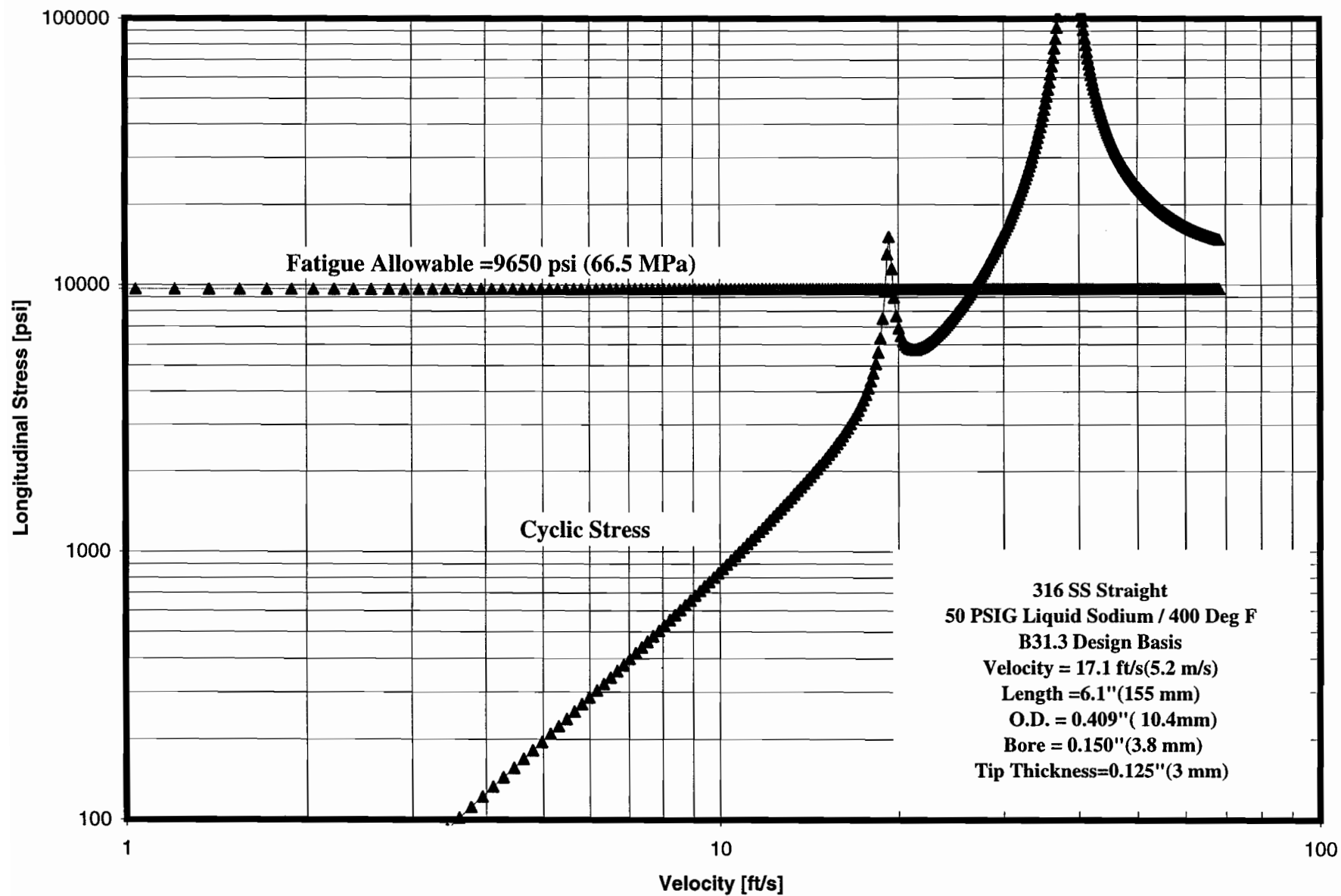


Figure 2

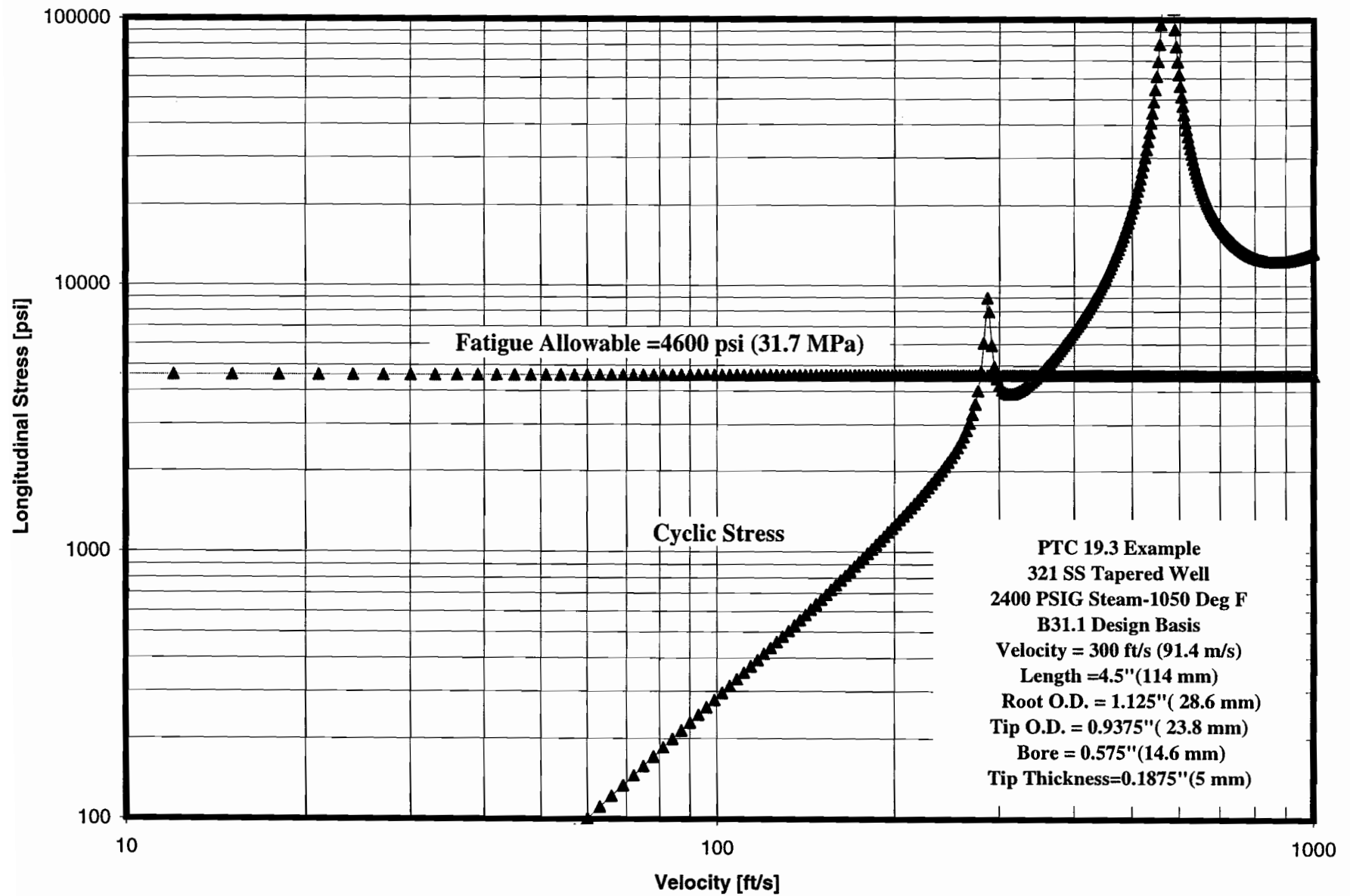


Figure 3



FATIGUE ANALYSIS OF THERMOWELL DUE TO FLOW-INDUCED VIBRATION

Masaki MORISHITA and Yusaku WADA

Power Reactor and Nuclear Fuel Development Corporation

Ibaraki, Japan

ABSTRACT

The incident of sodium leakage from a main pipe of the secondary heat transport system (SHTS) of Monju fast breeder reactor was caused by the failure of a thermocouple well. The thermowell was broken apart by high cycle fatigue failure. Flow-induced vibration (FIV) in the in-line direction associated with symmetric vortex shedding was the source of alternating stress causing this fatigue failure. Fractographic examinations revealed fracture patterns typical to high cycle fatigue.

The fatigue crack growth behavior was closely coupled with the FIV response through the variation of natural frequency of the thermowell. Fatigue damage and fracture mechanics analyses taking this coupling effect into account clarified the failure process from crack initiation, growth, and to final fracture. The close interaction between FIV response and crack growth was reproduced by FIV fatigue tests.

INTRODUCTION

Since the sodium was loaded in 1992, the secondary loop of the Monju fast breeder plant had been operated intermittently at 100% of its flow rate capacity, as part of the pre-operational and general plant performance test operations. The total time of 100% flow rate operations was about 700 hours. The initial criticality was achieved in April 1994 and the plant was first connected to the grid in August 1995. After that, electric power was gradually increased, on and off, as a series of power buildup test programs. In this period, the secondary loop was operated mainly at its 40% flow rate. The sodium leakage occurred during this 40% operation from a main pipe of the SHTS (Suzuki, et al., 1996).

The sodium leakage was caused by the breakage of a thermowell that was installed on the main pipe. It was confirmed by extensive analyses and experiments that the thermowell had been suffered from FIV, leading to high cycle fatigue failure. This FIV was not induced by the well known von Karman vortex shedding, but was an in-line

oscillation associated with symmetric vortex shedding (Yamaguchi et al., 1997, Ogura et al., 1998).

The in-line oscillation occurred while the loop was operated at its 100% flow rate, since the reduced velocity determined from the sodium flow velocity and the natural frequency of the thermowell was around two in this condition. On the contrary, the well did not break at a stretch during this period of 100% operation; rather, the final failure took place in the 40% flow rate operation where the reduced velocity was well below the range of in-line oscillation if the natural frequency of the thermowell remained unchanged.

With a purpose of estimating the fatigue failure process of the thermowell due to FIV, fracture mechanics analyses were made, along with the usual fatigue damage analysis. Here, an interaction between the variation of FIV response and crack growth behavior was taken into account through the change of the natural frequency of the well.

FRACTOGRAPHY

The thermowell made of 304 stainless steel was broken apart at the root of a steep diameter transition, as is shown in Fig. 1. A small piece that contained the fracture surface was brought in to the National Research Institute of Metals (NRIM), and subjected to a close fractographic examination by scanning electron microscopy (SEM). Figure 2 is a sketch of the examined fracture surface. Observed features of the fracture surface related to the crack behavior can be summarized as below.

- 1) The main crack initiated on the upstream side of the cross section, propagating towards the downstream direction. This is consistent with the bending stress distribution in the in-line oscillation.
- 2) Most of the fracture surface was occupied with mixed transgranular and intergranular failures. It is known that this type of failure surface is typically seen when crack growth rate is very low in high cycle fatigue.

- 3) Striations, where the crack growth rate was relatively high, were only observed near the dimple region that corresponding to the final ductile fracture.
- 4) Three typical crack front lines, denoted as *a*, *b*, and *c* in the sketch, were identified. On the lines *a* and *c*, the crack growth rate was estimated to be extremely low, or the crack almost arrested there. The crack growth rate was relatively high around the line *b* compared to the lines *a* and *c*. These estimations are based on the observed ratio of trans/inter-granular failure area: it is known that intergranular failure prevails when crack growth rate is extremely low.

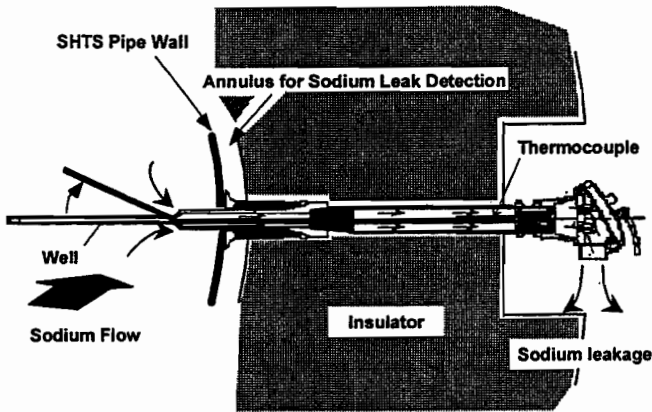


Fig. 1 Failed thermowell

FATIGUE DAMAGE ANALYSIS

As shown in Fig. 3, the secondary sodium loop had been operated on and off at 100% and 40% flow rates. Since the in-line oscillation due to FIV was first significant during the 100% flow rate operation, the fatigue damage analysis was made on this condition.

- : Crack initiation/coalescence
- : Low propagation rate
- : Striation
- : Dimple
- : Steps
- : Direction of Growth
- : Estimated Crack Front

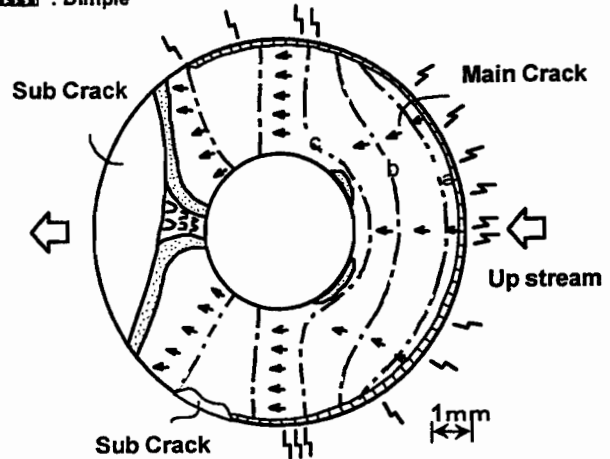
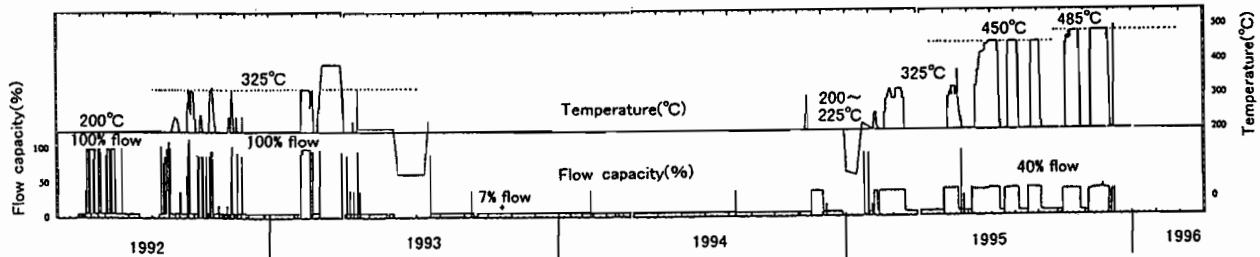


Fig. 2 Sketch of fractographic observation



Period	May, 1992 ↓ Aug, 1992	Sep, 1992 ↓ Jun, 1993		Jul, 1993 ↓ May, 1995		Jun, 1995 ↓ Nov, 1995		Dec, 1995 ↓
Operation time	About 200 hours	About 500 hours	About 0.5 hour	About 2000 hours	About 20 hours	About 2000 hours	About 1000 hours	About 1.5 hours
Operation condition	Temperature : 200℃	Temperature : 325℃	Temperature : 325℃	Temperature : 200℃	Temperature : 200~325℃	Temperature : 450℃	Temperature : 485℃	Temperature 450~485℃
	Flow rate : 100%	Flow rate : 100%	Flow rate : 100% ⇒ 40%	Flow rate : 40%, 7%	Flow rate : 100% ⇔ 40%	Flow rate : 40%	Flow rate : 40%	Flow rate : 40%

Fig. 3 History of SHTS operation

FIV Response

The FIV response of the thermowell was estimated in terms of displacement at the tip of the well. The dependence of the displacement amplitude on the reduced velocity was assumed to follow the response model shown in Fig. 4. This model was defined by simplifying the results of FIV water loop tests and the fluid-structure interaction analyses (Yamaguchi et al., 1997). In-line oscillation starts at $V_r=1.25$, takes its maximum value of $y/D=0.1$ at $V_r=2.1$, and ceases at $V_r=2.5$ again. The estimated responses are summarized in Table 1.

Table 1 Estimated in-line response

Temperature	°C	200	325
Duration	Hour	216	500
Flow Velocity	m/s	5.2	5.2
Natural Frequency	Hz	257	251
Reduced Velocity	---	2.02	2.07
Reduced Amplitude	---	0.091	0.097
Nominal Stress	MPa	100	101

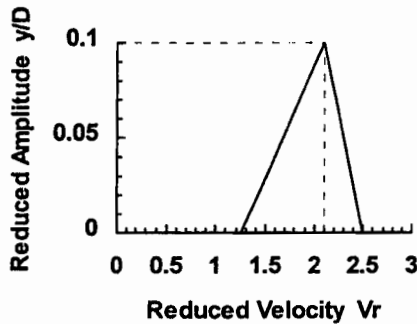


Fig. 4 In-line response model

Stress/strain Estimation

Nominal bending stress can be correlated with the displacement at the tip of the well through the simple beam theory and the vibration mode shape. In addition, there is a stress/strain concentration by the geometrical discontinuity at the root of the diameter transition. Theoretical stress/strain concentration factors were evaluated by 3D elastic and inelastic FE analyses with solid elements. Measured value of 0.1 mm for the radius of the root was used in the analyses, and the stress concentration factor, K_t , was calculated to be about 5.2. Based on an idea that the fatigue crack initiation is governed by grain slip in a local region, an inelastic strain concentration factor was also calculated to be about 3, using an average value of strain within one-grain size from the surface. Based on these calculations and some known relations between fatigue strength reduction factor and theoretical stress concentration factor, the strength reduction factor was estimated to be 3.

Fatigue Curve

The fatigue curves used in the analysis are shown in Fig. 5 for temperature 300° to 350°C. The average trend curve was originally proposed by Jaske (1977). It corresponds to the design fatigue curve B specified in an appendix to the Section III of the ASME Boiler and Pressure Vessel Code (Manjoine, 1983), but without safety factors of 20 on the number of cycles and 2 on the strain amplitude. The fatigue test data obtained on the thermowell material is overplotted, along with some existing data (Jaske, 1977). The expected upper and lower fatigue curves were determined by applying a factor of 1.2 to the average trend in the high cycle region.

Fatigue Life Estimation

A typical result of fatigue damage analysis is shown in Fig. 6. Here, the average trend of the fatigue curves was used. A very large value of accumulated fatigue damage was obtained, which implies that the fatigue crack(s) initiated at an early stage of the 100% flow rate operation. The region where the fatigue damage is greater than unity

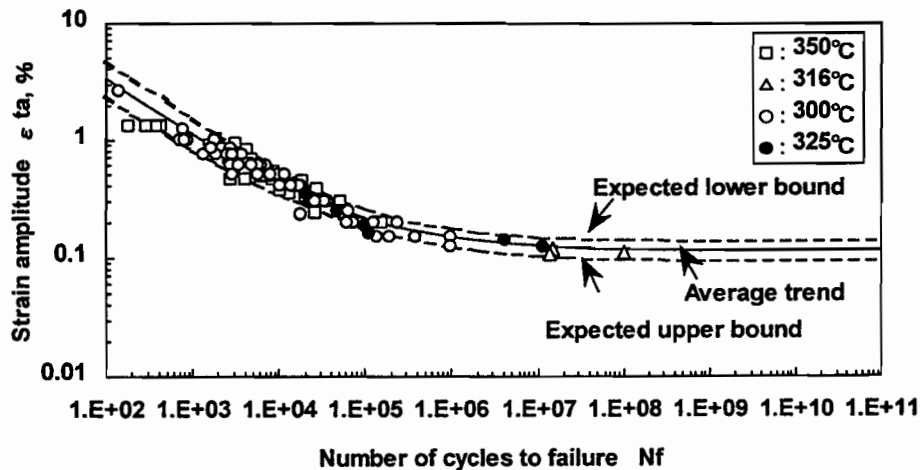


Fig. 5 Fatigue curve of austenitic stainless steels

spreads circumferentially over about ± 45 degrees. This is consistent with the fractographic examination shown in Fig. 2.

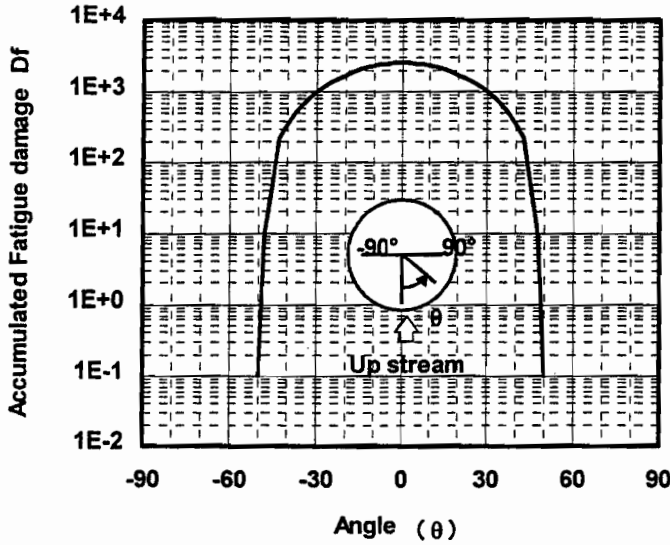


Fig. 6 Circumferential distribution of fatigue damage

CRACK GROW ANALYSIS

When the fatigue crack grew, it reduced the natural frequency of the thermowell. While the sodium flow rate remained constant, the in-line oscillation response was also affected since the reduced velocity varied. In this way, the in-line FIV response and the fatigue crack behavior was strongly coupled. Fracture mechanics analyses were made on the fatigue failure process taking this coupling into account (Wada et al., 1997).

Method of Analysis

The analysis procedure is given in Fig. 7. Relations between crack depth and natural frequency were derived, as shown in Fig. 8, from a series of dynamic analysis of cracked thermowell with a 3D solid FE model. Here, a straight crack front was assumed for simplicity. Presence of a sub-crack on the other side of the main crack was also considered. The same response model as in the fatigue damage analysis was used for the relation between the reduced velocity and the in-line response.

Crack growth rate was estimated by the linear fracture mechanics parameter, ΔK , with a relation

$$da/dN = C(\Delta K^m - \Delta K_{th}^m) \quad (1)$$

where a is crack depth, N is number of cycles, and C , m , and ΔK_{th} are material constants. The values of these constants for 200°C and 325°C are; $C=1.3 \times 10^{-11}$ m/cycle, $\Delta K_{th}=10.9$ MPa \cdot m $^{0.5}$, and $m=2.45$. The range of stress intensity factor was calculated by a simplified formula for a 2D crack on a cylinder.

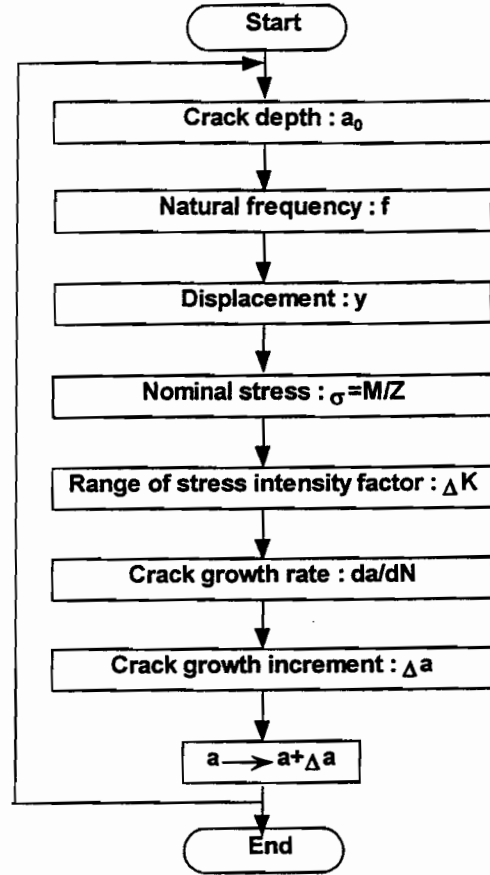


Fig. 7 Procedure of crack growth analysis

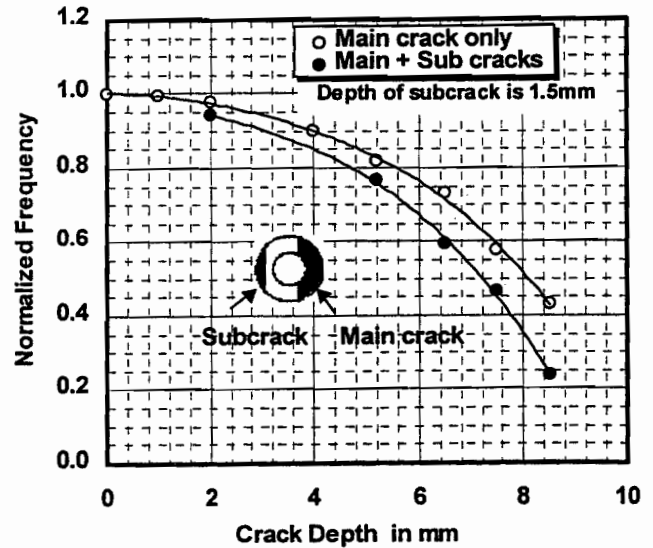


Fig. 8 Crack depth vs. natural frequency

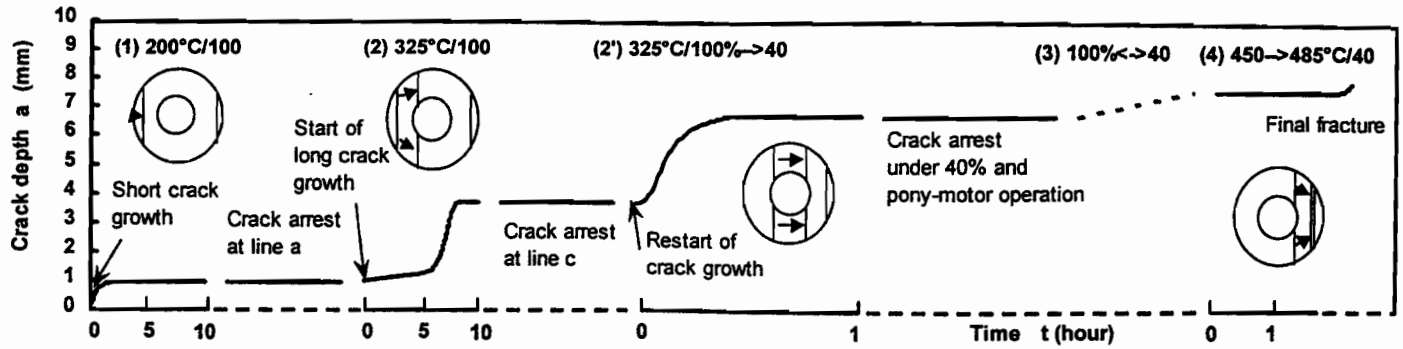


Fig. 9 Time history of crack growth and arrest

Results of Analysis

The process of crack growth obtained by the analysis is shown in Fig. 9. The following scenario for the failure process was found to be likely to have occurred.

- 1) The crack grew from its initiation under the 100%/200°C operation up to about 1 mm and arrested there by a sharp reduction of the stress concentration. The line *a* in Fig. 2 corresponds to this crack depth.
- 2) The crack started to grow again in the 100%/325°C operation because of a larger response in a higher temperature. As the crack grew, the crack growth rate attained its maximum value, the line *b* in Fig. 2.
- 3) As the crack grew farther and the natural frequency was lowered, the reduced velocity went out of the response range, suppressing the thermowell to oscillate and the crack to grow. The line *c* in Fig. 2 corresponds to this arrest.
- 4) The crack did not grow any more in the 100% flow rate operation. Instead, the reduced velocity for in-line response began to be satisfied during transient operations on the way to and from 100% flow rate. Then the crack grew again. A larger damping and thus a smaller response were likely in this stage. This larger damping might be attributed to some energy dissipation effects of crack opening/closure and plasticity in the ligament. Small response of a deeply cracked thermowell was observed in the FIV fatigue test, which will be discussed later.
- 5) When the crack depth reached a certain value, the reduced velocity for in-line response was finally achieved in the 40% flow rate. This in-line response caused the final crack growth and failure.

Verification by FIV Test

In order to verify the failure scenario described above, three FIV fatigue tests on mock-up thermowells using a water loop were carried out. Water temperature was chosen to be 57°C to reproduce the same Reynolds number as in the 200°C sodium flow. Two mock-ups were pre-cracked by mechanical vibration, while the other one was pre-cracked by FIV in the water loop. Acceleration response at the tip of the well and its frequency content were monitored during the tests. No sheath was used in the tests to obtain large response and for

instrumentation purpose.

Figure 10 is a typical test result in terms of the relation between the reduced velocity and the reduced displacement amplitude. Here,

- 1) The flow rate was increased up to 100% (5 m/s) and held constant until the measured frequency was reduced by 10%.
- 2) Under the constant flow rate of 100%, the in-line response of the well gradually decreased and calmed down along the path 2, since the natural frequency was decreased, leading to an increase in the reduced velocity.
- 3) Then the flow rate was varied between 100% and 40%. Although the amplitude was small, the in-line oscillation was resumed. The small amplitude might be attributed to an

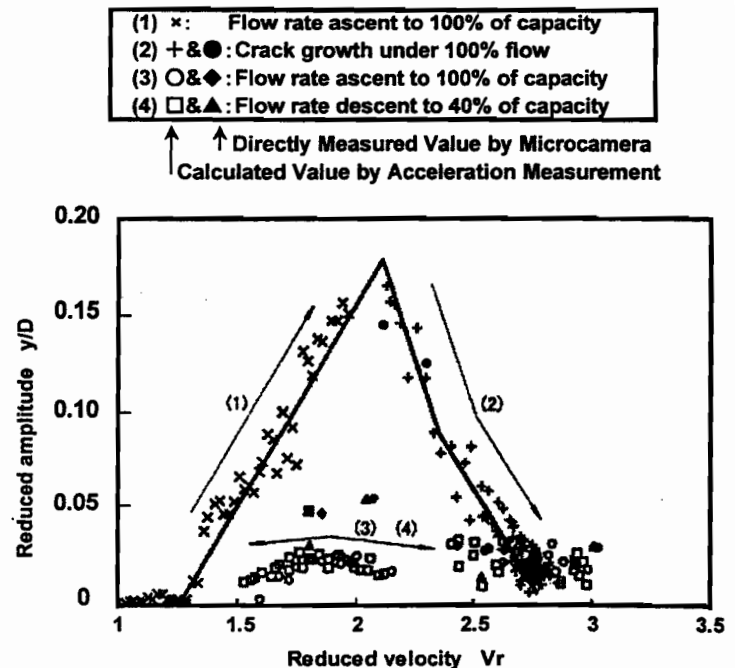


Fig. 10 Typical result of FIV fatigue test

additional damping that was brought about by energy dissipation with crack opening/closure and plasticity.

Fracture mechanics analyses were applied to these FIV fatigue tests. Figures 11 and 12 are the comparisons of the analysis and test results, in terms of the variation of displacement response and natural frequency along the elapsed time, respectively. In both of the figures, good agreements can be seen between the analysis and the tests, which indicates the applicability of the present analysis procedure.

CONCLUSIONS

From the fractographic examination and fatigue damage analysis, it was confirmed that the thermowell failure was caused by high cycle fatigue due to in-line FIV. The initiation of fatigue crack(s) was estimated to be at an early period of the 100% flow rate operations.

Fracture mechanics analyses were performed with the interaction between crack growth and FIV response through the change of natural frequency taken into account.

The analysis showed that;

1. The fatigue crack once arrested, since the response of in-line oscillation was ceased with lowered natural frequency of the thermowell.
2. After the crack reached a certain depth, the thermowell finally started to oscillate in the 40% flow rate condition, leading to the breakage.

Some FIV fatigue tests were made on mock-up thermowells, and they confirmed the failure process given by the analyses.

REFERENCES

- Jaske, C.E., and O'Donnel, W. J., 1977, "Fatigue Design Criteria for Pressure Vessel Alloys", Journal of Pressure Vessel Technology, ASME.
- Manjoine, M. J., and Tome, R. E., 1983, "Proposed Design Criteria for High Cycle Fatigue for Austenitic Stainless Steels", Proceedings, ASME Int. Conf. on Advances in Life Prediction Methods, ASME.
- Ogura, K., et al., 1998, "Cause of Flow-Induced Vibration of Thermocouple Well", Proceeding, ASME/JSME PVP Conference.
- Suzuki, T., et al., 1996, Monju Secondary Heat Transport System Sodium Leak", Proceedings, 10th Pacific Basin Nuclear Conference, Kobe, Japan
- Wada, et al., 1997 "Failure Mechanism of a Thermocouple Well Caused by Flow-induced Vibration: Part 2 -Interaction between Flow-induced Vibration and Crack Growth in a Thermocouple Well", Proceedings, 4th International Symposium on Fluid-structure Interactions, Aeroelasticity, Flow-induced Vibration and Noise, Vol. 1, pp149-148, ASME
- Yamaguchi, A., et al., 1997, "Failure Mechanism of a Thermocouple Well Caused by Flow-induced Vibration: Part 1 - Numerical Simulation and Water Experiment of Flow-induced Vibration", Proceedings, 4th International Symposium on Fluid-structure Interactions, Aeroelasticity, Flow-induced Vibration and Noise, Vol. 1, pp139-148, ASME

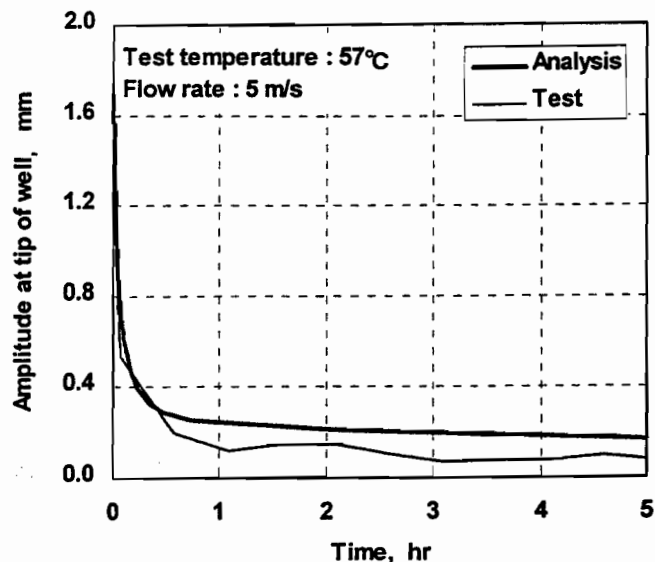


Fig. 11 Comparison of FIV response variation between test and analysis

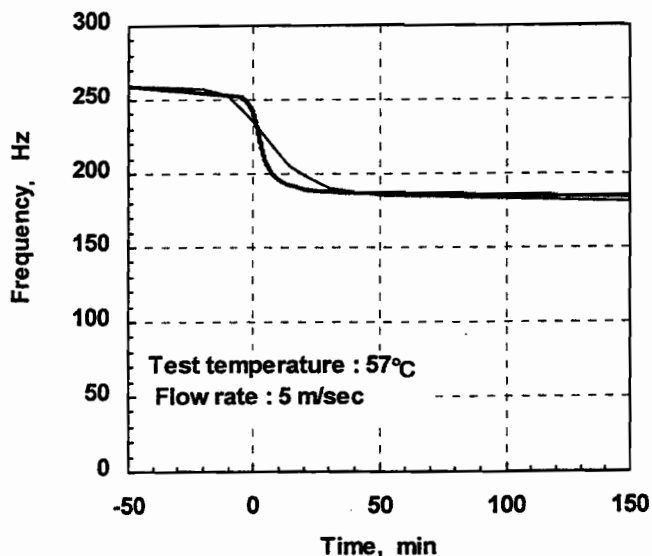


Fig. 12 Comparison of frequency change between test and analysis



ASME International

The American Society of Mechanical Engineers
Three Park Avenue
New York, NY 10016-5990

Reprinted From
**PVP-Vol. 363, Flow-Induced Vibration and Transient
Thermal-Hydraulics**
**Editors: M. K. Au-Yang, T. Nakamura, F. Hara,
A. Okajima, and Y. W. Shin**
Book No. H01144 - 1998

MODIFICATION AND DESIGN GUIDE OF THERMOWELL FOR FBR

Koji DOZAKI

Plant Improvement Planning Group,
Monju Construction Office,
Power Reactor and Nuclear Fuel Development
Corporation, Shiraki, Tsuruga, 919-1279, Japan

Masaki MORISHITA

Structure and Material Research Section,
O-arai Engineering Center
Power Reactor and Nuclear Fuel Development
Corporation, O-arai, Ibaraki, 311-1393, Japan

Koji IWATA

Advanced Technology Division, O-arai Engineering Center
Power Reactor and Nuclear Fuel Development Corporation, O-arai, Ibaraki, 311-1393, Japan

ABSTRACT

A thermowell at the intermediate heat exchanger outlet of Monju secondary cooling system was broken due to high cycle fatigue which was caused by Flow Induced Vibration (FIV).

Since the other existing thermowells on the secondary cooling system pipings in Monju have the same shape and size, it has been planned that most of those thermowells are to be replaced by modified ones and the rest to be removed.

The length of the immersed section of the modified thermowells was chosen in order that both the requirement for the temperature sensing and the structural integrity evaluation criteria against FIV were satisfied.

As the requirement for temperature sensing and flow velocity of sodium are not uniform for all thermowells, three different modified designs were prepared for the three groups of condition. These design concepts are presented in this paper.

A newly prepared design guide for thermowells against FIV provided the evaluation criteria to prove the structural integrity of the modified design. Although this design guide basically follows ASME Boiler and Pressure Vessel Code Section III Appendix N-1300, some additional evaluation methods are introduced, for example, definition of parameters used in the lock-in synchronization avoidance criteria of the design guide is extended to be applicable to a taper-shaped thermowell. Contents of the design guide are also presented.

1. INTRODUCTION

From the investigation of the existing thermowell's design on the secondary cooling system pipings in Monju, problems on the shape and structural strength of the thermowell resulting from the

initial design approach were identified as follows;

- In order to improve the thermal response characteristics, the following points had been thought a great deal of importance,
 - To make the thickness of the immersed section of thermowell uniformly thin.
 - To measure the temperature of sodium in the piping as close to the center as possible.
- On the other hand, the corner radius at the narrowing point of the well was not specified.

As for the structural design for FIV, only prevention of Kármán vortex resonance in lift direction was considered but in-line vibrations were not considered. Although N-1300 was added to ASME Sec. III Appendix N after the design of the existing thermowells, re-evaluation with ASME N-1300 would have found the problem of the wells on the in-line vibration. The root cause of these problems was a lack of recognition of the importance of non-class components, such as the thermowells, on the coolant boundaries.

As an improvement to prevent sodium leak due to FIV, PNC newly prepared a design guide for thermowells against FIV and design modification study of thermowell were made, reflecting the problems on the existing thermowells as mentioned above.

2. DESIGN MODIFICATION STUDY OF THERMOWELLS

2.1 Basic Approach for Modified Design

The basic approach for modified design is illustrated in Fig 1. Failure of the broken thermowell occurred at the narrowing point of the stepped cylindrical well. Sodium invaded from the failure point into the cylinder and spread out of the thermometer through the terminal head.

Causes of the failure were the following two points,

- Only prevention of Kármán vortex resonance in lift direction was considered but in-line vibrations were not considered.
- Stress concentration due to a step on the cylinder.

Cause of sodium spreading out of the thermometer was,

- There was no suppression mechanism inside the well for sodium leakage.

It is considered, therefore, improvement should be focused on prevention of failure and suppression at sodium leakage. Detection of the well failure should be also taken into account.

Target of improvement is aimed at prevention of failure as follows,

- Well balanced design for both measurement and strength.
- Reduce the number of penetration through sodium boundary.

For suppression with detection, target is aimed at as follows,

- Installation of suppression mechanism for sodium leakage due to supposed well failure.
- Installation of leak detection system in case of supposed well failure.

Removal of superfluous thermowells may be taken into account from the view of the reduction of the number of penetration through the coolant boundaries. Moreover, simplification of sodium containing walls may lead to an development of a new temperature sensor without penetration.

2.2 Specifications of Existing Thermometers

Location and number of the existing thermometers on the secondary cooling system in Monju are illustrated in Fig. 2. Signals from the three thermometers per loop (totally nine thermometers) at the outlet of evaporator are used as safety protection system against the loss of heat removal by the water/steam system.

These nine thermometers for safety protection and twenty-four for plant interlock have specifications on response time constant.

Signals of the other two thermometers per loop at the outlet of evaporator (totally six), one per loop at the outlet of intermediate heat exchanger (totally three), one per loop at the inlet of superheater (totally three), two per loop at the outlet of superheater (totally six) and two per loop at the outlet of air cooler in auxiliary cooling system (totally six), that is, twenty-four thermometers as a grand total, are used as plant interlocks. Among these twenty-four thermometers for plant interlock, six at the outlet of superheater and six at the outlet of air cooler in auxiliary cooling system (totally twelve) have specifications on response time constant.

Signals of the other fifteen thermometers on the secondary cooling system in Monju are used for either plant control, annunciation, post-accident monitoring, record chart, inspection monitoring or computer input, and do not have any specifications on response time constant.

2.3 Specifications of Modified Thermometers

Specifications of modified thermometers are based on the following policies,

- The function criteria for the thermometers in safety design (safety protection system) and on plant design (plant dynamics analysis) should be retained.
- The number of thermowells shall be based on Monju performance specifications including redundancy.

From these policies, each two thermometers per loop at the inlet and outlet of air cooler in auxiliary cooling system (totally six), whose signals are used for computer input, can be removed by substituting the function of computer inputs with the other thermometer signals at the inlet and outlet of the air cooler in auxiliary cooling system.

Discussions on the important parameters in design, response requirements for the thermometers and the length of the immersed section of thermowell are made in the following sections.

2.3.1 Response requirement for thermometers.

Safety protection system design did not require any absolute response time constant of thermowell. Descriptions are found, however, on the response time constant given by the Monju plant design in the licensing document of Monju safety design. Modified designs are to follow, therefore, the upper estimation of the response time constant for the evaporator outlet temperature measurement, 20 seconds, in the existing Monju safety design. The same response time constant was used in the plant dynamics analysis.

Since the response time constant of a thermometer is defined as the first order delay time in the step response property of the thermometer, response time constant itself is independent on the length of the immersed section of the thermowell. Nevertheless, response requirement in safety analysis or plant dynamics analysis is considered to be based on an assumption that the thermometer should measure the representative temperature in the piping section. This viewpoint leads to a requirement for the length of the immersed section of thermowell which has the response requirement in safety analysis or plant dynamics analysis.

2.3.2 The length of the immersed section of thermowells.

The length of the immersed section of thermowell should be chosen, as mentioned in the previous section, long enough to enable the thermometer to measure the representative temperature in the piping section. The bulk average temperature, T_b , which is defined by equation (1) is considered to be the representative temperature here.

$$T_b = \frac{\iint u\gamma C_p T ds}{\iint u\gamma C_p ds} \quad (1)$$

where, u : velocity, γ : specific weight, C_p : specific heat, T : temperature, ds : represents area integral

On the other hand, the length of the immersed section of the modified well should be chosen shorter than that of the existing wells so that the natural frequency of the well becomes higher in order to lower the reduced velocity, a major parameter to judge the structural integrity against FIV with enough margin.

The depth to measure the representative temperature varies, however, with the temperature distribution in the piping section which depends on the location of the thermometer. Natural frequency of the well varies with the diameter and thickness of the well which may depend on the joint form of the well to the piping. Reduced velocity depends, of course, on the sodium velocity inside the piping.

There are two groups of sodium velocity in Monju secondary cooling system, one is main cooling system, and auxiliary cooling system is another. The former reaches around 5.5m/sec at the condition of 100% thermal power in hot leg pipings, the latter remains around 0.7m/sec at the condition of residual heat removal operation.

Response-required thermometers in main secondary cooling system are those at the evaporator outlet (nine) and at the superheater outlet (six). The length of the immersed section of these thermowells is designed as 110 mm from the inner surface to the tip of the well. 10 mm of 110 mm is for the length from the temperature sensing point to the well tip. The rest 100 mm is for the net length of the immersed section. This length is obtained from a result of numerical thermalhydraulic analyses using a model of evaporator outlet plenum and crossover-leg piping which is connected with the plenum. Static and transient conditions are considered in those analyses. The evaporator outlet model is selected as first importance, since the thermometers whose signals are used for a safety protection system are at the outlet of evaporator. Although the length 100 mm is close to the minimum value to measure the bulk average temperature, T_b , from the analytical result, this length is adopted as it is according to the policy to have as enough margin for FIV evaluation as possible.

Response-required thermometers in the auxiliary cooling system are those at the outlet of the air cooler (six). The length of the immersed section of these thermowells is to be designed to follow the result of the other response-required thermometers in main secondary cooling system as mentioned above. 110 mm from the inner surface of the pipe to the tip of the well is also adopted, therefore, as the length of the immersed section of these thermowells at the outlet of air cooler in auxiliary cooling system.

The length of the immersed section of the other thermowells, which don't have any requirements for the response, is to be designed from the view of the measurability of sodium temperature without the influence of the heat transfer from the piping to the atmosphere. There is an empirical rule of the immersed length of thermowell for steady state of sodium flow, which provides the length as several times of the diameter of the thermocouple. The length obtained from the empirical rule is rather short, thus it is easy to achieve the design which has longer immersed length than that required. In transient conditions, temperature distribution over

the section of a piping changes as shown in Fig. 3. This result was obtained from a transient thermalhydraulic analysis of a straight pipe model under the condition of a step change of temperature at 1.5m upstream from the temperature measuring location. It is made clear from this analytical result, that the length of the immersed section is preferably longer than 20% of radius of the piping in order for the measured temperature to reach the representative temperature over the section. The length of the immersed section of the thermowells which don't have any requirements for the response, is designed as 50 mm from the inner surface of the pipe to the sensing point of the well. The length from the inner surface to the tip of the well is designed 60 mm considering additional 10 mm from the sensing point to the tip.

2.4 Concepts of Modified Thermometers

2.4.1 Well Shape and Thickness.

For all modified designs of thermowell on the secondary cooling system piping in Monju, well shape is designed as a taper-shaped cylinder without step. This choice is based on the intention to eliminate or minimize stress concentration to provide a well balanced design for both measurement and strength.

Thickness of each well is designed as 3 mm around the temperature sensing point and gradually becomes thicker as closer to the joint to the piping. The design of this well shape and thickness is quite different from the previous design for the existing wells where the uniform thickness 3 mm was thought as the first priority for temperature sensing. Prospect of good response performance was obtained based on thermal response tests using taper-shaped wells in hot water for the modified design study. It is not necessary, therefore, to design the immersed section of well uniformly thin.

2.4.2 The length of the wells and joint form to the pipings.

Based on the design specification on the length of the immersed section of the well mentioned in the section 2.3.1, the length of the well and the structure of joint form of the well to the piping are chosen, considering the other different design factors from the temperature sensing, for example, strength against FIV, convenience for fabrication as follows,

(1) Response-required thermowells on secondary main cooling system

The length of the immersed section is designed 110 mm from the inner surface of the piping to the tip of the well as is required by the specification which is close to the minimum requirement from the view of temperature sensing.

Not the existing nozzle joint but a built-in joint concept is chosen for the joint form of the thermowell to the piping which enables to design the outer diameter of the well root larger than that when the existing nozzle joint is applied. This built-in joint design provides an advantage that the natural frequency for the funda-

mental vibration mode of the well portion inside the piping raises up to lower the reduced velocity to less than 1 with enough margin for the fundamental vibration mode. If the reduced velocity, which is a parameter to evaluate the possibility of synchronized vibration, is under 1, then the vortex-induced vibration can be avoided.

Two thermowells per loop (totally six) at the outlet of evaporator don't have any response requirements but are designed as the same as the response-required thermowells mentioned above. The reason is that these thermowells are located close to another three thermowells per loop (totally nine) which have the response requirements and it will be easy if modification is performed by a pipe unit with the whole five thermowells per loop.

(2) The other thermowells on secondary main cooling system

The length of the immersed section is designed 60 mm from the inner surface of the piping to the tip of the well. Since the immersed length is much shorter than that of the response-required thermowells, the existing nozzle form can be applied to the joint of the well to the piping, keeping the natural frequency for the fundamental vibration mode of the well portion inside the piping high enough to make the reduced velocity for this vibration mode lower than 1. The length from the root of the nozzle joint to the tip of the well becomes around 120 mm, considering the existing nozzle height 60 mm.

(3) Thermowells on the auxiliary cooling system

The length of the immersed section is designed 110 mm from the inner surface of the piping to the tip of the well which is based on the specification for the response-required thermowells on the auxiliary cooling system. Since the sodium velocity of the auxiliary cooling system is much lower than that of the main secondary cooling system, the existing nozzle form can be applied to the joint of the well to the piping, keeping the natural frequency for the fundamental vibration mode of the well portion inside the piping high enough to make the reduced velocity for this vibration mode lower than 1. Although it is not necessary to make the length so long as 110 mm for the other thermowells on the auxiliary cooling system, all thermowells on the auxiliary cooling system is designed to have uniform shape and dimensions to avoid complication.

The design concepts for these thermowells on secondary main cooling system mentioned above (1) to (3) are shown in Fig. 4. Specifications of these thermometers are shown in Table 1.

2.4.3 Suppression and detection of sodium leak in case of well failure.

Suppression mechanisms against the sodium leak due to supposed well failure and detection systems of leaking sodium were investigated for the modified design. There would be two sodium leak paths out of the thermometer into the piping rooms in case of supposed well failure. One is a path through the connecting part of the measuring device with the well. A metal gasket with a nut is chosen as a suppression mechanism for this first leak path as shown in Fig. 4.

Another possible leak path would be inside the measuring device. Sodium leak through this second leak path can be intercepted by means of an application of a seal weld between the thermocouple sheath and the end plate of cylinder in the measuring device.

A contact type leak detector (CLD) is chosen as the leak detection device as shown in Fig. 4.

2.4.4 Structural Integrity of Modified Thermowells.

Structural integrity of the modified concepts of thermowells against FIV was evaluated according to the design guide for thermowells against FIV which is described in the next section. As the result of the evaluation, it was confirmed that all proposed designs meet the criteria for avoidance of synchronized vibration at their respective locations and flow conditions. Reduced velocity, V_r for second vibration mode, which is the fundamental vibration mode for the immersed section of the well, was lower than 1 for every type of design. Vibration stress levels were also evaluated and even the maximum stress amplitude at base of thermowell among three types of design was lower than quarter of allowable fatigue limits for design at its respective temperature condition.

3. DESIGN GUIDE FOR THERMOWELLS AGAINST FIV⁽¹⁾

3.1 Design Evaluation Procedure

The design guide will provide the design evaluation procedure of thermowells against FIV shown in Fig. 5. As the first judgment of the design procedure, synchronized vibration is to be avoided or suppressed by satisfying the synchronization region avoidance criteria. Moreover, the second judgment is to be executed on high cycle fatigue due to stress amplitude caused by FIV.

3.2 Avoidance or Suppression of Synchronized Vibration

The synchronization region avoidance criteria in the design guide are described as follows,

If either of the following three conditions is satisfied, then synchronized vibration can be avoided or suppressed.

- (a) $V_r < 1$
- (b) $C_n > 64$
- (c) $V_r < 3.3$ and $C_n > 1.2$

where reduced velocity, V_r and reduced damping, C_n are defined as follows,

$$V_r = \frac{V}{f_n D_o} \quad (2)$$

V : Average flow velocity around well

D_o : Minimum outside diameter of well

f_n : Natural frequency of n th vibration mode of well

$$C_n = \frac{4\pi\xi_n M_n}{\rho \int_0^{L_n} D^2(x) \phi_n^2(x) dx} \quad (3)$$

ρ : Fluid mass density

$D(x)$: Outside diameter (variable in axial direction x)

ξ_n : Fraction of critical damping for n th mode

M_n : Effective modal mass for n th vibration mode

$$(\int_0^{L_n} m_i(x) \phi_n^2(x) dx)$$

$\phi_n(x)$: n th vibration mode

$m_i(x)$: Effective mass per unit length

$$= m_s(x) + m_c(x) + m_A(x)$$

$m_s(x)$: Well mass

$m_c(x)$: Contained fluid mass

$m_A(x)$: Displaced fluid mass

L_n : Well length subject to vortex shedding

L : Total length of well assembly

Two non-dimensional parameters, reduced velocity, V_r and reduced damping, C_n , are to be calculated for each vibration mode of a thermowell in design before judging. The synchronization region avoidance criteria is illustrated in Fig. 6. Although the criteria basically follows the same criteria in ASME N-1300 which is applicable to uniform cylinders⁽²⁾, definitions of V_r and C_n in the design guide here are extended to general forms applicable to cylindrical thermowells with non-uniform diameter along the longitudinal axis of the cylinder, for example, taper-shaped thermowells. Also, for relatively thin walled sodium piping systems where the pipe wall is not a rigid structural boundary it is necessary to consider the mass distribution mode shape and frequency of the entire well assembly including its interaction with the pipe wall when evaluating the effective modal mass, M_n .

Another difference between the design guide and ASME N-1300 is that the former requires the synchronization region avoidance judgment for all considerable vibration mode while the latter for a fundamental vibration mode⁽²⁾.

The synchronization region avoidance criteria is based on the same background data as those of ASME N-1300⁽³⁾⁽⁴⁾⁽⁵⁾.

3.3 High Cycle Fatigue Evaluation

In addition to the synchronization region avoidance criteria, stress amplitude in the well due to FIV is to be calculated and limited within allowable stress limit to prevent high cycle fatigue failure.

The stress amplitude is limited as follows,

$$K \sigma_v(x) \leq \sigma_f \quad (4)$$

K : Fatigue strength reduction factor

(Stress concentration factor)

$\sigma_v(x)$: Flow-induced nominal stress amplitude in well

σ_f : Allowable fatigue limit for design

$\sigma_v(x)$ can be calculated by the following equation,

$$\sigma_v(x) = \sqrt{\sum_n \{\sigma_{L,n}^2(x) + \sigma_{D,n}^2(x) + \sigma_{R,n}^2(x)\}} \quad (5)$$

$\sigma_{L,n}(x)$: Nominal stress amplitude in lift direction for n th mode displacement amplitude by vortex shedding

$\sigma_{D,n}(x)$: Nominal stress amplitude in drag direction for n th mode displacement amplitude by vortex shedding

$\sigma_{R,n}(x)$: Nominal stress amplitude for n th mode displacement amplitude by turbulent buffeting

3.3.1 Displacement amplitude by vortex shedding.

Vortex-induced vibration can be considered as forced vibration when lock-in is avoided or suppressed. n th mode displacement amplitude in lift direction by vortex shedding, $y_{L,n}(x)$, can be calculated from the response of a single-degree-of-freedom system subjected to harmonic forces, assuming a uniform distribution of fluid force $\frac{1}{2} \rho V^2 \alpha_L D$ per unit length of well.

$$y_{L,n}(x) = \frac{\rho V^2 \alpha_L \int_0^{L_n} D(x) \phi_n(x) dx}{2(2\pi f_n)^2 \int_0^{L_n} m_i(x) \phi_n^2(x) dx} A_L \phi_n(x) \quad (6)$$

$$A_L = \frac{1}{\sqrt{\left\{1 - \left(\frac{f}{f_n}\right)^2\right\}^2 + \left\{2(\xi_n + \zeta_n) \frac{f}{f_n}\right\}^2}} \quad (7)$$

A_L , α_L and f_n are amplification factor in lift direction, coefficient for lift force and frequency of periodic vortex shedding, respectively. ζ_n is fluid damping for n th vibration mode and can be calculated by the following equation,

$$\zeta_n = \frac{1}{4} \left(\rho D_m^2 \int_0^{L_n} \phi_n^2(x) dx \right) \left(\frac{V}{2\pi f_n D_m} \right) \quad (8)$$

D_m : Average outside diameter of well in fluid

Other symbols are defined in Section 3.2.

Equation for $y_{D,n}(x)$, displacement amplitude in drag direction by vortex shedding, can be obtained in the same way, replacing the subscript L in equation (6) with D . Note f_n in equation (7) is replaced with $2f_n$ for drag direction equation (10).

$$y_{D,n}(x) = \frac{\rho V^2 \alpha_D \int_0^{L_n} D(x) \phi_n(x) dx}{2(2\pi f_n)^2 \int_0^{L_n} m_i(x) \phi_n^2(x) dx} A_D \phi_n(x) \quad (9)$$

$$A_D = \frac{1}{\sqrt{\left\{1 - \left(\frac{2f}{f_n}\right)^2\right\}^2 + \left\{2(\xi_n + \zeta_n) \frac{2f}{f_n}\right\}^2}} \quad (10)$$

A_D , α_D and f_n are amplification factor in drag direction, coefficient for drag force and frequency of periodic vortex shedding, respectively.

Constant values are assigned for coefficient for lift force, α_L and that for drag force, α_D conservatively considering that the vibration amplitudes calculated by the equations of $y_{L,n}(x)$ and $y_{D,n}(x)$ are to be consistent with experimental data⁽³⁾⁽⁵⁾ at the boundary of lock-in region as follows,

$$\alpha_L = 0.4$$

$$\alpha_D = 0.04$$

3.3.2 Displacement amplitude by turbulent buffeting.

Vibration induced by turbulence can be described by random vibration theory. Displacement amplitude of well is to be calculated by the following equation,

$$y_{r,n}(x) = C_0 \sqrt{\frac{L_s G_f(f_n) J^2 \int_0^L \phi_n^2(x) dx}{64 \pi^3 M_n^2 f_n^3 (\xi_n + \zeta_n)}} \phi_n(x) \quad (11)$$

$G_f(f)$ is single-sided power spectral density generated by the turbulent pressure field, C_0 is peak factor(=3), $J^2 (= 3D_m/L_s)$ is joint acceptance where D_m is average outside diameter of well fluid. Although equation (11) has the identical form with the turbulence-induced vibration formula in ASME N-1300⁽²⁾, displacement amplitude at the peak of random excitation is estimated by considering the peak factor instead of root mean square value. Another difference from ASME N-1300⁽²⁾ is the additional consideration of fluid damping ζ_n to structural damping ξ_n .

Not many data on power spectral density of fluid force to which an immersed cylinder inside piping, $G_f(f)$, is subjected are reported. In the design guide, the following function is presented as an upper bound of the data on power spectral density of lift force obtained by the tests in water piping,

$$G_f(f) = \Phi(f) \left(\frac{1}{2} \rho V^2 D_m \right)^2 (D_m / V) \quad (12)$$

$$\text{where, } \Phi(f) = \frac{4 C_n^2}{1 + \left(\frac{2\pi f D_m}{V} \right)^2} \quad (13)$$

C_n : Coefficient for fluid force by turbulence

Fig. 7 shows these data⁽⁶⁾ (Mulcahy, 1984) and normalized power spectral density, $\Phi(f)$, presented in the design guide. Note the peak of the spectral density which exists around $fD/V = 0.2$ on the horizontal axis is considered to be generated by vortex shedding.

Maximum Reynolds number (Re) is 1.6×10^5 in the water tests by Mulcahy. Re may raise to more than this, however, in operation conditions of practical plants. Applicability of presented power spectral density equation for larger Re region is confirmed by comparing with experimental data obtained by the tests in air with the larger Re conditions⁽⁷⁾ (Fung, 1960).

Coefficient for fluid force by turbulence, C_n , is to be constant 0.2 based on an assumption of isotropy and experimental data analyzed by Mulcahy from tests in water and in air. Fig. 8 shows the experimental values of coefficient for turbulent lift force, C_{ln} , coefficient for fluctuating drag force, C_{dn} , and presented constant 0.2 in the design guide. C_{dn} data shown in Fig. 8 can be considered to be almost equal to turbulent component. Presented constant 0.2 as C_n in the design guide seems to be conservative in comparison with the data as shown in Fig. 8.

4. SUMMARY

Modified designs of thermowells have been presented for those on the secondary cooling system piping in FBR Monju. The modified designs are based on a newly prepared design guide to prevent failure due to FIV.

The design guide provides high cycle fatigue evaluation for stresses due to vortex-induced vibration and also random turbulent vibration in addition to synchronization region avoidance criteria due to vortex shedding.

As a result of the design study, each immersed length of three different thermowells was selected much shorter than that of the existing thermowells to satisfy the criteria in the design guide with enough margin, also satisfying the requirement for temperature measurement. Tapered shape is adopted for each modified wells for advantage in structural design against FIV.

ACKNOWLEDGMENTS

Modification design study described in this paper was performed as one of the Monju Plant Improvement Projects by the staff of the Plant Improvement Planning Group in Monju Construction Office, PNC. Since the modified design of thermowells are conceptual ones, some minor changes may be introduced in the stage of final design for fabrication.

We would like to appreciate PNC International Fellows, Mr. R. L. Jetter and Mr. Kwok Wong, Technology Development Division in Monju Construction Office, made a great effort on the FIV evaluations of the proposed designs.

The authors would also like to acknowledge that the preparation of the design guide was performed by great contribution of the participants of Special Working Group on Thermometer Design Guide.

REFERENCES

- (1) Special Working Group on Thermometer Design Guide, 1997, "Proposed Flow-Induced Vibration Design Guide for Thermometer Wells," PNC TN9410 97-042
- (2) ASME, 1995, ASME Boiler and Pressure Vessel Code Section III, Division 1, Appendix N, Article N-1300
- (3) Scruton, C., 1963, "On the wind excited oscillations of stacks, towers, and masts, Proc. Conf. on Wind Effects on Buildings and Structures," Paper 16, Teddington, pp798-833.
- (4) King, R., Prosser, M.J., Johns, D.J., 1973, "On vortex excitation of model piles in water," J. of Sound Vibration, 29[2], pp169-188.
- (5) King, R., 1975, "An investigation of the criteria controlling sustained self-excited oscillation of cylinders in flowing water," 4th Biennial Symp. in Turbulence in Liquids, Univ. of Missouri-Rolla, USA., pp.171-191
- (6) Mulcahy, T.M., 1984, "Fluid forces on a rigid cylinder in turbulent crossflow," Proc. Symp. on Flow-induced Vibrations, Vol.1, Excitation and Vibration of bluff bodies in cross flow, (eds. M.P. Paidoussis, et al.), ASME, pp15-28.
- (7) Fung, Y.C., 1960, "Fluctuating lift and drag acting on a cylinder in a flow at super critical Reynolds numbers," J. of Aerospace Sci., 27[11], pp801-814.

Table 1 Specifications of Modified Thermometers

Location of thermometers*	No. of thermometers*2	Use of Thermometers		Response Time Constants		Specifications of Wells		Suppression Mechanism and Detection System
		OP or MT*3	Plant Tests	OP or MT*3	Plant Tests	Immersed Lengths*4	Joint Form to pipings	
Main Secondary Cooling System	IHX Outlet	1	○	○	(18sec)	50mm	Existing Nozzle	○
	SH Inlet	1	○	○	(18sec)	50mm	Existing Nozzle	○
	SH Outlet	2	○	○	18sec	100mm	Bilt-in-Joint	○
	EV Outlet	3	○	○	18sec	100mm	Bilt-in-Joint	○
	EV Outlet	2	○			100mm		○
	IHX Inlet	1	○	○	(18sec)	50mm	Existing Nozzle	○
Auxiliary Cooling System	A/C Inlet	2	○	○	(18sec)	100mm	Existing Nozzle	○
	A/C Inlet	Remove						
	A/C Outlet	2	○	○	18sec	100mm	Existing Nozzle	○
	A/C Outlet	Remove						

* IHX: Intermediate Heat Exchanger, EV: Evaporator, SH: Superheater, A/C: Air Cooler

*2 Number of thermometers per loop. Total numbers are 3 times these numbers.

*3 Operation or Monitoring

*4 Length from the inner surface of piping to temperature sensing point

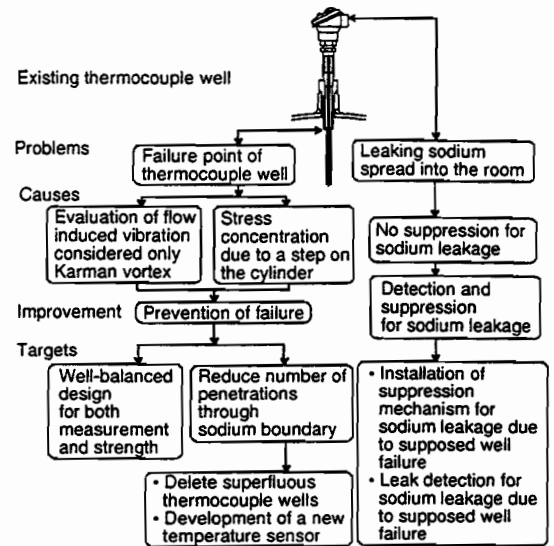


Fig. 1 Basic Approach for Modified Design

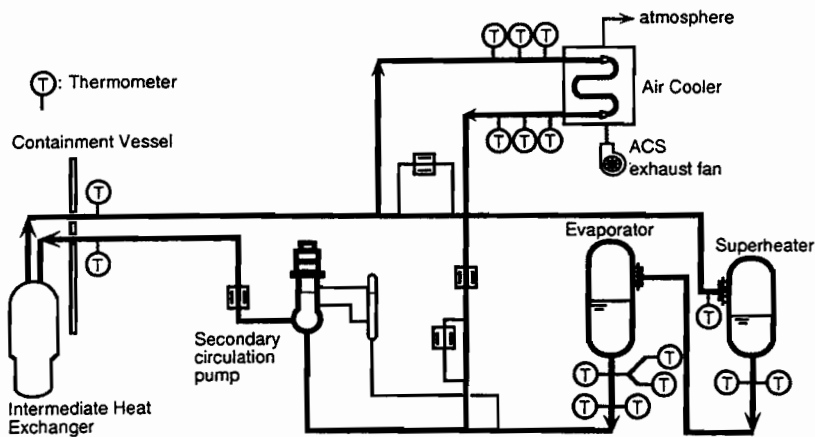


Fig. 2 Location and numbers of the existing thermometers on the secondary cooling system in Monju

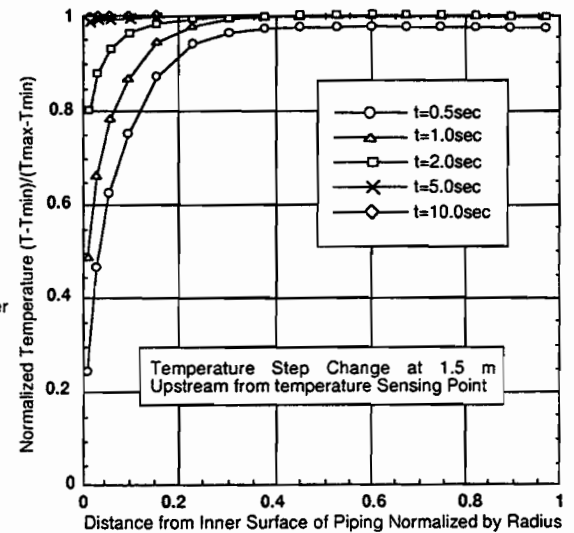


Fig. 3 Temperature Distribution Change in Transient Condition over the Section of a Piping

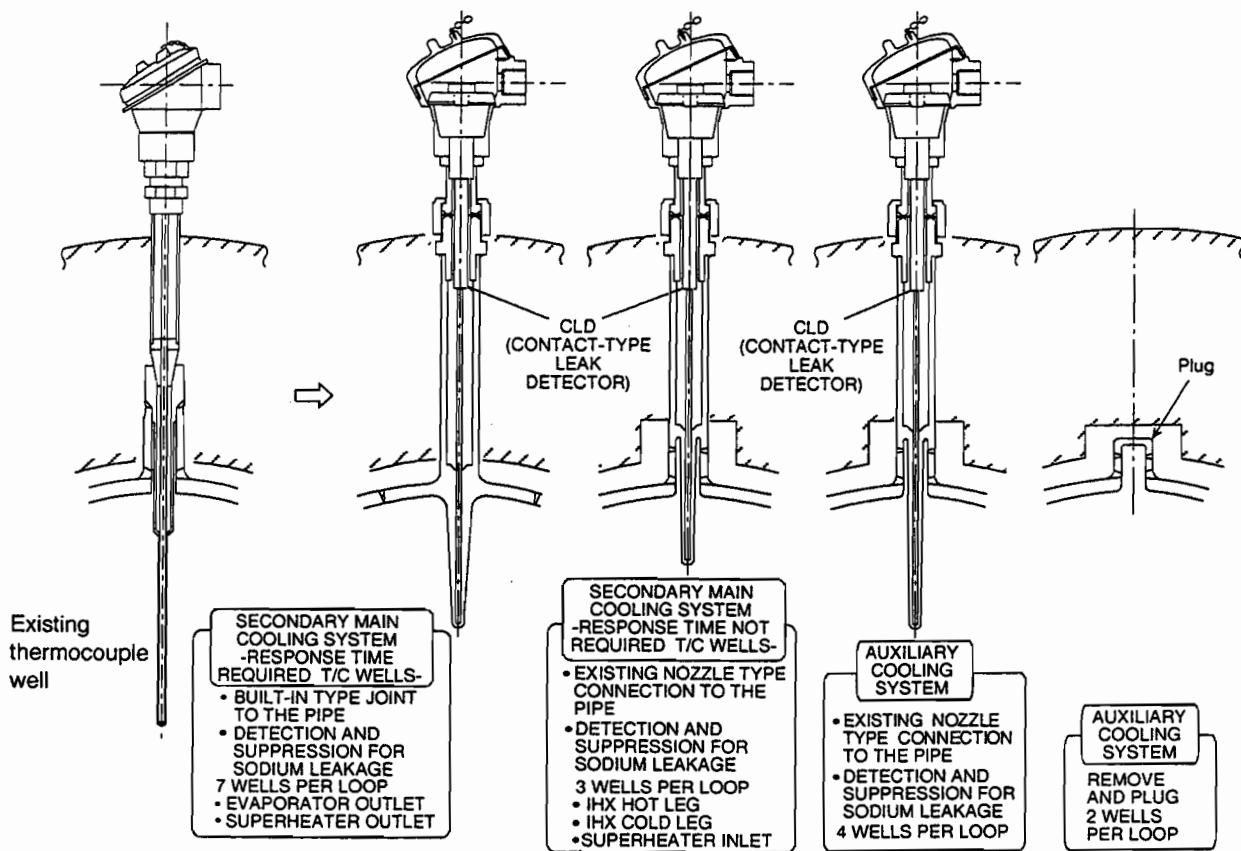


Fig. 4 Modified Design Concepts of the Thermocouple Wells on the Secondary Cooling System

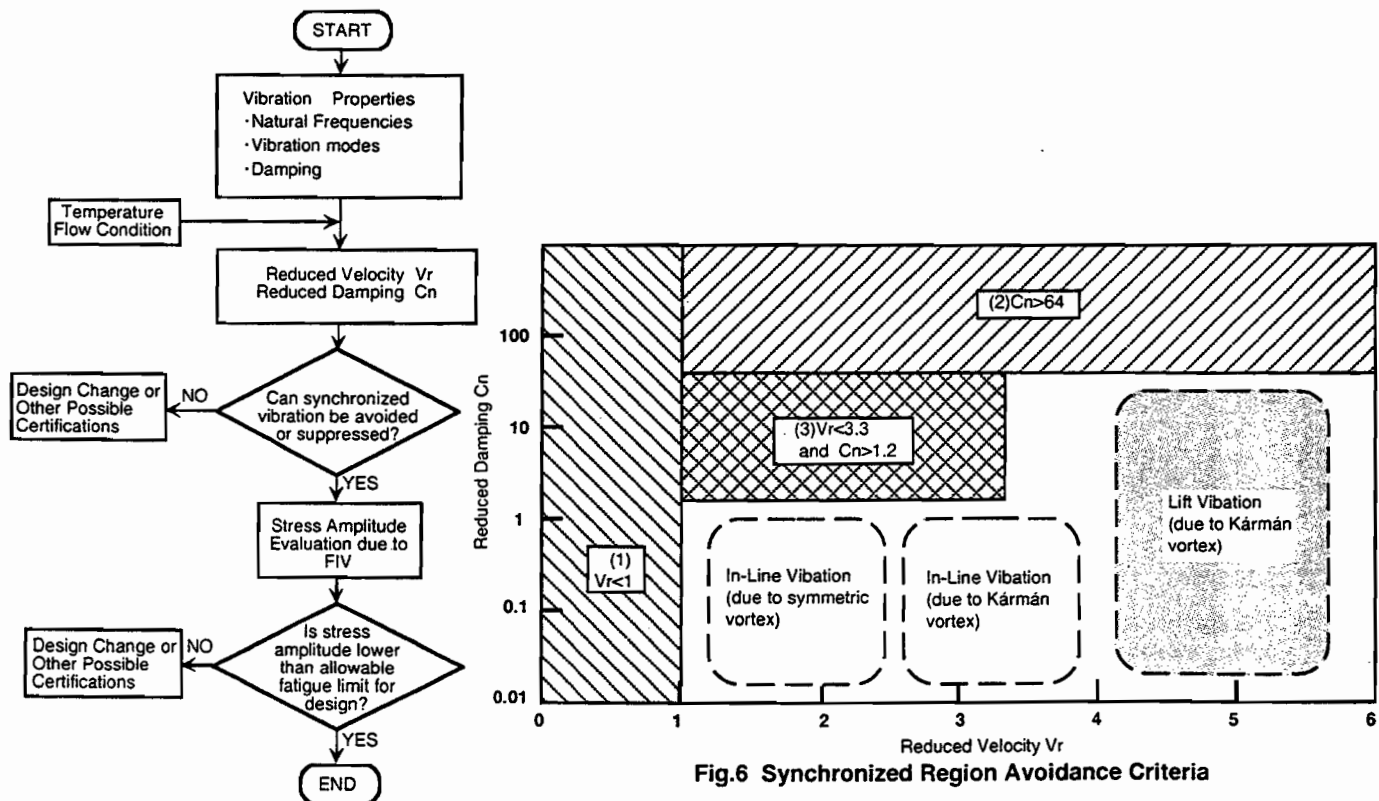


Fig. 6 Synchronized Region Avoidance Criteria

Fig. 5 Design Evaluation Procedure of Thermowells against FIV

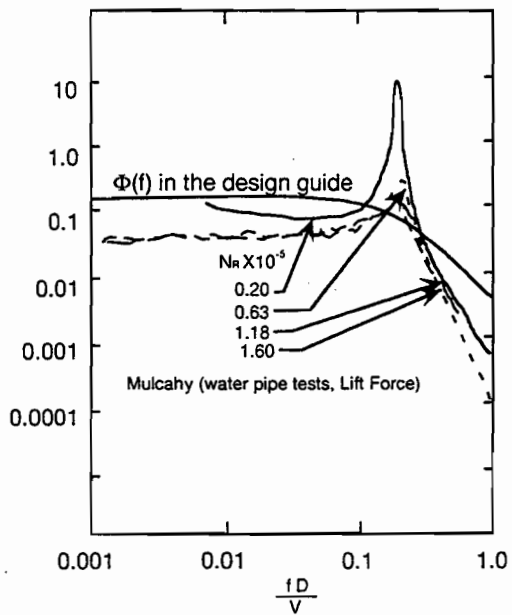


Fig.7 Comparison of Normalized Power Spectral Density in the design guidewith Experimental Data⁽⁶⁾

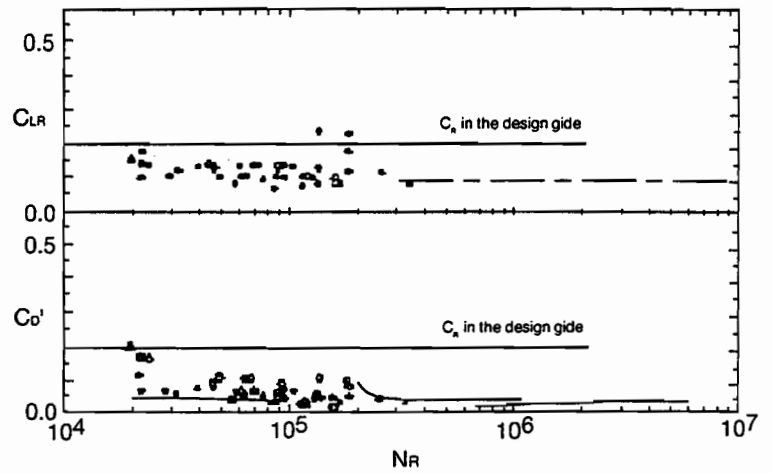


Fig.8 Comparison of Coefficient for Fluid Force by Turbulence, C_R with Experimental Data⁽⁶⁾



ASME International

The American Society of Mechanical Engineers
345 East 47th Street
New York, NY 10017

Reprinted From
**PVP-Vol. 363, Flow-Induced Vibration and Transient
Thermal-Hydraulics**
**Editors: M. K. Au-Yang, T. Nakamura, F. Hara,
A. Okajima, and Y. W. Shin**
Book No. H01144 - 1998

HISTORY OF FLOW-INDUCED VIBRATION INCIDENT OCCURRED IN MONJU

Masaki MORISHITA

O-arai Engineering Center,
Power Reactor and Nuclear Fuel Development Corporation
O-arai, Ibaraki, JAPAN

Koji DOZAKI

MONJU Construction Office,
Power Reactor and Nuclear Fuel Development Corporation
Tsuruga, Fukui, JAPAN

ABSTRACT

On 8 December 1995, Monju fast breeder reactor experienced a sodium leakage from one of its secondary heat transport systems (SHTS) main piping. However, the reactor core was remained cooled and the safety of the core was secured. Since the secondary sodium is not radioactive, there was no adverse influence on the surrounding environment and the operating personnel.

The leakage was caused by the failure of a thermocouple well that was inserted to the pipe. The tip of the thermowell was broken off due to high cycle fatigue caused by flow-induced vibration (FIV). It was found that this FIV was not induced by well known von Karman vortex shedding, but it was an in-line oscillation associated with symmetric vortex shedding.

An extensive investigation including FIV analyses and tests and fatigue and fracture mechanics analyses revealed the failure process of the thermowell due to FIV. Damping affected by the condition of the sheathed thermocouple inside the thermowell was attributed to the fact that only one thermowell failed among those in the SHTS with the identical dynamic characteristics.

The original design of the thermowells that could not prevent this failure was reviewed, and new designs for the improved thermowells were made.

INTRODUCTION

Monju is a Japanese prototype fast breeder reactor (FBR) of a loop-type with an electric power of 280 MWe (714 MW thermal). It is fueled with mixed oxides of plutonium and uranium and cooled by liquid metal sodium. The principal plant specifications of Monju are summarized in Table 1, and a schematic of the plant system is outlined in Fig. 1. (Suzuki, et al., 1996)

The Power Reactor and Nuclear Fuel Development Corporation

(PNC) is responsible for the FBR development project, including design, construction, and operation of Monju. The construction of the plant was commenced in October 1985 and completed in May 1991. Loading of the fuel into the core was started in October 1993. The initial criticality was achieved in April 1994 and the plant was first connected to the grid in August 1995. After that, electric power was gradually increased, on and off, as a series of power buildup test programs, with the rated power test planned for the scheduled time of June 1996.

It was in the course of this program that the sodium leakage incident occurred in a main sodium pipe of the SHTS on 8 December 1995. Although there was no radioactive influence on the environment, the incident brought about a serious social impact since it was the first sodium leakage in a nuclear facility in Japan.

A thorough investigation was made on the incident, and it was found by extensive analyses and tests that high cycle fatigue failure of a thermowell due to in-line flow-induced vibration was the direct cause of the sodium leakage. For the purpose of this investigation, a task force and a working group were established, independently by the Science and Technology Agency and the Nuclear Safety Commission.

In this paper, the major technical aspects of the incident and the following investigations are overviewed.

INCIDENT DEVELOPMENT

The sodium leakage incident occurred on 8 December 1995, when the plant was operated at its 40% of its full power as part of the plant performance tests. Depicted below is the time history of the incident development (Itoh, 1997).

1. Following a prior shutdown test, Monju was restarted on 6 December to conduct a plant trip test, as part of 40% electric power tests. Operation for increasing reactor power up to 45% was undertaken when the first alarm sounded.

Table 1

Principal plant specifications of Monju

Reactor type	Sodium-cooled, loop-type	Reactor Vessel	
Number of loops	3	Height / diameter	18 / 7 m
Thermal output	714 MWt	Primary coolant systems	
Electrical output	280 Mwe	Sodium inventory	760 ton
Fuel material	PuO ₂ -UO ₂	Inlet / outlet reactor temp.	397 / 529 °C
Core dimensions		Coolant flow velocity	6 m/s (inlet) 4 m/s (outlet)
Equivalent diameter	1790 mm	Secondary coolant systems	
Height	930 mm	Sodium inventory	760 ton
Plutonium enrichment (inner core / outer core)		Inlet / outlet IHX temp.	325 / 505 °C
(Pu fissile %)		Coolant flow velocity	5 m/s
Initial core	15 / 20	Water-steam systems	
Equilibrium core	16 / 21	Feed water flow rate	113.7 x 10 ⁴ kg/h
Fuel inventory		Steam temp. (turbine inlet)	483 °C
Core (U+Pu metal)	5.9 t	Steam press. (turbine inlet)	12.7 MPa
Blanket (U metal)	17.5 t	Type of steam generator	Helical coil
Average burn-up	80,000 MWD/T	Refueling system	Single rotating plug with fixed arm
Cladding material	SUS316	Refueling interval	6 months
Cladding outer diameter/thickness	6.5 / 0.47 mm		
Blanket thickness			
Upper/lower/radial	30 / 50 / 30 cm		
Breeding ratio	1.2		

* Fuel Handling Machine

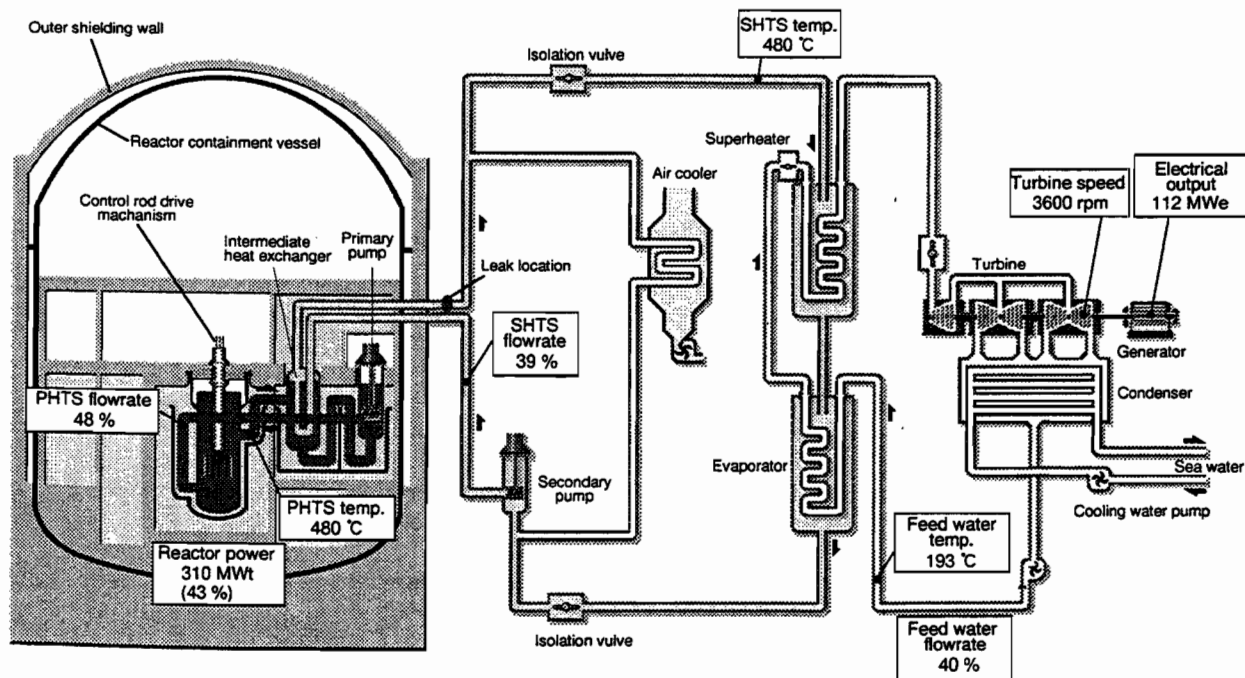


Fig. 1 Plant system of Monju

2. The plant conditions just before the sodium leakage were;

Reactor power	: 43%
Electric power	: 112MWe
Primary sodium temperature at reactor outlet	: 480°C
Primary sodium temperature at reactor inlet	: 360°C
Primary sodium flow rate	: 48%
Secondary sodium temperature at IHX outlet	: 480°C
Secondary sodium temperature at IHX inlet	: 285°C
Secondary sodium flow rate	: 39%
Main steam temperature	: 475°C
Main steam pressure	: 120 kg/cm ²
Feed water temperature	: 193°C
Feed water flow rate	: 40%
3. At 19:47 on 8 December, an alarm sounded indicating an unusually high sodium temperature at the outlet of the intermediate heat exchanger (IHX) in the SHTS C-loop. After six seconds, a fire alarm (smoke detector) also sounded, followed by another alarm indicating sodium leakage in the SHTS C-loop. It was recognized that a sodium leakage took place.
4. Reactor power-down operation was started at 20:00 according to the normal shut down procedure, judging that the scale of leakage was small. This judgement was based on the observation that there was no significant change in the sodium level both in the steam generator (SG) and the overflow tank.
5. Around 20:50, the number of activated fire alarms suddenly increased, and an increase in white fume was observed in the piping room. It was judged that the leakage had spread and the reactor was manually tripped at 21:20. After the trip, the auxiliary cooling system (ACS) cooled down the reactor. The SHTS was cooled down to about 400°C at 22:40.
6. Sodium draining was started in the C-loop at 22:40 in order to prevent further leakage, completing at 00:15, 9 December. The blowers of the air ventilation system in the C-loop automatically stopped.

7. The decay heat was removed from the core by remaining two loops (Monju has three sodium loops) operating at minimum flow rate. Thus, the reactor was safely shut down and the sodium leakage was ceased. There was no release of neither radioactive material nor sodium compound (aerosol) to the surrounding environment.

A walk down observation of the piping room was carried out right after the incident was settled down and it revealed that the location of the leakage was around a thermocouple installed on the main sodium pipe just downstream of the IHX of SHTS C-loop. Fig. 2 is a sketch of the piping room after the sodium leak. The sodium that leaked out reacted with air and resulted in sodium fire. Approximately 1 m³ of sodium compound formed a semicircular mound on the steel floor liner, nearly 3 m in diameter and 30 cm high. A ventilation duct directly beneath the pipe developed a hole extending over a half of the perimeter facing the concrete wall with lumps of deposits around the opening. On the walkway grating made of iron beneath the pipe, an opening was also formed and some lumps of the deposit stuck around the edges. No further anomaly was recognized in the main sodium pipe. Traces of sodium compound was observed over the entire floor of the SG room connected to the pipe room and on the passages of the first and second floors. It was estimated by later analysis that a total amount of about 640 kg of sodium leaked out.

INITIAL FAILURE INVESTIGATION

As shown in Fig. 3, the thermocouple well is horizontally inserted into the pipe, welded by a nozzle that stands on a sidewall of the pipe. The well extends into the center of the pipe, for about 185mm. It is not smoothly tapered, but there is a steep diameter change. The diameter of the well at the tip is 10 mm for about 150 mm long. A sheathed thermocouple is inserted into the well.

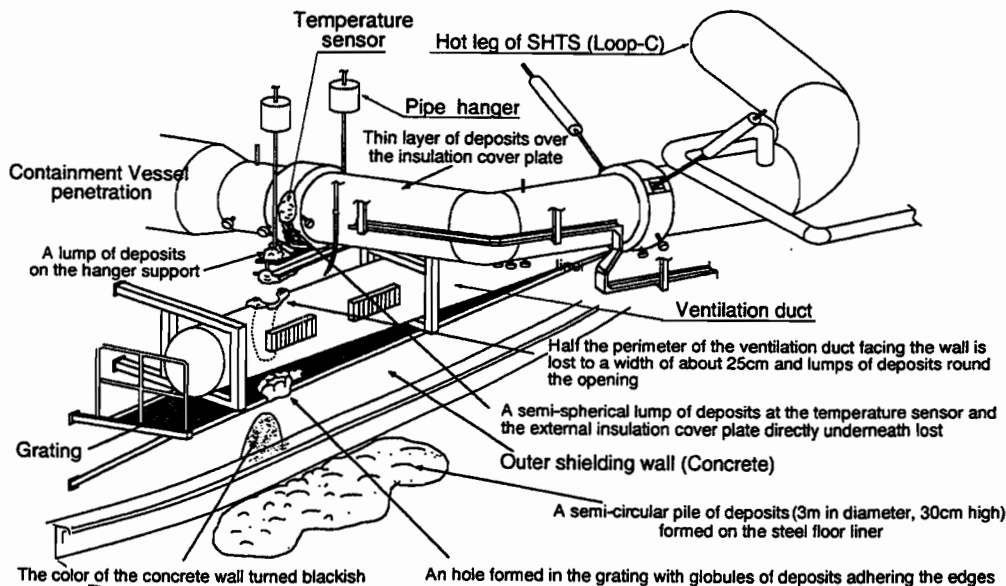


Fig. 2 Situation of the piping Room (C) after Sodium Leakage

Failure of the thermowell was suspected from the early stage since the leakage occurred around it. This was confirmed by radiography taken in-situ from outside the pipe. About two months later of the incident, the thermowell was cut out of the pipe and it was found that the tip of the well was broken apart at the root of the steep taper and missing, allowing sodium to leak directly out of the pipe. This tip was later found in the superheater and collected. The sheathed thermocouple remained intact, but it was bent about 45° toward downstream.

A close fractographic observation was made on the fracture surface of the thermowell by the National Research Institute of Metals and the Japan Atomic Energy Research Institute (Itoh, 1997). As illustrated in Fig. 4, the fracture surface showed a typical feature of high cycle fatigue failure with crack initiation, very slow propagation, and final ductile rupture.

Among the potential loads including thermal and mechanical ones, only FIV was identified to produce an alternating stress that could lead to high cycle fatigue failure by the preliminary analysis.

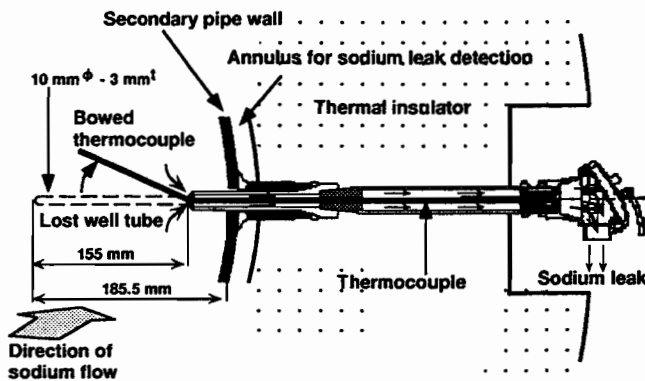


Fig. 3 Broken thermowell

[|||||] : Crack Initiation/coalescence - : Steps
 [] : Low propagation rate < : Direction of Growth
 [|||||] : Striation - - - : Estimated Crack Front
 [|||||] : Dimple

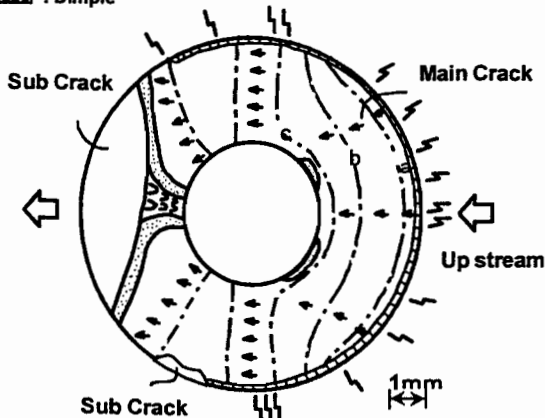


Fig. 4 Sketch of fractographic observation

DETAILED INVESTIGATION

In order to clarify in detail the cause of the thermowell fatigue failure due to FIV, a thorough investigation was made, including:

- Dynamic analysis of the thermowell
- FIV water loop tests on mock-up thermowells
- FIV analysis (CFD)
- Fatigue analysis
- Fracture mechanics analysis

From the studies, the cause and the process of the thermowell failure was clarified as follows:

1. The reduced velocity of the thermowell, $V_r = U/fD$, where U is sodium flow velocity, f and D are the natural frequency and the outer diameter of the well, was closed to 2 and the well was very lightly damped. Significant in-line oscillation with shedding of symmetric vortices, not with well-known Karman vortex street, took place under this condition. The occurrence of the in-line oscillation was confirmed both by the FIV water loop tests and CFD analysis (Yamaguchi, et al., 1997).
2. The failure process under the history of the plant operating conditions was estimated from the fracture mechanics fatigue crack analysis (Wada, et al., 1997).
 - a. Fatigue crack(s) was initiated at a relatively early period of 100% flow rate operation, due to the in-line FIV.
 - b. As the crack grew, the natural frequency of the well decreased, which in turn lowered the FIV response because the reduced velocity went out of the significant in-line oscillation range. The crack growth rate was correspondingly decreased, and finally the crack arrested during the 100% flow rate operation.
 - c. On the other hand, the condition of the reduced velocity V_r of 2 was achieved not in the steady 100% flow rate operations, but in transient periods from and to 100% flow rate. During these periods, the crack repeated gradual growth and arrest.
 - d. The crack grew farther and finally the in-line oscillation began to occur in the subsequent 40% flow rate operations, leading to the final failure and sodium leakage.
 - e. This scenario with a close interaction between in-line oscillation response and the crack growth through the change of natural frequency of the well was reproduced in the FIV water loop tests.

In total, forty-eight (48) thermowells were installed in the SHTS. Integrity of all the remaining thermowells in the SHTS was examined by radiography, ultrasonic inspection, and visual inspection with fibroscope. As a precaution, however, the thermowells in the other loops were reinforced by additional seals to prevent possible sodium leakage. Two thermowells were cut out of the pipe for detailed examination purposes. No slight structural damage or anomaly was found by these examinations.

Then a question was raised; why this particular thermowell failed while all the others remained intact? Additional vibration tests and FIV tests were carried out which focused on this issue, and it was found that the sheath of thermocouple inside the well significantly affected the damping characteristics and then FIV response of the well.

Basically the sheath increases the damping by dynamically interacting with the well; e.g., friction and shock between the sheath and the inner wall of the well. This effect is significant when the sheath is normal and straight. Since the in-line vibration is very sensitive to the damping, almost negligible response is produced when the sheath is normal. However, when the sheath is bent to the inside wall of the well, this interaction is suppressed and the damping is also decreased. With the bent sheath, significant in-line vibration occurs because of the low damping.

This dependency of damping and in-line response on the condition of the sheath inside the well was confirmed by vibration tests and FIV water loop tests, as are shown in Figs. 5 and 6. In addition, a good correspondence was seen between the patterns of scratch mark on the sheaths of failed thermocouple and artificially bent one.

From these observations, it was inferred that the damping of the failed thermowell was especially low due to the bent sheath and the thermowell suffered from a large in-line vibration.

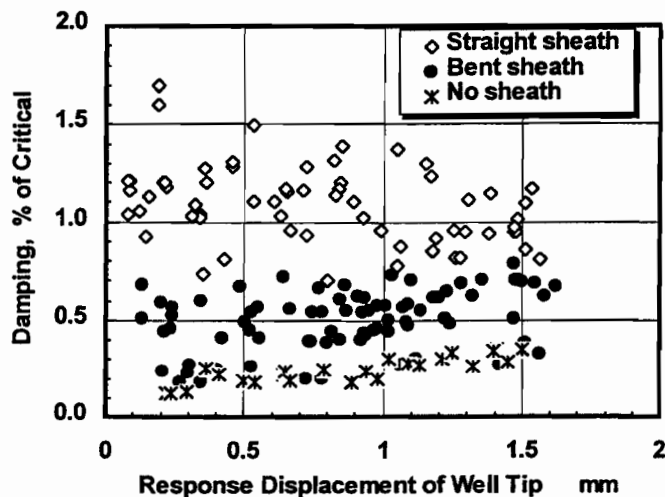


Fig. 5 Effect of sheath on damping of thermowell

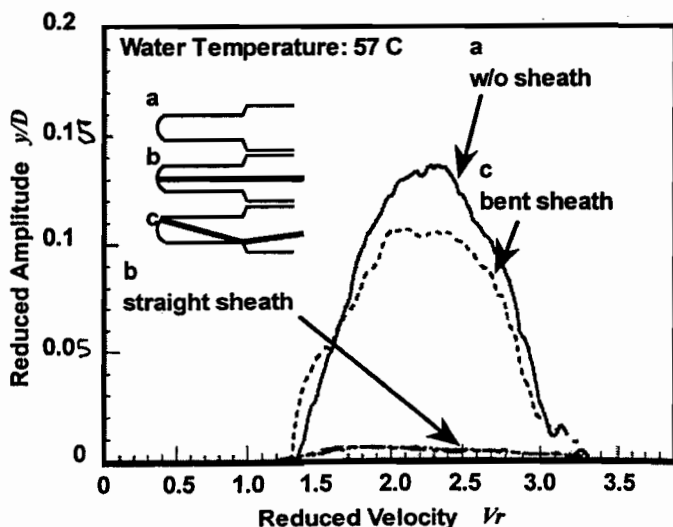


Fig. 6 Effect of sheath on in-line vibration response

REVISIT TO ORIGINAL THERMOWELL DESIGN

The original design of the thermowells was made during the period of 1984 through 1989. In this design, attention was only paid to avoid lock-in resonance with Karman vortex street in lift direction oscillation, as was usually done in designs against FIV. Here, reference was made to the ASME Performance Test Code 19.3, which was applicable to tapered thermowells. Importance was put on quick thermal response and measurement of the temperature at the center of the pipe. The geometry of the thermowell was rather governed by these factors, that is, small diameter and long well.

No consideration was given to the possibility of in-line oscillation with symmetric vortex shedding in the original design. Although this type of FIV had been known mainly in marine engineering pertinent to the offshore structures, neither PNC nor the manufacturer recognized its importance. On December 1991, a non-mandatory design guide on FIV of tubes and tube banks was supplemented to the Appendix N to the Section III of the ASME Boiler and Pressure Vessel Code. Design considerations for avoiding or suppressing both cross-flow (lift) and in-line (drag) oscillations by the vortex shedding were described in this guideline. However, both PNC and the manufacturer failed to take a chance to review the thermowell design on the issuance of the revised Appendix N.

Lack of recognition that thermowells are important components composing part of the main sodium boundaries can be pointed out as another shortcoming in the original design. Because the thermowells formed part of the sodium boundary, care should have been taken in their design as in the design of the Class III components. However, the thermowells were treated as instrumentation devices and no clear and explicit classification as sodium boundary components was given in their design specifications.

It also implies a poor structural design that there was no specification given on finishing the root of the diameter transition to give a sufficiently large radius of curvature. In fact, the root of the diameter transition was left as lathed. If a proper finishing had been specified to avoid an excessive stress concentration at the geometrical discontinuity, then this failure might have been avoided.

MODIFIED THERMOWELL DESIGNS

It was decided to replace all the thermowells in the SHTS with modified designs, since those in the main loops were susceptible for in-line FIV with their reduced velocity being around 2. Three thermowell designs were newly developed, depending on their functional requirements and locations. All the designs uses tapered well, instead of steep diameter change. A redundant suppression mechanism is also employed against postulated failure of the well and sodium leakage. Susceptibility of these designs was evaluated in accordance with the "Proposed Flow-induced Vibration Design Guide for Thermometer Wells" that was developed by PNC.

The three thermocouple designs, Type A, B, and C are shown in Fig. 7, along with the existing ones. The Type A thermowell is directly welded to the pipe, while the Type B and C thermowells are mounted on the existing nozzles. The three design types have different penetration designs and different insertion length into the flowing stream. However, outboard of the pipe the designs are

identical.

The Type A design provides the most rigid design to minimize FIV with a pipe wall penetration of 105 mm into the flowing stream. This design requires that the original thermowell nozzle be cut out and replaced with a solid section which supports the inner well probe and the outer nozzle extension. The Type A design has been selected for those locations where the thermal response measurement is part of the secondary main loop safety system.

The Type B design does not require removal of the original nozzle but the penetration into the flow stream is reduced to 55 mm to provide adequate rigidity to resist FIV. The thermowells of this design are used for control and recording functions in the main secondary loop.

The Type C thermowells are the same as the Type B except that the penetration into the pipe wall is 105 mm, the same as for Type A. This design is used in the secondary system auxiliary flow loop where the velocity is low and there is no concern about FIV.

CONCLUSIONS

The direct cause of the sodium leakage incident in the Monju fast breeder plant was identified to be high cycle fatigue failure of a thermocouple well that was caused by FIV. This FIV was not usual lock-in resonance with Karman vortex shedding, but in-line oscillation associated with symmetric vortex shedding.

An extensive investigation including FIV analyses and tests and fatigue and fracture mechanics analyses revealed the failure process of the thermowell due to FIV. Damping affected by the condition of the sheath inside the well was attributed to the fact that the only one well failed among those which had the identical dynamic characteristics in the SHTS wells.

The original design of the thermowells that could not prevent this failure was reviewed, and the new designs for the improved thermowells were presented.

REFERENCES

ASME Boiler and Pressure Vessel Code Section III, Division I, Appendix N, Article N-1300, ASME, 1995

ASME Power Test Code Supplement on Instruments and Apparatus -Part 3- Temperature Measurement, ASME, 1929

Hiroi, H. et al., 1996, "Analysis of the Monju's Sodium Leak Accident and Investigation of the Cause", PNC Technical Review, No. 99, pp23, (in Japanese)

Itoh, W. et al., 1997, "Technical Report on Monju's Sodium Leak Incident", Journal of Atomic Energy Soc. of Japan, Vol. 39, No. 9, pp.704, (in Japanese)

Proposed Flow-induced Vibration Design Guide for Thermometer Wells, PNC TN9410 97-042, PNC, 1997 (in Japanese)

Suzuki, T. et al., 1996, "Monju Secondary Heat Transport System Sodium Leak", Proceeding of 10th Pacific Basin Nuclear Conference, Kobe, Japan

Wada, Y. et al., 1997, "Failure Mechanism of a Thermocouple Well Caused by Flow-induced Vibration (2) Interaction between Flow-induced Vibration and Fatigue Crack Growth in a Thermocouple Well", Proceeding of the 4th Int. Symp. on Fluid-structure Interactions, Aeroelasticity, Flow-induced Vibration and Noise, ASME, AD-Vol. 53-1, pp149

Yamaguchi, A. et al., 1997, "Failure Mechanism of a Thermocouple Well Caused by Flow-induced Vibration (1) Numerical Simulation and Water Experiment of Flow-induced Vibration", Proceeding of the 4th Int. Symp. on Fluid-structure Interactions, Aeroelasticity, Flow-induced Vibration and Noise, ASME, AD-Vol. 53-1, pp139

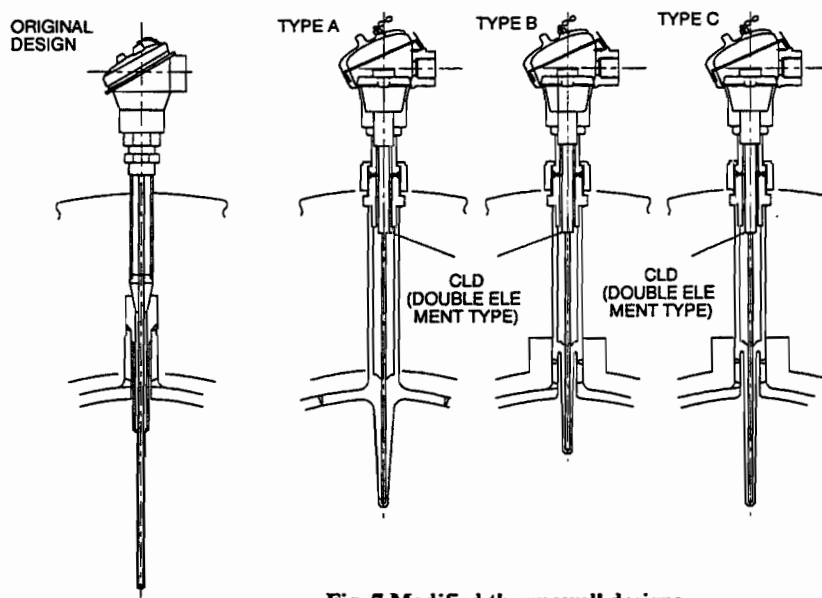


Fig. 7 Modified thermowell designs



ASME International

The American Society of Mechanical Engineers
345 East 47th Street
New York, NY 10017

Reprinted From
PVP-Vol. 363, Flow-Induced Vibration and Transient
Thermal-Hydraulics
Editors: M. K. Au-Yang, T. Nakamura, F. Hara,
A. Okajima, and Y. W. Shin
Book No. H01144 - 1998

CAUSE OF FLOW-INDUCED VIBRATION OF THERMOCOUPLE WELL

Kenji Ogura*

Masaki Morishita**

Akira Yamaguchi**

*: TOSHIBA Corporation, Isogo Nuclear Engineering Center
8, Shinsugita-cho, Isogo-ku, Yokohama 235-8523, JAPAN
Phone: +81-45-770-2413

Facsimile: +81-45-770-2266

**: O-arai Engineering Center
Power Reactor and Nuclear Fuel Development Corporation
4002 Narita, O-arai, Ibaraki 311-1393, JAPAN

ABSTRACT

In December 1995, a thermocouple well broke at the prototype fast breeder reactor, Monju. In this paper, a water flow test and numerical simulation of the flow-induced vibration of the thermocouple well are presented. The test was conducted in water using a full-scale model. Both the test and analysis identified an in-line vibration and symmetric vortex shedding at the rated flow condition. Furthermore, it was found that an in-line vibration occurred at a decreased flow rate, if the natural frequency of the thermocouple well was reduced.

1. INTRODUCTION

Liquid sodium leaked from the Monju fast breeder reactor in December 1995. It was caused by flow-induced vibration, which damaged a thermocouple well of the secondary main cooling piping (Yamaguchi, 1997).

The thermocouple on the secondary main cooling piping is welded to the side of piping with the well projected 185 mm in the piping. The diameter of the well is reduced to 10 mm over a length of 150 mm from the end as shown in Fig. 1. Generally, a well placed in a flow field vibrates due to the Karman vortex formed in the flow. A certain factor other than the lock-in in the cross flow direction by the Karman vortex is supposed to have existed because the frequency of Karman vortex at 100% flow is about 40% of the natural frequency of the well and the liquid sodium leakage occurred at a much smaller velocity of flow (during a 40% flow test). In this paper the authors explain the flow induced vibration of a thermocouple well based upon the results of hydrodynamic tests and numerical analysis conducted within the framework of efforts to identify causes of the damage to the thermocouple well.

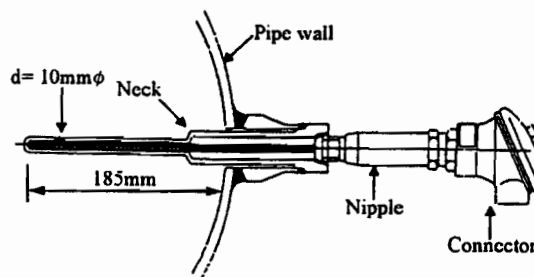


Fig. 1 Schematic drawing of the thermocouple well.

2. FLOW-INDUCED VIBRATION TEST

2.1 Basic method of test

(1) General

The authors conducted a hydrodynamic test with a full-scale model of the thermocouple well in order to establish the hydrodynamic characteristics of the thermocouple well under conditions of the same size piping as that of the Monju reactor. We have collected data on the basic characteristics of the flow induced vibration and evaluated the effect of the following parameters on the vibration characteristics:

- Natural frequency of thermocouple well
- Temperature condition of fluids
- Presence/absence of circulating flow in piping
- Insertion condition of thermocouple sheath.

The basic method of the test is described below.

a. Simulation of the piping and thermocouple well

A full-scale model was used in the test. The diameter (outer diameter: 558.8 mm) and wall thickness (9.5 mm) of piping was simulated. The thermocouple well, including nipple and connector, was simulated in full-scale.

b. Simulation of fluid flow field in piping

Simulation of local fluid flow characteristics (vortex shedding

characteristics) is significant for evaluation of the vibration characteristics of a thermocouple well. The velocity and Reynolds number of coolant under the reactor operating condition was simulated in the water flow test. The kinetic viscosity coefficient of liquid sodium was simulated by change of water temperature. It was estimated from a water flow test separately conducted that circulating flow was generated in the piping. For this reason, the test was conducted by adding circulating flow in order to evaluate its effect in the piping on the flow induced vibration characteristics of thermocouple well.

Simulation of vibration characteristics

Concerning the characteristics of vibration, we focused on the reduced flow velocity (Vr) and reduced damping (Cn), which are considered to be significant parameters for the evaluation of flow-induced vibration. They are defined as follows:

① Reduced flow velocity

$$Vr = (v/fd), \quad (1)$$

where, v: Average flow velocity over cross-sectional area of piping (m/s), d: Diameter of well tube (m), f: Well natural frequency (Hz).

② Reduced damping (stability parameter)

$$Cn = \frac{4\pi\xi_n \int_L m_t(x) \phi_n(x)^2 dx}{\rho d^2 \int_{L_e} \phi_n(x)^2 dx} \quad (2)$$

where, m_t : Total mass per unit length of well (kg/m)

ξ_n : Damping ratio(-)

ρ : Density of fluid (kg/m³).

ϕ_n : n -th vibration mode

L_e : Length of well in the fluid (m)

L : Length of well (m)

Vr can simulate the actual condition by making the shape of the thermocouple well model and flow velocity in the piping the same as the actual system. The condition Cn of the actual system can be mostly simulated in the above manner, although it becomes lower in the test than in the actual one since the density of water is higher than the sodium in the range of testing conditions used in the test. Cn (test)/Cn (actual system) is approximately equal to 0.92 for simulation of sodium at 200°C. However, the effect of Vr on the flow induced vibration characteristics of the thermocouple well was evaluated over a wider range in the test with the fluid velocity and natural frequency of thermocouple well taken as parameters.

(2) Testing apparatus and thermocouple well model

Figure 2 shows the apparatus used for the water flow test. A closed loop was employed as the loop configuration with the outer diameter and wall thickness of piping set to the same values as those of the actual system. A rectification lattice was installed at the upstream of the piping to rectify the flow at the section in which the thermocouple well was installed. A device to add the circulating flow was also installed in some cases.

Figure 3 illustrates the test pieces used for the thermocouple well. A reduced natural frequency well was used to establish the effect of the natural frequency of the thermocouple well together with an intact well to obtain a basic knowledge of the characteristics. This test assumed that the crack generated on the neck of the thermocouple well reduced the natural frequency of the well. More specifically, it is a thermocouple well model with natural frequency reduced to about 50% of the intact well by partially reducing the wall thickness of well tube to 1 mm. However, the outer diameter of the tube at the area with reduced thickness is maintained to 10 mm by refilling the area with resin to eliminate the influence interaction between the tube and fluid.

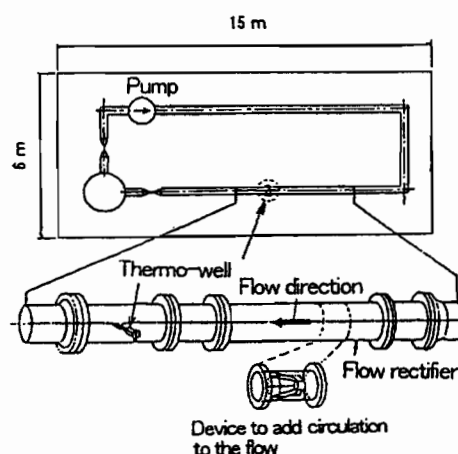


Fig. 2 High temperature water flow test loop

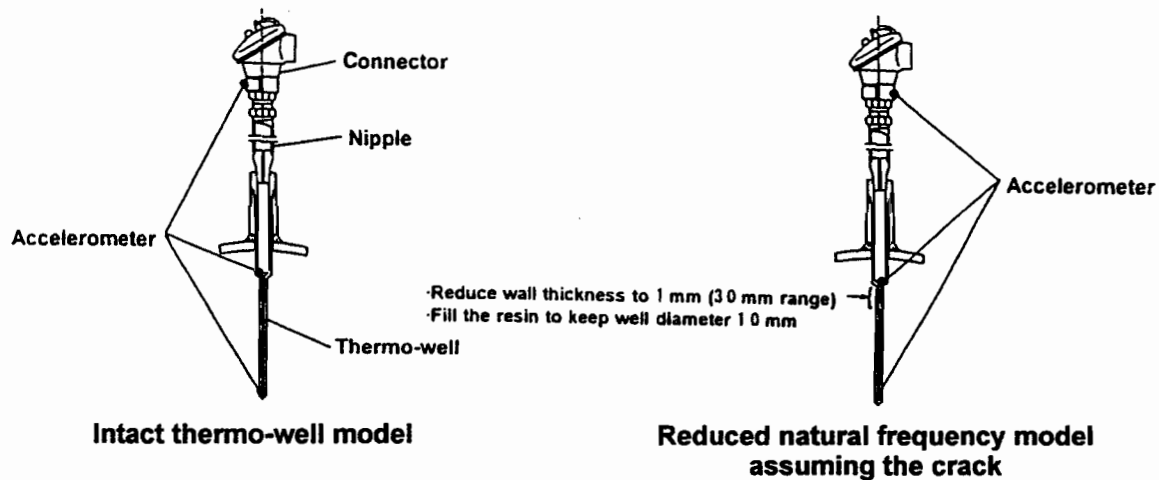


Fig. 3 Concept of thermo-well model

(3) Parameters and conditions for test

a. Basic case

- Thermocouple well model: Intact well (without thermocouple sheath)
- Water temperature: 57°C (equivalent kinetic viscosity of 200°C sodium)
- Circulating flow in pipe: None

b. Test parameters

Items listed below were used as parameters for the test of the basic case in order to evaluate the effect on the characteristics of flow induced vibration.

① Natural frequency of thermocouple well

Reduced natural frequency well (natural frequency approximately 110 Hz) was used. (See Fig. 3)

② Water temperature

The relationship between the water temperature setting the testing condition and the temperature of sodium simulated at the temperature is shown below.

- Water temperature 57°C: Equivalent kinetic viscosity of 200°C of sodium (Basic case)
- Water temperature 78°C: Equivalent kinetic viscosity of 325°C of sodium
- Water temperature 98°C: Equivalent kinetic viscosity of 450°C of sodium

Table 1 compares the kinetic viscosity and density of each fluid in the basic case.

③ Circulating flow in pipe

The device to add circulating flow in the piping was installed at the upstream of the section where the thermocouple well is installed to simulate the flow condition in the pipe as anticipated at the section (about 20% of the velocity of main flow). (See Fig. 2)

Table 1 Comparison of fluid properties (water and sodium)

	Water	Sodium
Temperature(°C)	57	200
Fluid mass density (kg/m ³)	985	904
Kinetic viscosity (m ² /s)	5×10^{-7}	5×10^{-7}

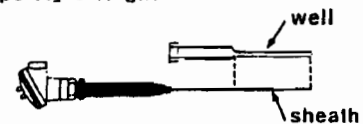
(Example at sodium temperature 200°C)

④ Insertion condition of thermocouple sheath

The insertion condition of the thermocouple sheath was used as the parameter as follows (see Fig. 4):

- Thermocouple sheath installed (straight sheath)
- Thermocouple sheath installed (with sheath knuckled at step-like joint of thin and thick tubes of well)

[Type A] Straight



[Type B] Knuckled

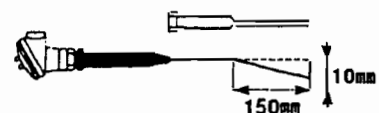


Fig. 4 T/C sheath condition in the thermo-well

The flow velocity in the pipe swept the range between about 1m/s to 8m/s, which included the actual rated flow velocity condition of 5.5m/s.

2.2 Test results

(1) Basic characteristics of flow induced vibration of thermocouple well (basic case)

a. Natural frequency

Figure 5 shows the results of measurement of thermocouple well model vibration frequency under the condition of flow velocity in the pipe swept up to 8.3 m/s and water temperature 57°C (equivalent kinetic viscosity of 200°C sodium) given by the analysis of response from an accelerometer installed at the neck of the well. The result shows that the frequency of about 250 Hz dominates in both the in-line and cross flow directions without any observable amount of other components. Fig. 6 shows the results of analysis of the response at the end of the thermocouple well with the white noise applied as the external condition in the form of a transfer function. The result shows that the vibration mode of the thermocouple well as a cantilever (secondary mode) dominated as compared with the rocking mode of the well (primary mode). The result shown in Fig. 5 corresponds to the secondary mode as judged from vibration frequency.

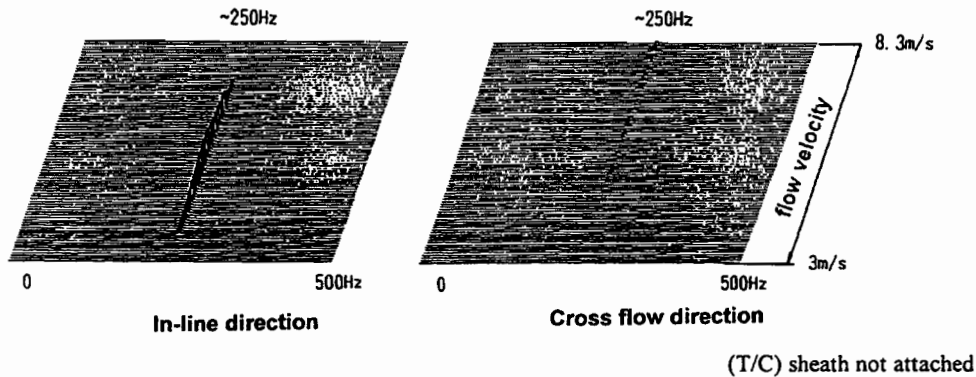


Fig. 5 Natural frequency in the velocity sweep test

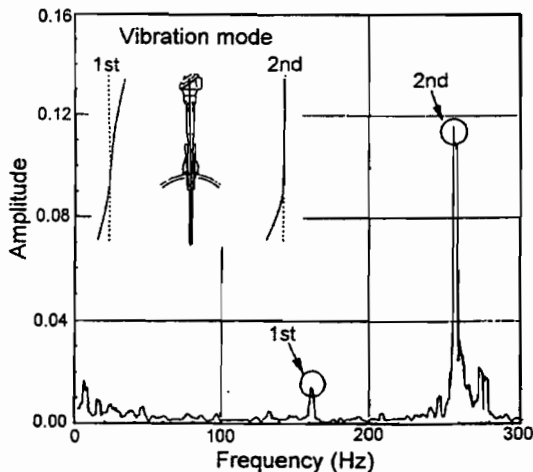


Fig. 6 Transfer function of thermo-well displacement (Analysis)

b. Acceleration response

Figure 7 shows the response of the accelerometer. The vibration in the in-line direction started from the region of low flow velocity (about 3.5 m/s) as compared with the rated flow velocity (5.5 m/s). The vibration increased with increasing flow velocity and reached the maximum value at the velocity of about 5 to 6 m/s. The vibration tended to decrease at flow velocities higher than this value. The degree of vibration in the cross flow direction is low compared with that in the in-line direction. The vibration in this mode occurs in the lower flow velocity region than the usually anticipated Karman vortex synchronized vibration region. This is because the resonance flow velocity with the Karman vortex is calculated to be equal to about 12 m/s assuming a Strouhal number of 0.21. The vibration was found to have a nearly completely sinusoidal waveform as shown in the enlarged chart of acceleration waveform attached to Fig. 7.

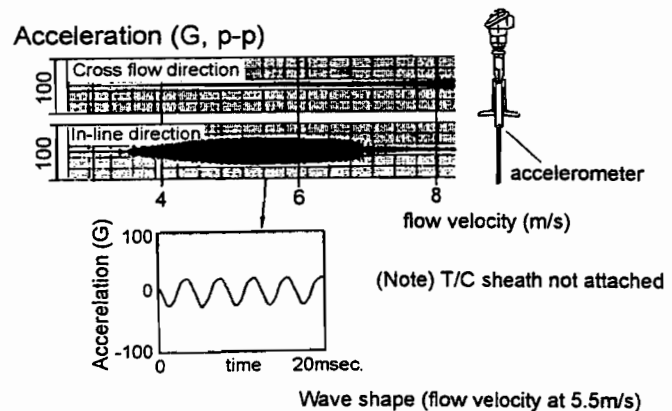


Fig. 7 Response of the accelerometer

c. Displacement at the end of the thermocouple well

Figure 8 shows the displacement at the end of the thermocouple well (non-dimensional amplitude) estimated from the response of the accelerometer together with reduced flow velocity (V_r). The vibration in the in-line direction started at the reduced flow velocity of about 1.3. The displacement reached the maximum value at 2.2, followed by a gradual decline. The maximum displacement was about 1.3 mm. The displacement in the cross flow direction is relatively small.

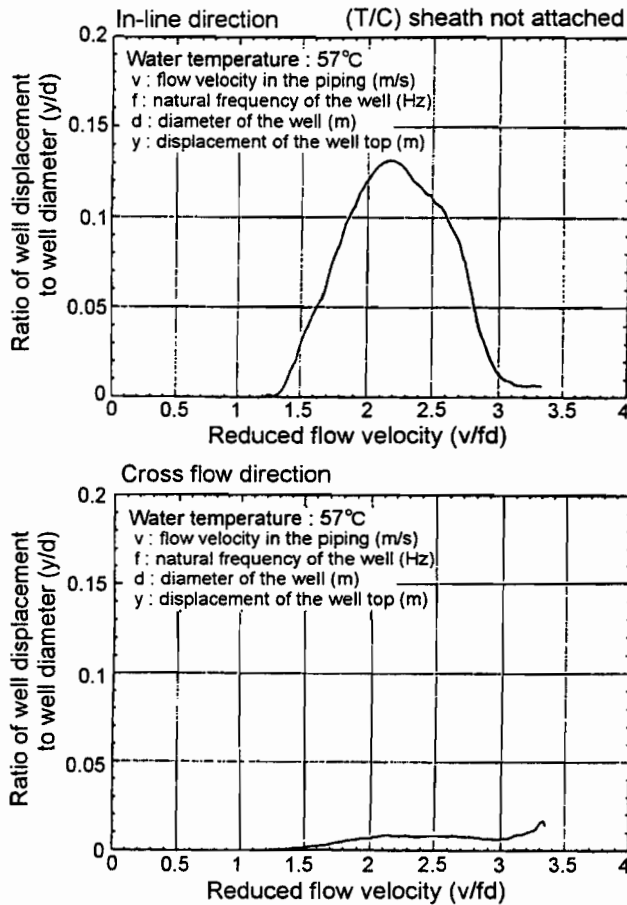


Fig. 8 Ratio of well displacement to well diameter in the in-line motion

d. Visualization of vibration behavior

The flow at the end of the thermocouple well was visualized by bubbles injected at the upstream and illuminated with a laser light sheet. The result is shown in Photo. 1, demonstrating the symmetric formation of vortices on both sides of the well under the presence of vibration in the in-line direction at a rate of one pair of vortices per cycle in synchronization with the vibration.

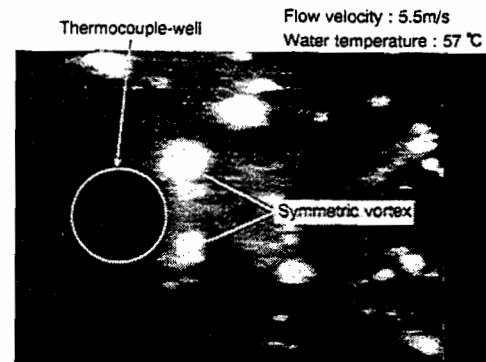


Photo. 1 Visualized symmetric vortex around the thermo-well

(2) Evaluation of effect of several factors on the flow-induced vibration characteristics

a. Natural frequency of thermocouple well

We conducted a test under the condition of reduced natural frequency of the thermocouple well. Fig. 9 compares the displacement in the in-line direction at the end of the well arranged with the reduced flow velocity with the basic case.

Vibration in the in-line direction starts at the reduced flow velocity of about 1.3 and shows a similar behavior to the basic case. When it is converted to actual flow velocity, the vibration starts at a flow velocity of about 1.5 m/s, or lower velocity than the velocity in the basic case (about 3.5 m/s). As the gradual decline of displacement was observed in a similar manner at reduced velocity of 3 or higher, it was judged that data on thermocouple well model with different natural frequency can be rearranged by the reduced flow velocity. The smaller vibration displacement of reduced natural frequency well than that of the basic case may be attributed to the increased damping due to filling of the thin walled section with resin.

A reduced flow velocity of 2 is obtained under the assumption of 40% flow rate condition of the actual system (flow velocity: 2.2 m/s) and the vibration may start in the region. For this reason, the vibration may start under the 40% flow rate condition in the thermocouple well with reduced natural frequency due to crack propagation.

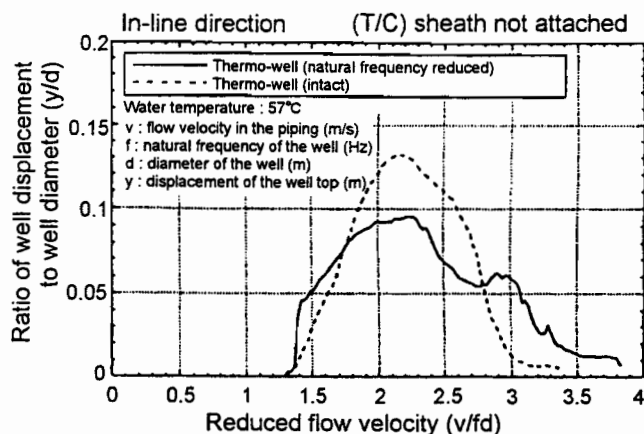


Fig. 9 Ratio of well displacement to well diameter in the in-line motion (effect of natural frequency of thermocouple well)

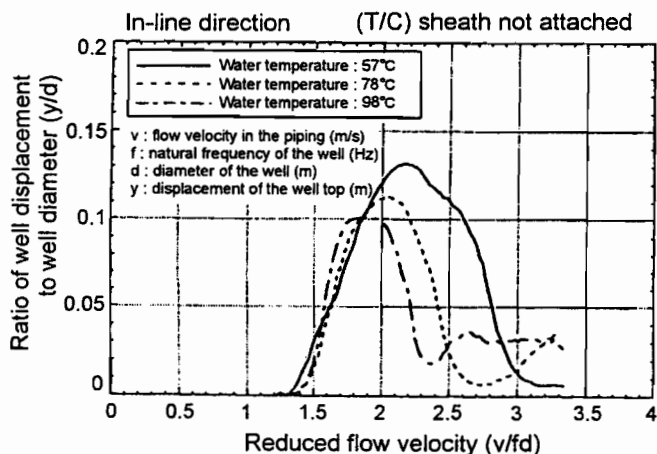


Fig. 10 Ratio of well displacement to well diameter in the in-line motion (effect of water temperature (intact well))

b. Temperature condition of fluid

Figure 10 shows the displacement at the end of the thermocouple well in the intact well with the water temperature taken as the parameter. Although the vibration onset flow velocities match each other, the displacement of vibration was temperature dependent, showing a gradual reduction of the maximum displacement at the end of the well with increasing temperature.

Figure 11 plots the similar result of the reduced natural frequency well, which did not show temperature dependency as seen in the basic case. The flow velocity may be involved together with the water temperature since the flow velocity of the reduced natural frequency well for the same reduced flow velocity was about 50% of that in the basic case. Accordingly, this behavior may be also affected by the Reynolds number.

Values of Reynolds number (water temperature 98°C) for the reduced flow velocity of 2 were about 1.7×10^5 (intact well) and about 7×10^4 (reduced natural frequency well). The reduction of vibration displacement may be explained by the reduced correlation length due to the increased value of Reynolds number. Further investigation is needed.

c. Circulating flow in pipe

Figure 12 shows the displacement at the end of the well with the presence and absence of circulating flow as a parameter. It was confirmed from this result that the effect of circulating flow in the pipe on the basic flow-induced vibration behavior of the thermocouple well was low, including onset and termination conditions and displacement of the vibration.

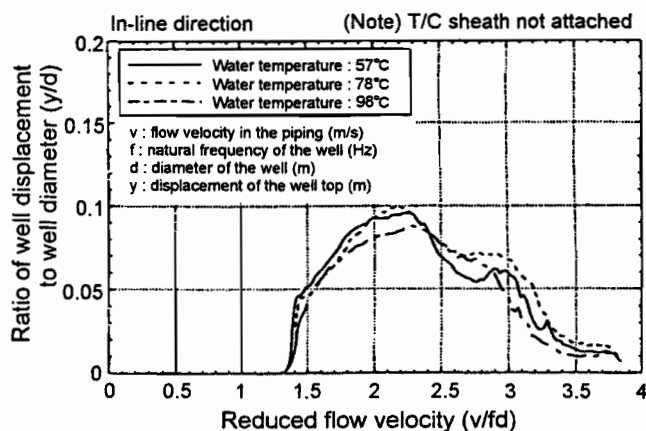


Fig. 11 Ratio of well displacement to well diameter in the in-line motion (effect of water temperature (natural frequency reduced well))

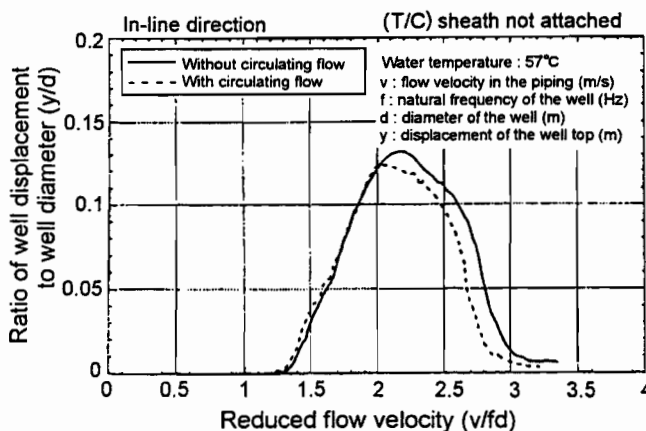


Fig. 12 Ratio of well displacement to well diameter in the in-line motion (effect of circulating flow in the piping)

d. Inserted condition of thermocouple sheath

Figure 13 shows the displacement at the end of the well with the insertion condition of the thermocouple sheath as a parameter.

The displacement under the presence of the thermocouple sheath was low as compared with that without the thermocouple sheath inserted. Without the knuckle of the sheath, in particular, the displacement was smaller than 10%. A reason for this was estimated to be the dissipation of energy caused by the interference effect between the thermocouple sheath and inner wall of the thermocouple well (collision and friction).

The displacement was larger in the case with the knuckled sheath since the well and the sheath vibrate in an integrated manner.

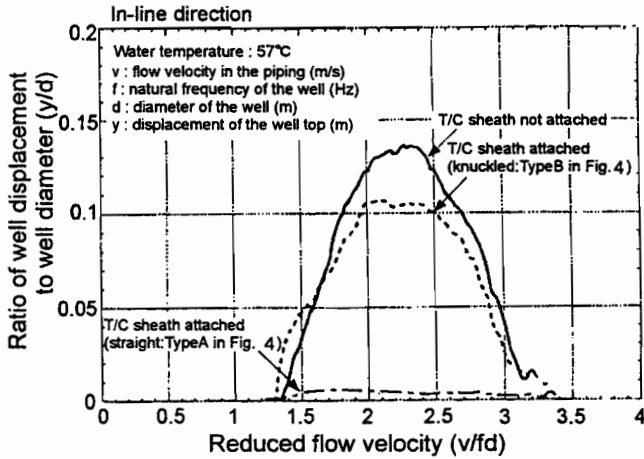


Fig. 13 Effect of sheath condition in the well

3. NUMERICAL SIMULATION

3.1 Fluid structure coupled model

The computer program solves Navier-Stokes equations coupled with equation of structural motion by ALE method (Arbitrary Lagrangian and Eulerian). A geometry for an analysis is limited to a two-dimensional model due to computational time and cost. Therefore three dimensional phenomena are transformed to a two-dimensional problem. This program has been verified by some theoretical solution and experimental results (Yamaguchi, 1996). The program is valid if a single cantilever mode dominates the motion of the thermocouple well. The well is modeled as a two-degree-of-freedom system with viscous damping. That is, the well is modeled as a nodal mass with spring and dashpot in the in-line and cross flow directions. Using the generalized mass and generalized force for the n -th mode, the equations of motion are expressed as the following equation (Blevins, 1977):

$$\begin{Bmatrix} \ddot{x} \\ \ddot{y} \end{Bmatrix} + \begin{bmatrix} 2\xi_n\omega_n & 0 \\ 0 & 2\xi_n\omega_n \end{bmatrix} \begin{Bmatrix} \dot{x} \\ \dot{y} \end{Bmatrix} + \begin{bmatrix} \omega_n^2 & 0 \\ 0 & \omega_n^2 \end{bmatrix} \begin{Bmatrix} x \\ y \end{Bmatrix} = \frac{1}{M_n} \int_0^L \begin{Bmatrix} P_x(z,t) \\ P_y(z,t) \end{Bmatrix} \phi_n(z) dz \quad (3)$$

where M_n is the generalized mass per unit length:

$$M_n = \int_0^L m(z) \phi_n^2(z) dz \quad (4)$$

This formulation equates the kinetic energy of the nodal mass and three-dimensional/beam. Here, x and y are the displacements in the in-line and cross flow directions, respectively. Single and double dots describe the first and second derivatives with respect to time. Here, ϕ_n , ω_n and ξ_n are the mode shape function, the natural angular frequency, and the damping ratio with respect to the mode. The longitudinal coordinate is z in the slender part of the well, being 0 at the well tip. P_x and P_y are hydraulic force per unit length in the in-line and cross flow directions, respectively. They are calculated at the tip ($z = 0$) of the well as:

$$\begin{Bmatrix} P_x(0,t) \\ P_y(0,t) \end{Bmatrix} = \int_0^{2\pi} \begin{bmatrix} -p(\theta,t) & -\tau_\theta(\theta,t) \\ \tau_\theta(\theta,t) & -p(\theta,t) \end{bmatrix} \begin{Bmatrix} \cos\theta \\ \sin\theta \end{Bmatrix} \frac{d}{2} d\theta \quad (5)$$

where τ_θ is the circumferential shear stress at the surface and d is the outer diameter of the well. The pressure distribution on the well surface is obtained by solving the Navier-Stokes equations. The circumferential distribution of the shear stress is calculated from the radial gradient of tangential flow velocity around the well surface.

We need to determine the dependency of the in-line and cross flow loads on the longitudinal coordinate, z . From the preliminary analysis, it was found that the loads are almost in proportion to the displacement of the thermocouple well. Therefore, it is assumed that the longitudinal distribution of the load is evaluated using the mode function.

The mesh size in the radial direction around the thermocouple well is set to about $30 \mu\text{m}$ considering the thickness of the boundary layer (about $100 \mu\text{m}$). The area around the thermocouple well is divided in the circumferential direction into meshes of the same order (about $60 \mu\text{m}$). The increment of time is set to about $1 \mu\text{s}$ for reasons of analytical accuracy and numerical stability.

3.2 Analytical result

(1) Analysis for 100% flow rate condition

The result of flow-induced vibration analysis under the conditions of 100% flow rate, sodium temperature at 200°C , damping ratio equal to 1.0% and the natural frequency of 272Hz (in air) is examined as an example. The flow velocity was increased to a specified value ramp-wise in 0.1 s from the still state.

Figure 14 shows the time history of the displacement in the in-line and cross flow directions of the well. The root mean square (RMS) of displacement around the time average given by the

analytical result after 0.4 s is 0.59 mm and 0.13 mm, respectively, in the in-line and cross flow directions. As the response of displacement is nearly sinusoidal, the average displacement given by multiplying RMS by $\sqrt{2}$ is 0.83 mm and 0.18 mm in the in-line and cross flow directions, respectively.

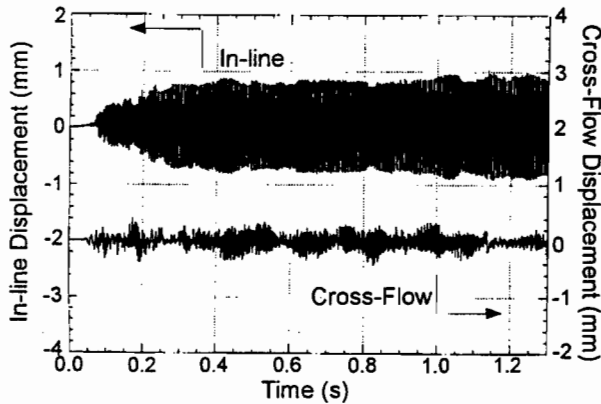


Fig. 14 Time history of the displacement response of the well

(2) Analysis for 40% flow rate condition

An analysis was performed to check whether the vibration occurs in the in-line direction under the conditions of 40% flow rate and sodium temperature 485°C of the intact thermocouple well (reduced flow velocity 0.9). The damping ratio of 0.5% was taken. The natural frequency in the sodium is about 240 Hz at this temperature. Figure 15 shows displacement in the in-line and cross flow directions. The average displacement determined from the range in which the response is almost steady was sufficiently smaller than 1% of the diameter of the thermocouple well in both the in-line and cross flow directions (order of 10^{-2} mm), suggesting that they would not damage the thermocouple well. Unlike the analytical result of 100% flow rate condition, the vibration in the in-line direction was not dominant.

Another analysis was conducted with reduced natural frequency and 40% flow rate condition under the assumption of a crack on the thermocouple well. Figure 16 shows the displacement in the in-line and cross flow directions under the condition of natural frequency reduced to 145Hz (in air). The reduced flow velocity was about 1.6. The synchronized vibration was analyzed in the in-line direction. It was shown that the flow-induced vibration may occur even with low flow velocity if the natural frequency of thermocouple well was reduced by the crack in the 40% flow rate condition.

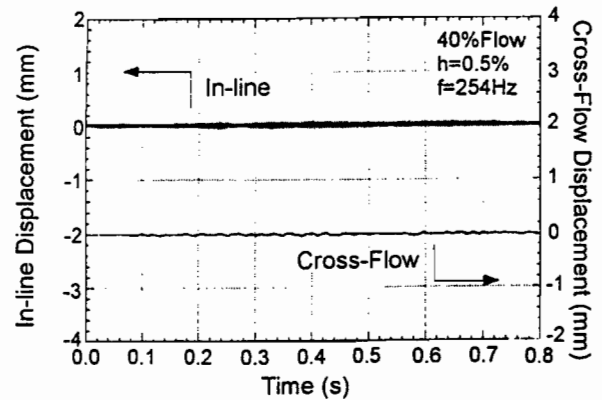


Fig. 15 Time history of the displacement response of the well at 40% flow

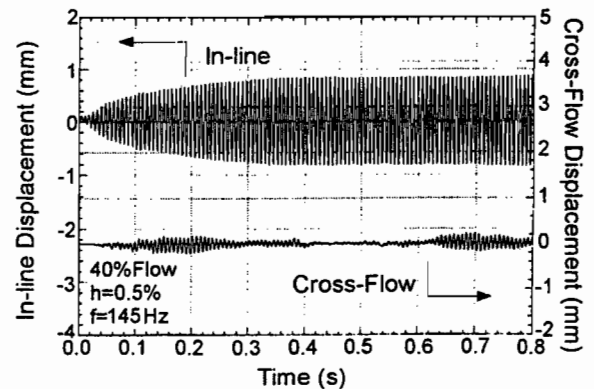


Fig. 16 Time history of the displacement response of the well with reduced natural frequency at 40% flow

4. CONCLUSIONS

- (1) As a result of the flow-induced vibration test and analysis of thermocouple well, dominant synchronized vibration was measured and analyzed in the in-line direction. The dominant vibration in the in-line direction has been observed in experiments conducted by several researchers including King (King, 1977). Symmetric vortex shedding from both sides of the thermocouple well was also confirmed. As discussed in chapter 2.1, size and reduced damping of the well model is almost same as the actual one. Therefore, according to these results, it is probable that the in-line synchronized vibration, which takes place when the reduced flow velocity is about 2, occurred in the damaged thermocouple well.
- (2) The authors investigated the flow-induced vibration characteristics under the condition of reduced natural frequency of the well, assuming a crack on the thermocouple well in the operating condition when the sodium leakage took place (40% flow rate and sodium temperature 485°C). Both the water flow test and analysis indicate that significant vibration did not take